Structural and Optical Properties of

III-V Semiconductor Materials

for Photovoltaics and Power Electronic Applications

by

Po-Yi Su

A Dissertation Presented in Partial Fulfillment
of the Requirements for the Degree
Doctor of Philosophy

Approved June 2020 by the
Graduate Supervisory Committee:

Fernando A. Ponce, Chair
Peter A. Crozier
David J. Smith
Yuji Zhao

ARIZONA STATE UNIVERSITY

August 2020

ABSTRACT

This dissertation focuses on the structural and optical properties of III-V semiconductor materials. Transmission electron microscopy and atomic force microscopy are used to study at the nanometer scale, the structural properties of defects, interfaces, and surfaces. A correlation with optical properties has been performed using cathodoluminescence.

The dissertation consists of four parts. The first part focuses on InAs quantum dots (QDs) embedded in a GaInP matrix for applications into intermediate band solar cells. The CuPt ordering of the group-III elements in $Ga_{0.5}In_{0.5}P$ has been found to vary during growth of InAs QDs capped with GaAs. The degree of ordering depends on the deposition time of the QDs and on the thickness of the capping layer. The results indicate that disordered GaInP occurs in the presence of excess indium at the growth front.

The second part focuses on the effects of low-angle off-axis GaN substrate orientation and growth rates on the surface morphology of Mg-doped GaN epilayers. Mg doping produces periodic steps and a tendency to cover pinholes associated with threading dislocations. With increasing miscut angle, the steps are observed to increase in height from single to double basal planes, with the coexistence of surfaces with different inclinations. The structural properties are correlated with the electronic properties of GaN epilayers, indicating step bunching reduces the *p*-type doping efficiency. It is also found that the slower growth rates can enhance step-flow growth and suppress step bunching.

The third part focuses on the effects of inductively-coupled plasma etching on GaN epilayers. The results show that ion energy rather than ion density plays the key role in the etching process, in terms of structural and optical properties of the GaN films.

Cathodoluminescence depth-profiling indicates that the band-edge emission of etched GaN is significantly quenched.

The fourth part focuses on growth of Mg-doped GaN on trench patterns. Anisotropic growth and nonuniform acceptor incorporation in *p*-GaN films have been observed. The results indicate that growth along the sidewall has a faster growth rate and therefore a lower acceptor incorporation efficiency, compared to the region grown on the basal plane.

To Wen-Hsiu, Mei-Jung, Po-Chung, and Chiu-Jung

ACKNOWLEDGMENTS

I would like to express my sincere gratitude to Professor Fernando A. Ponce, who guided me throughout my Ph.D. study and research at Arizona State University. Without his incredible support and encouragement, the goal of the projects would not have been realized. I benefited greatly from many wonderful discussions, and I will not forget the valuable help and motivation from him. Besides my supervisor, I wish to show my gratitude to my committee members, Dr. David J. Smith, Dr. Peter A. Crozier, and Dr. Yuji Zhao.

I would like to thank the former and current group members: Dr. Alec Fischer, Dr. Hongen Xie, Dr. Shuo Wang, Hanxiao Liu, and Dr. Shanthan Alugubelli, whom I have had spent a wonderful time working with. I wish to acknowledge the help provided by the technical and support staff in the Eyring Materials Center. Especially, I would like to thank Mr. Karl Weiss, Dr. Shery Chang, Dr. Manuel Gutierrez, Mr. Sisouk Prasavath, and Ms. Diana Convey for the technical support in TEM and AFM. I would like to thank Dr. Patricia L. Souza, Dr. Mauricio Pires, Dr. Roberto Jakomin, Eleonora Weiner, and Beatriz Rocha from the Pontifical University of Rio de Janeiro. I would also like to thank Dr. Houqiang Fu, Dr. Kai Fu, Dr. Xuanqi Huang, and Chen Yang in Dr. Yuji Zhao's research group at ASU. They care contributed greatly to the research that let to this dissertation.

Nobody has been more important to me in the pursuit of the Ph.D. than the members of own my family. I would like to acknowledge the support and great love of my father, Wen-Hsiu; my mother, Mei-Jung; my brother, Po-Chung; and my aunt, Chiu-Jung. They kept me going on and this work would not have been possible without their love and care.

TABLE OF CONTENTS

Page

CHAPTER Page

CHAPTER Page

LIST OF TABLES

LIST OF FIGURES

Figure Page

Figure Page

CHAPTER 1

INTRODUCTION TO III-V COMPOUND SEMICONDUCTORS

1.1 General Properties of III-V Compound Semiconductors

The III-V compound semiconductors obtained by combining group-III (Al, Ga, In, etc.) with group-V elements (N, P, As, etc.) offer advantages in materials properties over silicon, such as higher carrier mobility, and wider direct bandgap, making them favorable for power electronic and optoelectronic applications. In addition, bandgap engineering of III-V alloys consisting in varying the alloy composition tunes the bandgap of III-nitrides, for example, from the infrared to the ultraviolet region of the electromagnetic spectrum, as shown in Fig. 1.1.[1]

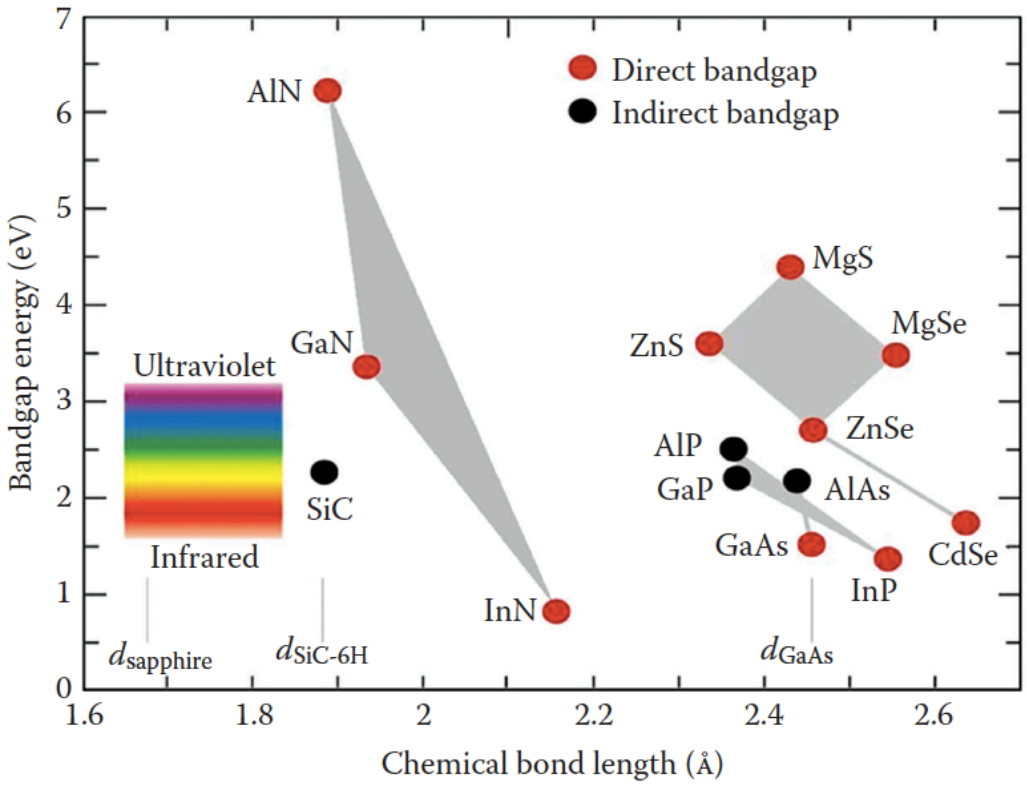

Figure 1.1. Bandgap of compound semiconductors versus the chemical bond length. (Adapted from Ref. 1)

In addition, the absence of toxic elements, such as cadmium and lead, makes III-V semiconductors more desirable to replace toxic II-VI materials in optoelectronic devices. In general, the III-V alloys crystallize in zinc blende and wurtzite structures, which differ from each other in the fourth interatomic bond direction along the (111) chain, shown in Fig. 1.2.[2]

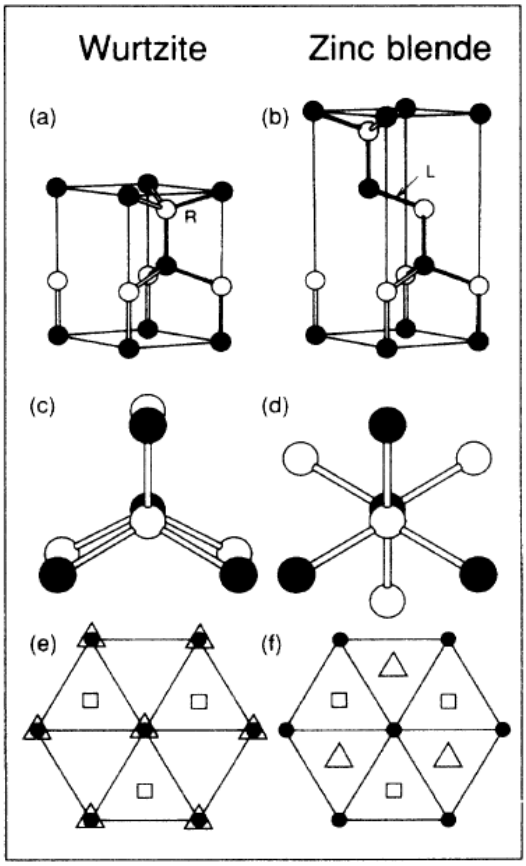

Figure 1.2. The crystal structures of wurtzite and zinc blende are shown. (Adapted from Ref. 2)

1.2 InAs, GaAs, and Their Applications

Indium arsenide (InAs) and gallium arsenide (GaAs) are direct bandgap semiconductors crystallizing in the zinc blende structure, shown in Fig. 1.2.[3] The structure shows face-centered cubic (FCC) translational symmetry, containing two interpenetrating

FCC lattices with a displacement of ¼[111]a along the diagonal of the unit cell. InAs has a relatively small bandgap (0.35 eV at 300 K), and an electron mobility μ of 32000 $cm^2/V \cdot s$ at 300 K.[4] The bandgap of GaAs is 1.424 eV, and with an electron mobility μ of 9400 $cm^2/V \cdot s$ at 300 K.[5,6] These direct bandgap characteristics and electrical transport properties are quite useful for high frequency field effect transistors (FET) and optoelectronic devices.[7-9]

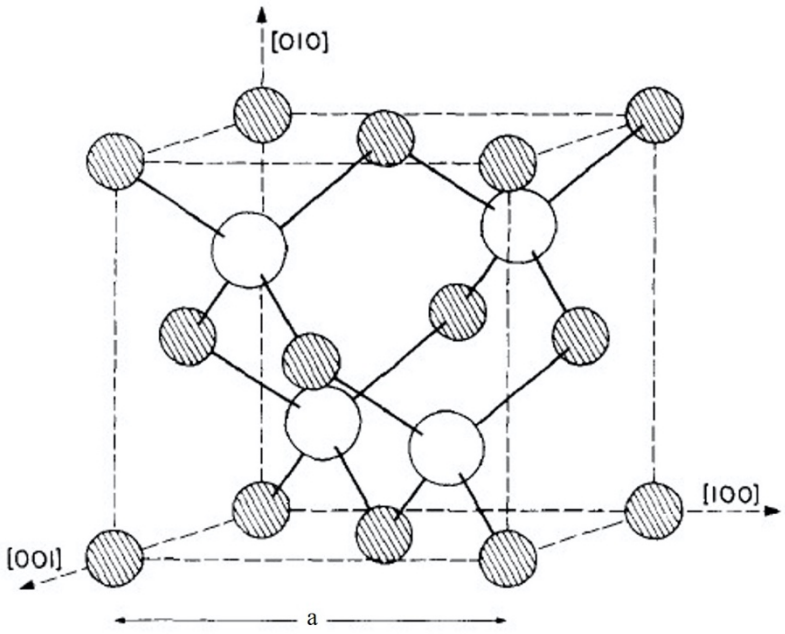

Fig 1.3. Conventional unit cubic for zinc blende structure. (Adapted from Ref. 3)

Quantum dots (QDs) with zero dimensional electronic properties utilized in QD solar cells have been extensively studied over the past decades. InAs QDs grown on GaAs substrates is one of the highly-investigated materials systems.[10-11] The lattice mismatch is 7.1% between the two materials, leading to the formation of self-assembled QDs following the strain-induced Stranski-Krastanov (S-K) growth mode. The confined states in QDs can be used as an intermediate band, sandwiched between two *n*- and *p*-type semiconductors,

to develop intermediate band solar cells (IBSCs). The extra states in the bandgap create two additional photons absorption paths, from the valence band to the intermediate band and from the intermediate band to the conduction band, as shown in Fig. 1.4. The additional photon absorption paths together with a conventional path through the valence band to the conduction band, resulting in a calculated efficiency of QD-IBSCs is 63%, potentially outperforming single junction cells.[12]

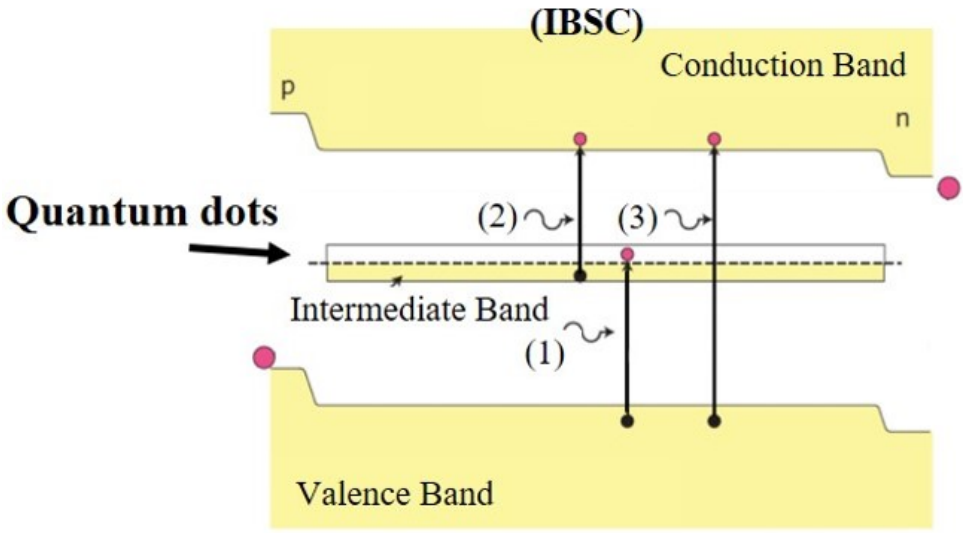

Fig 1.4. Energy band diagram of intermediate band solar cells. Photon absorption from the valance band to the intermediate band (1), the intermediate band to the conduction band (2), and the valence band to the conduction band (3). (Adapted from Ref. 12)

1.3 GaN and Its Applications

The most common thermodynamically stable structure of GaN is wurtzite, which has a hexagonal unit cell with six atoms of each type (Ga and N atoms). In the hexagonal structure, there are two lattice constants, *a* and *c*, representing the basal and height parameters, respectively. At a room temperature (T = 300 K), the edge length *a* is 3.189 Å, and the prism height *c* is 5.185 Å. On the other hand, non-centrosymmetric crystal structure of wurtzite GaN indicates the polar nature and its polarity is defined by the direction of III-

nitride bonding along the *c*-axis. This property makes the N- and Ga-polar GaN behave very different from each other in terms of chemical reactivity. Besides, there are two nonpolar $\{1\bar{1}00\}$ *m*- and $\{11\bar{2}0\}$ *a*-planes, perpendicular to the polar *c*-plane in the GaN wurtzite structure, shown in Fig. 1.5(a). The angle between two adjacent directions normal to *a*- and *m*-planes, for instance, $[11\bar{2}0]$ and $[10\bar{1}0]$, is 30°, shown in Fig. 1.5(b).[13]

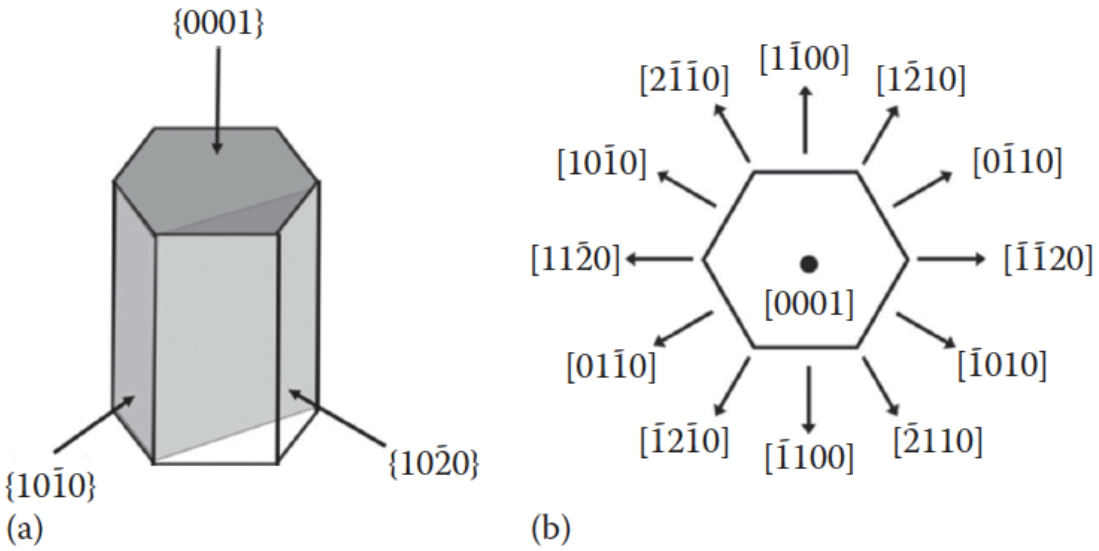

Figure 1.5. Schematic structure and crystal planes of wurtzite III-V nitride (a) Crystal plane of wurtzite III-nitride. (b) Top view of the (0001) *c*-plane. (Adapted from Ref. 13)

Usually, GaN is grown epitaxially on foreign substrates (sapphire or GaAs) by metalorganic chemical vapor deposition (MOCVD). The lattice mismatch between GaN layer and sapphire substrate results in a high dislocation density ($>1\text{x}10^9$ cm^{-2}), which is detrimental to the performance and reliability of GaN-based devices.[14] To use sapphire as a substrate addresses some drawbacks. For example, sapphire in the trigonal symmetry group with a poor symmetry lacks cleavage planes, making device processing difficult. In addition, sapphire is an insulator, requiring extra steps involving etching and wire bonding in order to make electric contacts. The emerging development of GaN-based applications

is due to the achievement in crystal growth and fabrication process to realize blue light-emitting diodes (LED) since the early 1990s.[15] Later, epitaxial laterally overgrown GaN with lower threading dislocations density was utilized to realize the laser diodes with a significantly extended lifetime.[16] In addition to its optical applications, GaN shows fundamental advantages over silicon in terms of a higher critical electric field, electron transport property, a low on-state resistance, etc. Such superior properties make it well-suited for the applications in high-power semiconductor devices.[17]

This thesis consists of six chapters, presenting the results of structural and optical properties analysis on III-V semiconductors used in the photovoltaics and power electronic applications.

In the second chapter, the characterization techniques used in this study are discussed, providing the working principles and frame works for the following chapters.

In the third chapter, the CuPt ordering of the group III elements in $Ga_{0.5}In_{0.5}P$ has been observed to vary during growth of InAs quantum dots capped with GaAs in a GaInP matrix. While ordering is not affected by the insertion of a GaAs layer, the growth of InAs quantum dots capped with GaAs results in ordered, partially ordered, or fully disordered GaInP. The results show that the degree of ordering depends on the deposition time of the InAs quantum dots and on the thickness of the GaAs capping layer.

In the fourth chapter, the formation of atomic steps and their coalescence into clusters at the surface of GaN epilayers grown on vicinal GaN substrates is reported. AFM studies show that steps meander on undoped GaN surfaces; while Mg doping increases the line tension of the steps producing well-defined periodic steps. For a low tilt, the steps involve a single basal plane (height = $c/2$). At a higher tilt, the steps involve two basal planes, with

a tendency towards step coalescence, generating surface regions with different orientations. It is also found that slower growth rates can enhance step-flow growth and suppress step bunching.

In the fifth chapter, the effects of inductively coupled plasma etching processes on GaN epilayers are reported. It shows that the etching damage on the films increases with the ions energy. Higher ion energy enhances the bombardment effect, leading to a rougher surface morphology, a decrease in the intensity of band-edge emission, and a higher yellow luminescence of GaN films. The etching damage, assessed via luminescence depth profiling on GaN films, suggests that the etching damage can be minimized by tuning the etching conditions, in order to improve the device performance.

In the sixth chapter, the anisotropic growth and non-uniform luminescence of Mg-doped GaN grown on trench patterns are described. The sidewall region with the lateral growth shows a faster growth rate but a lower acceptor density, compared to the flat region with the vertical growth. The regions with lateral and vertical growths of Mg-doped GaN films grown on trench patterns can be visualized from cathodoluminescence images.

In the seventh chapter, further possible studies of intermediate band solar cells and power electronic devices are discussed.

CHAPTER 2

EXPERIMENTAL METHODS

2.1 Transmission Electron Microscopy

The transmission electron microscope (TEM) is a powerful instrument for materials characterization, and it is essential to study nanoscale materials and devices. It offers high spatial and analytical characterization techniques through the conventional TEM imaging, scanning TEM imaging (STEM), electron diffractions, and spectroscopy. In the TEM instrument, electrons are controlled by the magnetic fields and interact with materials. As they pass close to the positive nuclei or other electrons of atoms, the Coulomb interactions scatter the electrons, creating TEM images, diffraction patterns, and other spectroscopic data. Depending on the applications, different electron beams can be selected to form a bright-field (BF) or a dark-field (DF) image in TEM, and different detectors are used to collect electron beams for BF and annular dark field (ADF) imagings in STEM, shown in Fig. 2.1.[18]

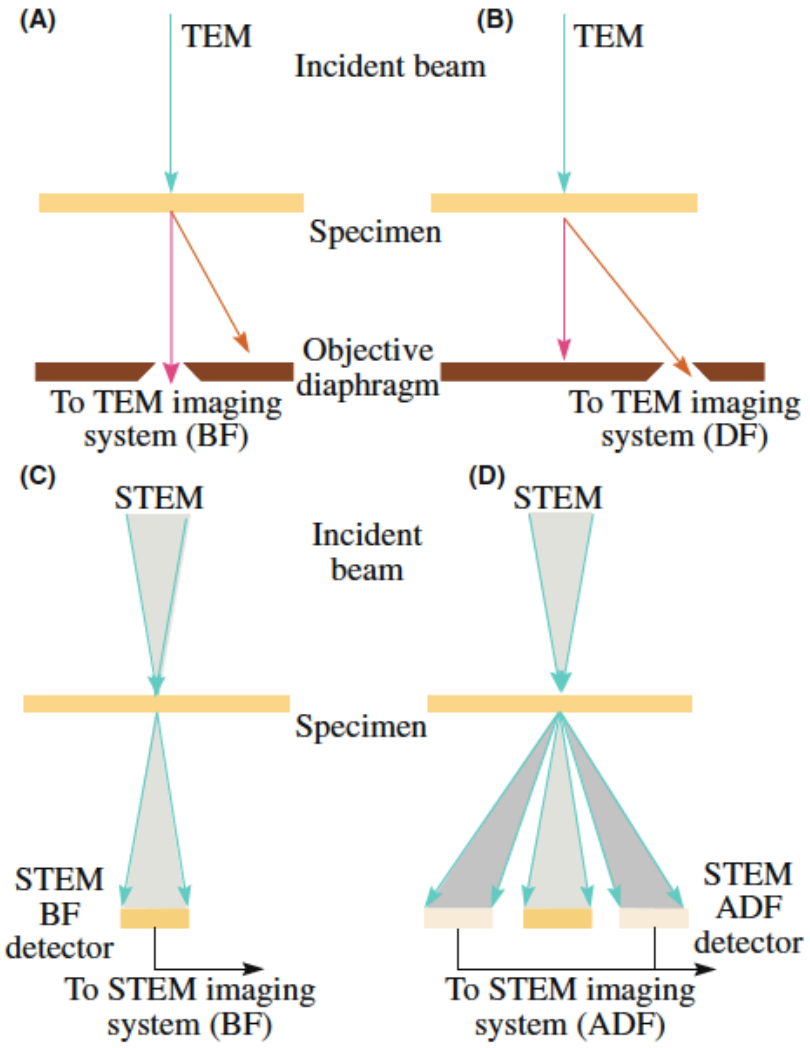

Figure 2.1. Comparison of the use of objective apertures and detectors in TEM and STEM. (Adapted from Ref. 18)

The phenomena of electron scattering can be divided to elastic and inelastic scatterings, in terms of scattered electrons with no loss of energy or with measurable loss of energy. Elastically scattered electrons are the major source of contrast in TEM images and diffraction. Inelastically scattered electrons are used for spectroscopic studies. On the other hand, depending on the electron wave nature, the scattered electrons can be separated into coherent and incoherent contributions, resulting in different angular distributions. In general, inelastic scattering is incoherent and occurs at very low scattering angle (<1°).

Elastic scattering is at relatively low angles (1~10°), and it becomes incoherent (i.e. Rutherford scattering) at higher scattered angles, shown in Fig. 2.2.[19]

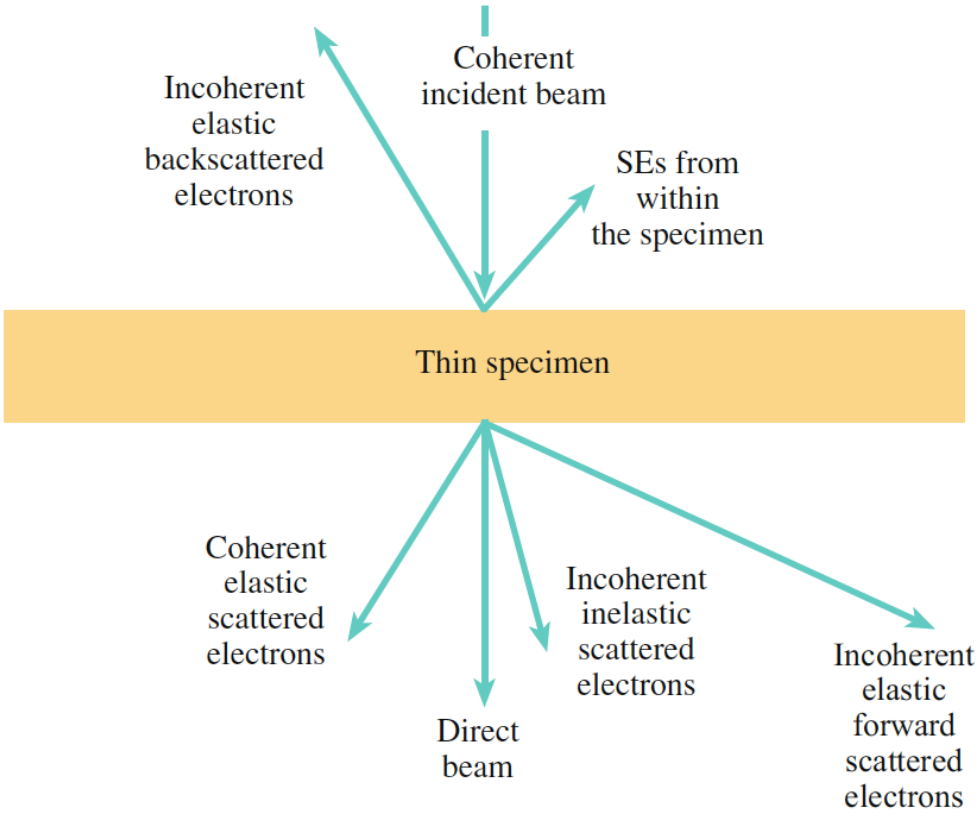

Figure 2.2. Different kinds of electron scatterings from a thin TEM specimen. (Adapted from Ref. 19)

As the electrons are elastically scattered by a periodic array of the atoms, a diffraction pattern (DP) is formed at the back focal plane of the objective lens in TEM. Each diffraction spot in the pattern corresponds to a set of planes in the real space, and the intensity of the diffracted beams strongly depends on the magnitude of the excitation error **s** to the exact Bragg condition. On the other hand, the Kikuchi lines produced by exact Bragg diffractions of inelastic scattered electrons appear as maps, connecting various zone axes. They provide more accurate crystallographic information and orient the specimen to the specific pole for TEM imaging and structural analysis. A selected area diffraction (SAD) aperture located

at the image plane can be inserted to the beam path, resulting in a SAD pattern corresponding to a particular area of the specimen. This diffraction technique is useful to study specific features and interfaces. As the SAD pattern shown in Fig. 2.3, two sets of DP obtained at the InGaN/AlN interface indicate the lattice mismatch between two layers and the nature of strain relaxation.

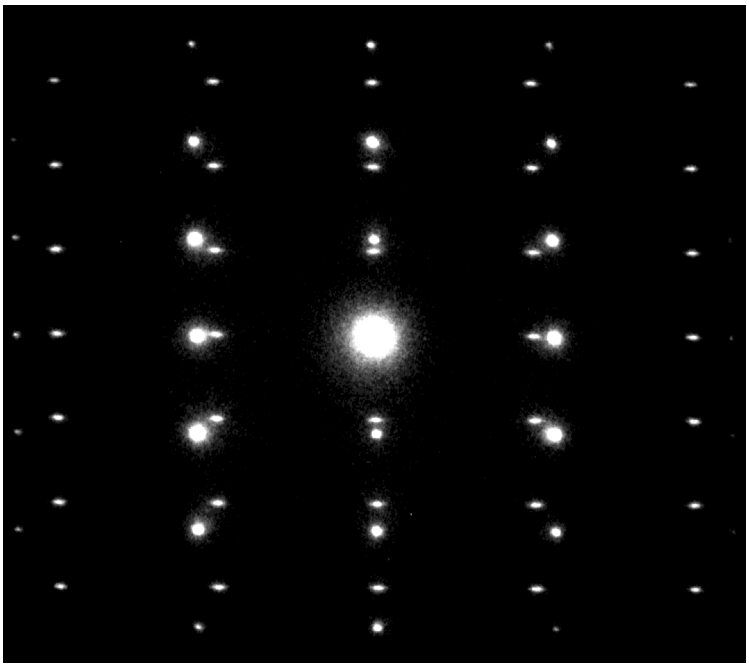

Figure 2.3. The selected area diffraction (SAD) pattern along <11$\bar{2}$0> zone axis obtained at the interface of InGaN/AlN layers.

Diffraction contrast imaging consists of collecting coherent elastic scattered electrons diffracted at specific Bragg angles. This technique is suitable for defect analysis because the presence of defects rotates the nearby diffracting planes, leading to the variation in the diffraction contrast. To obtain a strong diffraction contrast for defect analysis, the specimen is usually tilted to excite a certain diffracted beam corresponding to a specific set of planes, so called “two-beam condition.” Under two-beam condition, either the direct-beam or a diffracted beam is selected with a small objective aperture, to form a BF or a DF two-beam

image. A region without defect shows a uniform contrast, however, the region close to defects shows different contrast due to the bending of planes by the defects. Therefore, the region near the defects appears darker in the BF image, or brighter in the appropriate DF image. On the other hand, to compare the contrast produced by the crystal deformation under different diffraction conditions is used to determine the Burger vector $\boldsymbol{b}$ of defects. For instance, in the study of dislocations, $\boldsymbol{g} \cdot \boldsymbol{b}$ analysis gives an invisibility criterion when no contrast is observed for $\boldsymbol{g} \cdot \boldsymbol{b} = \boldsymbol{0}$ (i.e. the diffracting planes are parallel to the Burger vector $\boldsymbol{b}$).[20] As a result, the character of the dislocations (edge, screw, or mixed) can be understood by comparing the direction of the Burger vector $\boldsymbol{b}$ and the line direction of the dislocations. Figure 2.4 shows two-beam bright-field images of an InGaN layer grown on a GaN substrate. The threading dislocations are only visible in the "*g*=*m*" condition (right), but invisible in the "*g*=*c*" condition (left). It indicates the defects are edge-type dislocations, with the direction of the Burger vector of dislocations perpendicular to the dislocation line.

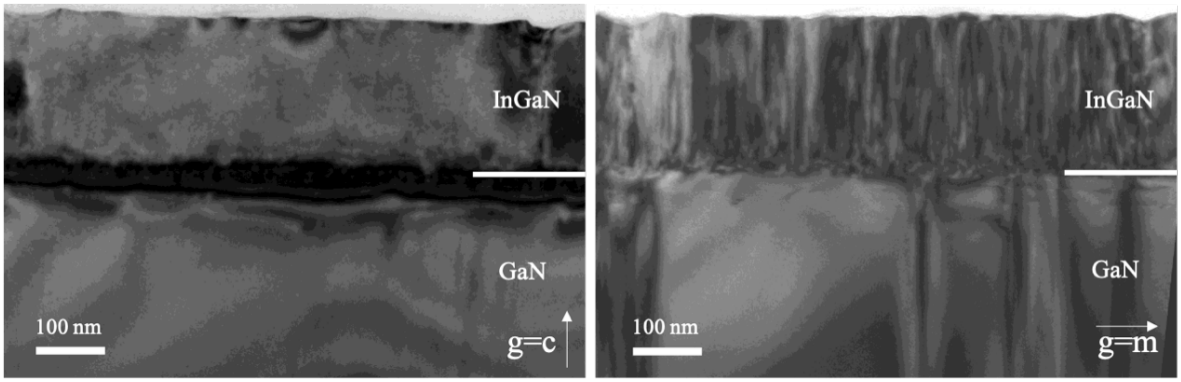

Figure 2.4. Two-beam bright-field images of InGaN layer grown on GaN substrate under two different diffraction conditions. Threading edge dislocations are only visible in "*g*=*m*" condition.

High-resolution TEM (HRTEM) is synonymous with phase contrast imaging, giving atomic-scale resolution images of the crystal structure. Unlike diffraction contrast imaging

which selects a single beam with the objective aperture, instead, HRTEM requires to collect multiple electron beams with no or a large objective aperture, to form the images. Phase contrast imaging depends on differences in phase between electrons leaving the TEM specimen. The wave function of electrons is determined by the atomic potential and a phase shift results as the phase is modified by the strength and spacing of periodic atomic potential. The electron wave exiting the specimen is imaged by the objective lens and magnified by the projection lens onto the screen. The phases of the diffracted waves are sensitive to the objective lens focus. On the other hand, the lens aberrations need to be sufficiently small because any phase shifts between the specimen and the screen can complicate the image interpretation. Therefore, the images strongly depend on the imaging parameters (sample thickness, defocus and lens aberration). Due to the interpretation complexity, image simulation is required for true understanding of the images.

In HRTEM, the specimen is tilted along low-index crystallographic zone axes in order to obtain images with atomic resolutions. For example, the <110> zone axis is chosen for HRTEM in zinc blende cross-sectional samples. For wurtzite structure, the projection along a $<11\bar{2}0>$ zone axis is used because it shows larger lateral atomic spacing comparing to a $<1\bar{1}00>$ zone axis. STEM imaging is also a high-resolution imaging technique by collecting scattered electrons. Depending on the collecting angle, high-angle annular dark-field (HAADF) images are formed by choosing high angle, incoherently scattered electrons (Rutherford scattering), without the effect of Bragg scatterings. Therefore, HAADF imaging is only sensitive to the atomic number of atoms in the specimen, and it is also referred as Z-contrast imaging, the heavier atoms with higher atomic numbers would appear brighter due to more scattered electrons collected by the HAADF detector.[21,22]

Figure 2.5 shows a HAADF image with a GaAs layer sandwiched by two GaInP layers. The average atomic number of GaAs is higher than that of GaInP, leading to a brighter contrast in the GaAs layer. On the other hand, a dumbbell configuration is observed in the GaAs layer, which is formed by atoms of a similar atomic mass (Z_{Ga}=31 and Z_{As}=33). However, P atoms are barely visible in the GaInP layers since the atomic mass of P (Z_P=15) is much smaller than that of Ga and In atoms.

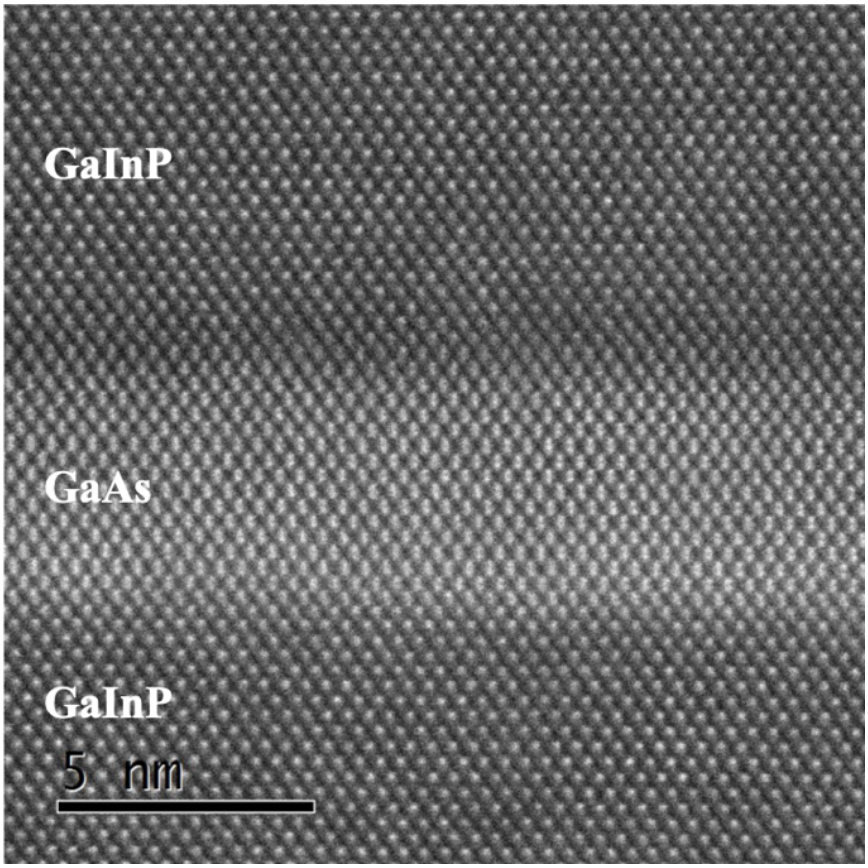

Figure 2.5. HAADF image taken along $[1\bar{1}0]$ zone axis shows a GaAs layer sandwiched by two GaInP layers. GaAs layer shows a brighter contrast than that of GaInP layers.

2.2 Cathodoluminescence Spectroscopy

Cathodoluminescence (CL) spectrometers equipped in a scanning electron microscope (SEM) is a unique tool to characterize optical, electronic and compositional properties of materials, coupling with the microstructure and morphology at the nanoscale. CL is the photon emission at characteristic wavelengths of materials as the result of high energy electron bombardment. As the electrons with sufficient energy strike the material, the generation of electron-hole pairs results from electrons from the valence band (VB) jumping up to the conduction band (CB). The recombination of electron-hole pairs occurs when the electrons return to the VB, producing photons with energy equal to the energy difference between the CB and VB, corresponding to the bandgap of the material ($E = h\nu = E_{CB} - E_{VB}$, when h is the Planck constant and ν is the frequency of the emitted light), as shown in Fig. 2.6.

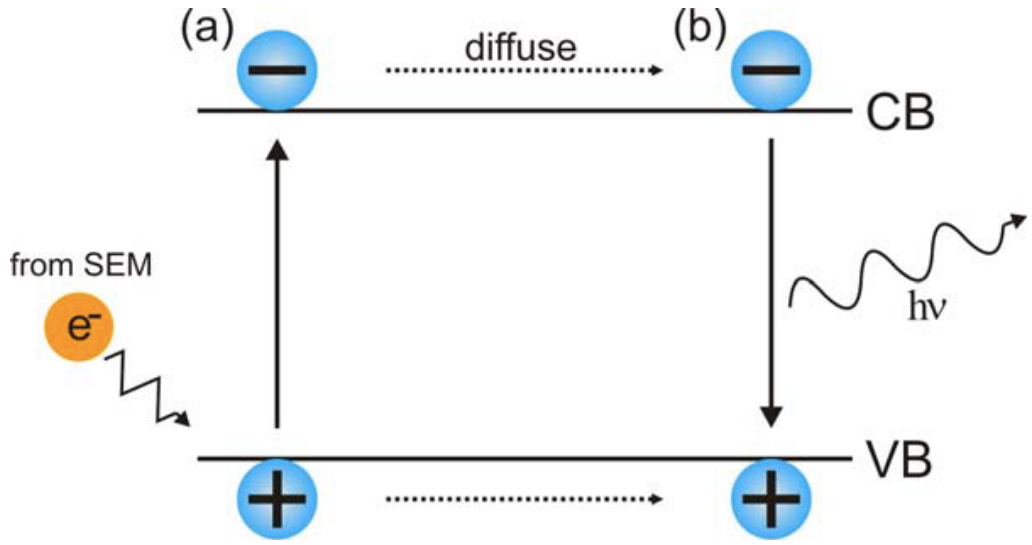

Figure 2.6. The generation of a photon in a semiconductor after electron bombardment. (a) Impinging electron promotes an electron from the valence band (VB) to the conduction band (CB), leaving a hole in the VB. (b) The electron recombines with the hole, generating a photon. (Courtesy of Dr. Alec Fischer)

In CL system, an electron beam is focused to excite the material within a small region, giving a higher spatial resolution over the photoluminescence (PL) technique. On the other hand, the excitation energy in CL is several keV, which is much higher than several eV used in the PL system, giving it the capability to characterize the materials with higher bandgaps. In addition, by changing the electron excitation energy to control the penetration depth of the incident electrons, it allows CL to probe electronic features within multilayer structures.[23] Furthermore, a monochromator in CL enables to select emissions at specific wavelengths, which can produce monochromatic 2D mapping to reveal compositional variation in materials.[24]

2.3 Atomic Force Microscopy

Atomic force microscopy (AFM) was first proposed by Binnig, Quate and Gerber in 1986, which is a combination of the concepts of scanning electron microscope (STM) and the stylus profilometer.[25] AFM is an imaging tool allowing to investigate the surface structure with an atomic resolution. Rather than other optical or electron microscopes focusing light or electrons to the surface to form images, AFM physically interacts with the samples with a sharp silicon tip mounted at the free end of the silicon nitride cantilever, shown in Fig. 2.7(left). The displacement of the free end of the cantilever can be determined by measuring the laser beam reflected off the cantilever into a split photodetector, shown in Fig. 2.7(right).[26,27]

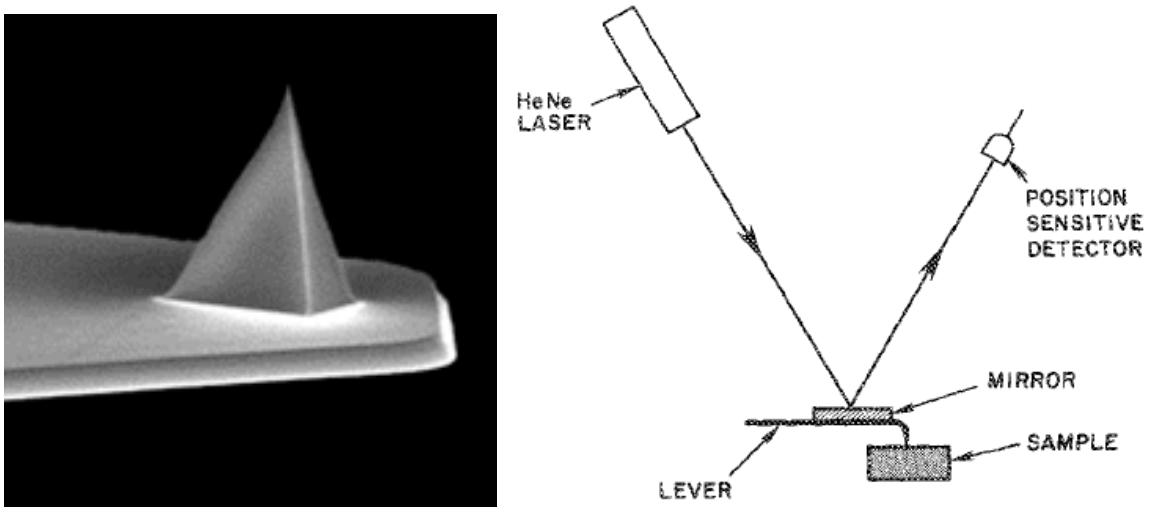

Figure 2.7. AFM silicon tip (left) and cantilever deflection detection scheme (right). (Adapted from Refs. 26 and 27)

AFM can be operated in different modes, depending on the applications.[25] In this work, ScanAsyst (SA) imaging technique based on the PeakForce Tapping mode is used to characterize the surface morphology. This novel technique is operated in a non-resonant mode, where the oscillation frequencies are below the cantilever resonance, and the *z*-position is modulated by a sine wave to avoid unwanted resonances at the turnaround points, giving the highest resolution imaging versus a number of AFM methods.[28]

CHAPTER 3

EFFECT OF InAs QUANTUM DOTS CAPPED WITH GaAs ON ORDERING IN $Ga_{0.5}In_{0.5}P$ (*)

3.1 Introduction

Photovoltaic solar cells fabricated with nanostructures such as quantum wells (QWs) and quantum dots (QDs),[29,30] are currently being researched in an attempt to exceed the Shockley-Queisser limit of single *p-n* junction solar cells.[31] Quantum-dot intermediate-band solar cells (QD-IBSCs) can potentially far outperform single junction cells, with a predicted efficiency of 63% under concentration.[12] The latter occurs when the materials selection is such that the barrier bandgap is 1.96 eV, and the QD fundamental absorption energy is 1.24 eV.[32] InAs self-assembled QDs embedded in a III-V matrix have demonstrated potential for photovoltaic applications.[33] However, the carrier escape caused by either thermal activation or tunneling from the QDs reduces the output voltage.[34] The choice of wide bandgap material for the barrier should suppress carrier escape, leading to higher efficiencies.[35] One material is $Al_{0.3}Ga_{0.7}As$ with a bandgap energy of 1.84 eV, which together with InAs QDs have been used to achieve transitions to an intermediate band energy close to the ideal theoretical value.[36,37]

Another material is $Ga_{0.5}In_{0.5}P$, which has produced record high-efficiency tandem solar cells,[38,39] and has some advantages over AlGaAs, such as lower excess carrier recombination velocity at heterojunction interfaces,[40] and better resistance to oxidation

*Results included in this chapter have been published as:
P.-Y. Su, H. Liu, R. M. S. Kawabata, E. C. Weiner, R. Jakomin, M. P. Pires, R. R. King, P. L. Souza, and F. A. Ponce, *Effect of InAs quantum dots capped with GaAs on atomic-scale ordering in $Ga_{0.5}In_{0.5}P$*, J. Appl. Phys. **125**, 053104 (2019).

and radiation damage.[41] The bandgap for free standing $Ga_xIn_{1-x}P$ reportedly varies as $E_g = 1.34 + 0.73\,x + 0.7\,x^2$.[42] The resulting values in the neighborhood of x = 0.5 are given in Table 3.1. In order to achieve the ideal value of 1.95 eV for IBSCs, the composition for *strain free* films would be x ≈ 0.55. However, tensile strain causes the bandgap to significantly decrease for x > 0.5 compared to strain-free values.[43] Taking into consideration the mismatch strain with GaAs, the value would be (by extrapolation) x = 0.6,[43] but the crystalline quality would be quite poor if the critical thickness for plastic deformation is exceeded.[42]

Table 3.1. Lattice parameter and band gap energy for $Ga_xIn_{1-x}P$ in the range of interest. The respective lattice parameters for GaAs, GaP, and InP are 5.6536, 5.4504, and 5.8687 Å. The band gap energy for GaP is 2.26 eV, and for InP is 1.34 eV.

x	a	Eg	Comment
0.500	5.6596	1.880	Lower if ordered along {111} planes
0.510	5.6554	1.894	Lattice matched to GaAs
0.550	5.6387	1.953	Ideal for IBSCs

When lattice matched to GaAs, GaInP has a tendency towards CuPt ordering of the group-III sublattice. The monolayer superlattices are formed along $[\bar{1}11]$ or $[1\bar{1}1]$ directions. They are observed in TEM along the $[110]$ projection, with the group-V element positioned above the group-III elements in the dumbbell configuration, shown in Fig. 3.1.[44]

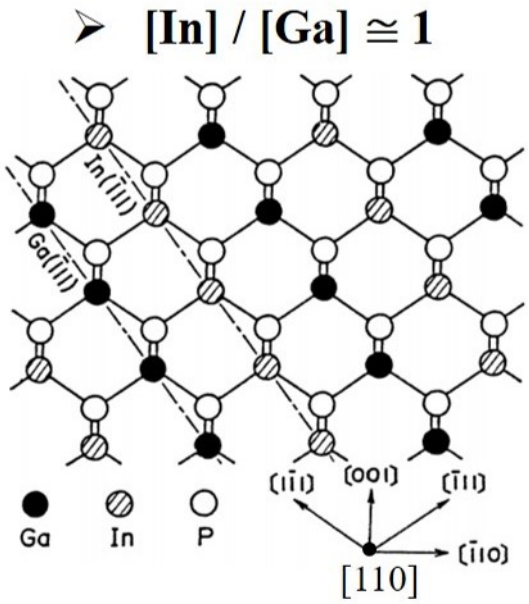

Fig. 3.1. Structure model of ordered GaInP along the [110] projection. The alternating Ga- and In- planes lying along {111} directions are shown. The group-V elements position above the group-III elements. (Adapted from Ref. 44)

The room-temperature value of the band gap is 1.9~1.92 eV for the disordered phase, and 1.83~1.85 eV for the ordered phase.[44,45] As a material candidate for intermediate band solar cells, the bandgap shrinkage due to ordering can be detrimental, significantly deviating from the optimal energy bandgap of 1.95 eV for IBSCs. Therefore, understanding $Ga_{0.5}In_{0.5}P$ ordering is necessary to develop and optimize the performance of QD-IBSCs based on this material. It is known that the degree of ordering of GaInP strongly depends on the growth conditions and also on substrate misorientation.[46,47] Although ordering of GaInP has been extensively investigated in the 1980's and 1990's, only few reports are available on the transition between ordered and disordered GaInP in the presence of InAs QDs.

In this work, the effect of the presence of InAs quantum dots and their GaAs capping layer on the ordering of the GaInP barrier have been investigated. Our goal has been to

optimize the conditions for growth of InAs QDs capped with GaAs in a GaInP matrix. The GaInP optical properties vary from ordered to disordered has been observed, depending on the time of deposition of the InAs and on the thickness of the GaAs capping layer. An explanation for the transitions between ordered and disordered based on the nature of InAs QD growth is provided. High-angle annular dark-field (HAADF) imaging and bright-field imaging in a scanning transmission electron microscope (STEM) are used to correlate the GaInP microstructure with the presence of InAs QDs. Cathodoluminescence (CL) spectra exhibit peaks with two distinct wavelengths corresponding to disordered and ordered GaInP. The optical properties thus observed are consistent with the microstructure observed by STEM.

3.2 Experimental Details

The InAs-QD/GaAs/GaInP samples were grown by metalorganic vapor phase epitaxy on (001) GaAs substrates in an Aixtron AIX 200 horizontal reactor at 100 mbar. A pre-growth treatment at 720 °C for de-oxidation was applied to the GaAs substrates for 15 min under AsH_3 overpressure. The hydrogen carrier gas flow rate was 8 liters/min. The precursors were tri-methyl gallium (TMGa), tri-methyl indium (TMIn), phosphine (PH_3) and arsine (AsH_3). GaAs was grown at 630 °C at a growth rate of 0.16 nm/s and a V/III ratio of 160. The Ga/(Ga + In) gas phase ratio was calibrated for growth of $Ga_{0.5}In_{0.5}P$ layers at 675 °C, with a growth rate of 0.27 nm/s and a V/III ratio of 345.

A schematic drawing of the thin film structure and a photoluminescence spectrum of the region comprising the InAs QD and GaAs capping layer, common for all samples, is shown in Fig. 3.2. The InAs QDs emit at ~950 nm and the GaAs capping layer at ~825 nm at 10K. The growth sequence was as follows: The common base consists of a 200-nm-thick

GaAs buffer layer grown on an *n*-doped (001) GaAs substrate, followed by a 350-nm-thick $Ga_{0.5}In_{0.5}P$ layer. The active region consists of an InAs QD layer and GaAs capping film. The QDs are grown with various deposition times at 490 °C, with a V/III ratio of 6.4. After the QD growth, the temperature was kept constant for 12 s, and afterwards the layer was capped with GaAs during the first 23 or 34 s, while the temperature was being raised to 675 °C, with a ramp rate of 46 °C/min. After reaching 675 °C, the temperature was held constant for 1.5 min to achieve surface stabilization. Then, a 90 nm thick $Ga_{0.5}In_{0.5}P$ layer acting as the barrier was grown; and the growth sequence of the active region and barrier was repeated four times. An extra QD layer was grown at the top surface for the purpose of determining the dot morphology and distribution. The dot density was measured over an area of 9 μm^2 using a Veeco MultiMode V atomic force microscope (AFM) with a tip driven at frequencies above 100 kHz.

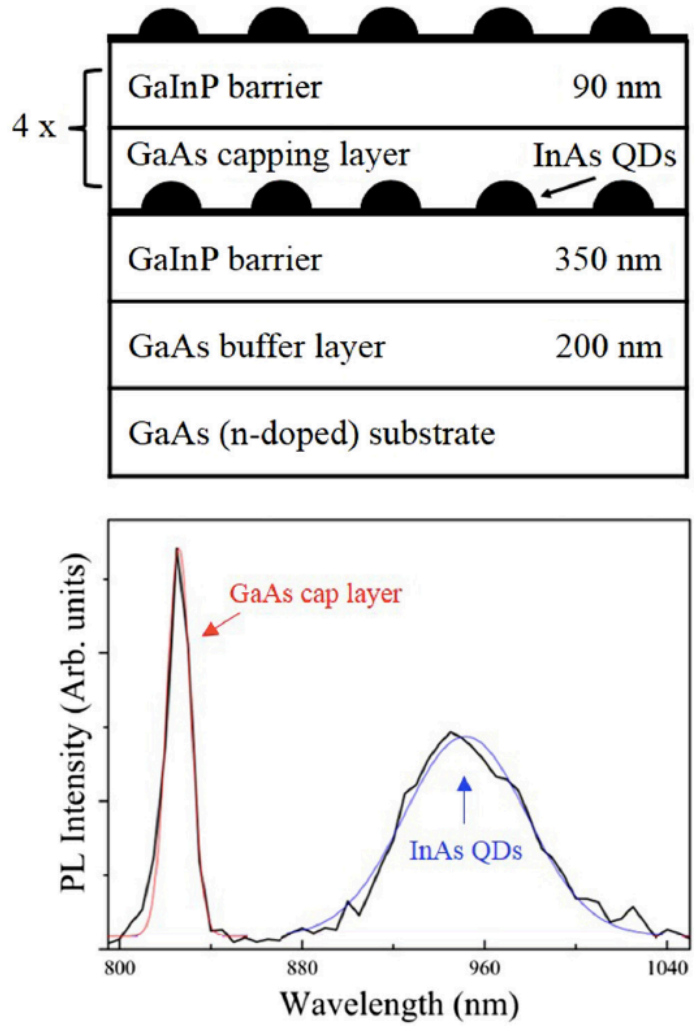

FIG. 3.2. Schematic diagram of the InAs QD/GaAs/GaInP thin film structure and photoluminescence spectrum taken at 10 K, showing emission from the InAs QD and GaAs capping layer. Best-fit Gaussian curves give peak emissions at 823 and 952 nm, and FWHM of 11 and 54 nm, for the GaAs capping layer and the InAs QDs, respectively. (Courtesy of Dr. Mauricio Pires)

This report focuses on two parameters of the QD structure: (a) the capping layer thickness, and (b) the InAs deposition time. The samples are listed in Table 3.2. Sample A does not contain InAs and serves as reference. The deposition time for InAs was 2.4 s for Samples B and C, 3.0 s for Sample D, and 3.5 s for Sample E. The GaAs capping layers thickness was 6 nm for Samples A and B, and 9 nm for Samples C, D, and E.

Table 3.2. GaAs cap layer thickness and InAs deposition time, and their effect on the GaInP microstructure. The capping layer thickness, the average QD height and morphology, and the GaInP degree of ordering was determined from cross-section TEM images. An average QD density of about 1.6 $x10^{10}$ cm^{-2} was determined from AFM images over an area of 9 μm^2.

Sample ID	Thickness of GaAs cap layer (nm)	InAs deposition time (s)	QDs height /morphology	GaInP microstructure
A	6	0	-	Ordered
B	6	2.4	4 nm height lens-shaped	Disordered
C	9	2.4	4 nm height lens-shaped	Upper part ordered, lower part disordered
D	9	3.0	9 nm height spool-shaped	Ordered
E	9	3.5	10 nm height spool-shaped	Ordered

Cross-section samples were prepared for STEM by mechanical wedge polishing followed by argon-ion milling with a 2 kV accelerating voltage at liquid N_2 temperatures. The morphology of the InAs QDs was studied using bright-field and HAADF detectors, in an aberration-corrected JEOL ARM 200 STEM. The intensity in HAADF images depends on the atomic number of the elements, which is approximately proportional to $Z^{1.7}$ for a detector internal angle of 75 mrad.[48,49] The relative intensity for molecular columns in the HAADF images is given in Table 3.3. Note that GaAs and InP columns should give a close intensity, while GaP columns should be darker and InAs should be brighter. Bright field STEM images are used, with a detector semi-angle of 10 mrad, to obtain strain contrast that complements the HAADF images for identification of the QD morphology.[50]

Table 3.3. Z contrast in STEM-HAADF images. The atomic column intensity is proportional to $Z^{1.7}$.

	Columnar number Z	$Z^{1.7}$	Relative intensity
GaP	46	671	1
InP	64	1176	1.8
GaAs	64	1176	1.8
InAs	82	1793	2.7
GaInP	55	909	1.4

Photoluminescence spectra were obtained at 10 K, using a 532-nm 10-mW laser and a liquid nitrogen-cooled Ge detector, to probe the infrared optical properties of the InAs QDs and of the GaAs capping layers. The optical properties in the visible range of the GaInP layers were investigated using CL spectroscopy. The CL system consists of a scanning electron microscope equipped with a spectrometer having a 1200 lines/mm grating and a GaAs photomultiplier tube. The CL spectra were acquired at 298 K, with an acceleration voltage of 3 kV, an electron beam current of 7 nA, a scan magnification of 3,000 times, and an entrance slit of 3 μm. Average spectra were obtained using a raster mode over an area of 20 μm^2.

3.3 Experimental Results

Figure 3.3 shows the CL spectra of the samples in this study. Luminescence peaks with maxima at 670 nm (1.85 eV) and 645 nm (1.92 eV) corresponding to the ordered and disordered group-III sublattices, respectively. Our reference Sample A, with no InAs present, shows a single emission peak at 670 nm corresponding to ordering of the group-III sublattice. On the other hand, when InAs QDs are present (Samples B to E), emission at ~ 645 nm is sometimes observed, corresponding to the disordered phase of $Ga_{0.5}In_{0.5}P$.

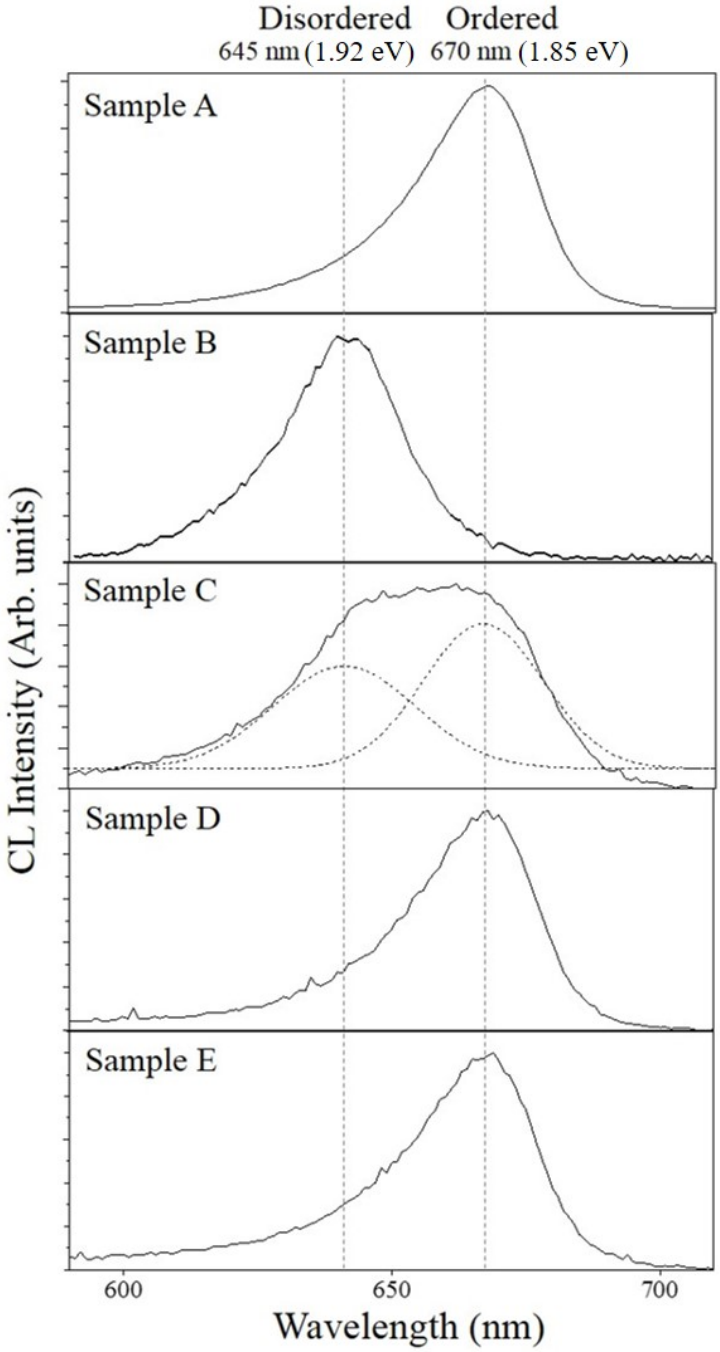

Fig. 3.3. Cathodoluminescence spectra of the InAs QD/GaAs/GaInP samples. Sample A shows an ordered GaInP emission peak. Sample B shows a disordered GaInP emission peak. In Sample C, both ordered and disordered GaInP emission peaks are observed. Best-fit Gaussian curves give peak emissions at 645 and 669 nm, and FWHM of 30 and 25 nm, corresponding to disordered and ordered GaInP, respectively. Samples D and E exhibit ordered GaInP emission peaks. The CL spectra were acquired at 298 K, with an acceleration voltage of 3 kV, an electron beam current of 7 nA, scan magnification of 3000 times, and using a slit of 3 μm. (Courtesy of Hanxiao Liu)

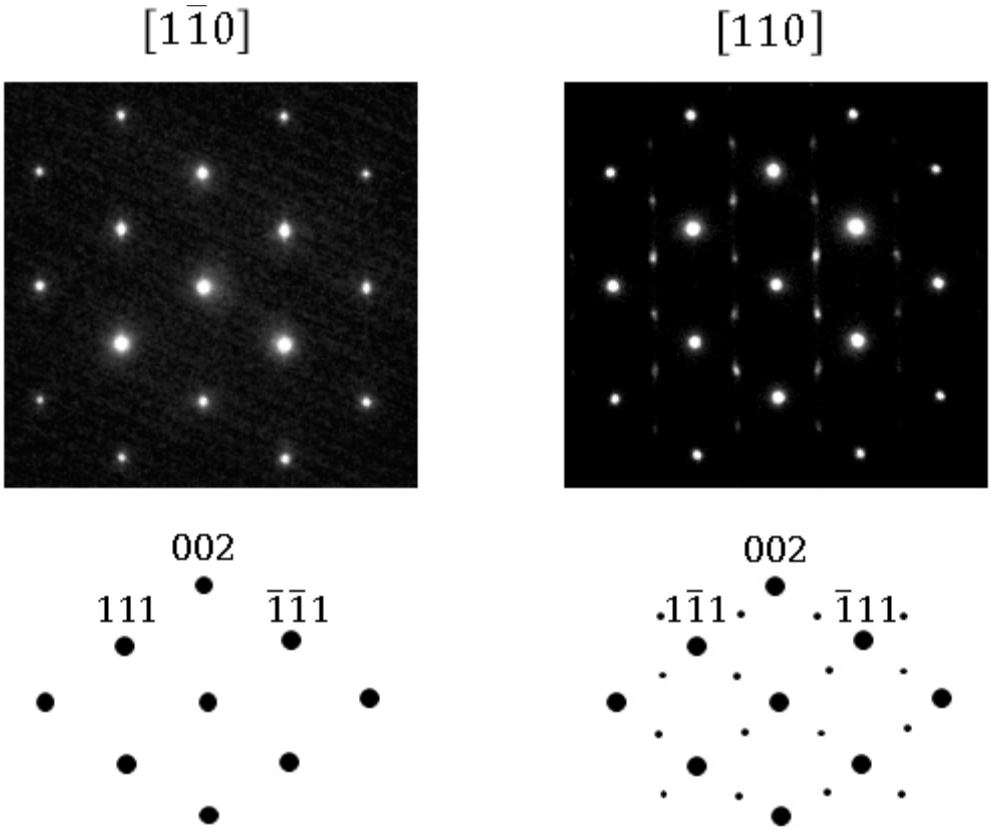

FIG. 3.4. Transmission electron diffraction patterns of Sample A taken along the [1$\bar{1}$0] zone axis (left) and [110] zone axis (right): Superstructure reflections along [$\bar{1}$11] and [1$\bar{1}$1] directions are only observed in the [110] projection.

In Figure 3.4, selected-area diffraction patterns (SADP) of a GaInP layer in Sample A are shown. Along the [1$\bar{1}$0] zone axis, the typical zincblende diffraction pattern is observed. On the other hand, along the [110] projection, extra superstructure spots located halfway along the [$\bar{1}$11] and [1$\bar{1}$1] directions are observed, corresponding to ordered structures, with sequential InP and GaP {111} planes. Note that ordering can happen only along one of those directions. Their presence in the electron diffraction patterns indicates that ordered domains along both directions coexist in our samples. The streaks along the [001] direction in the extra spots are associated with the coexistence of ordering along the

two {111} directions.[51] They imply that ordered domains are irregular in size, and that they are oriented nearly parallel to (001) planes.

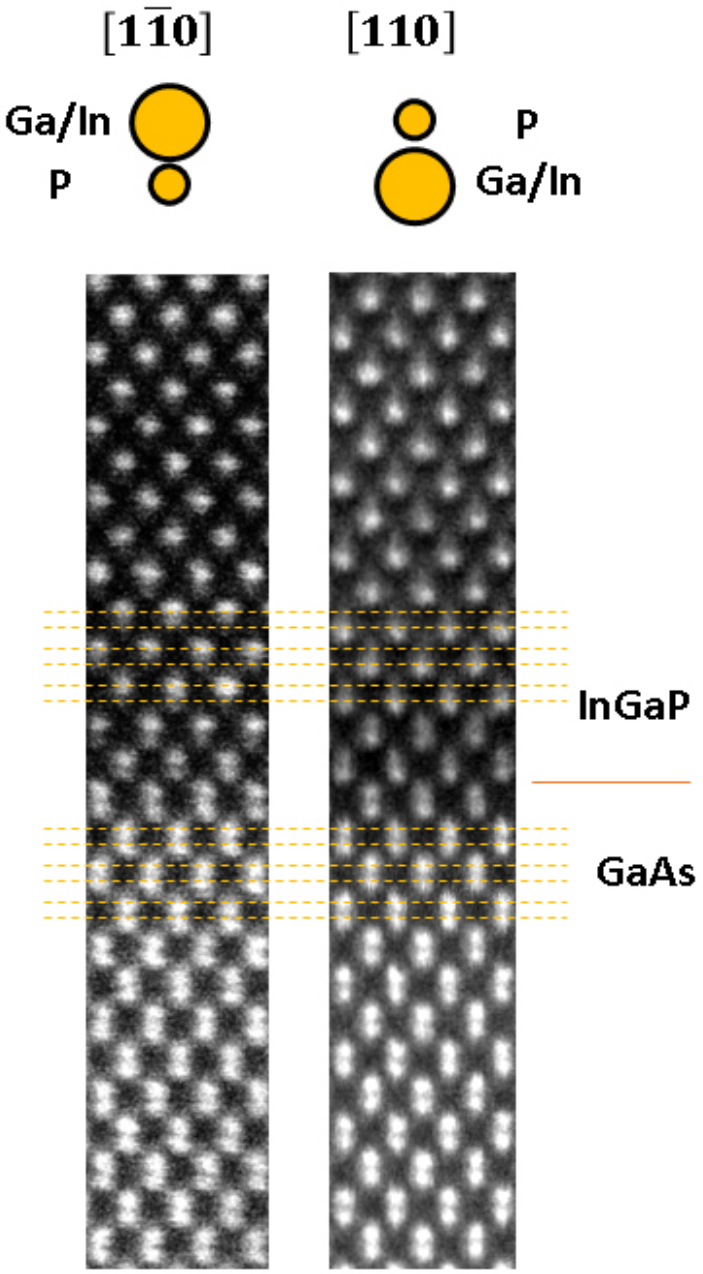

FIG. 3.5. HAADF images of Sample A viewed along the [1$\bar{1}$0] zone axis (left) and [110] zone axis (right). The dumbbells in GaInP and GaAs are clearly visible. The phosphorus atoms are much smaller than the Ga, In, and As atoms. The P column is located on top of the group-III column when viewed along the [110] zone axis. The orientation of the dumbbell is reversed when viewed along the [1$\bar{1}$0] zone axis. Therefore, HAADF images can be used to determine the polarity of the lattice leading to ordering.

Figure 3.5 shows HAADF images taken along orthogonal $[1\bar{1}0]$ and [110] projections, showing the relative positions of the Group-III and Group-V elements.In GaAs, the Ga-As dumbbell is rather symmetric, due to the close atomic number between Ga and As. In GaInP the situation is different, with the phosphorus atoms being much smaller than the Group-III atoms. The reversal of the relative positions of the columns in GaInP is evident in HAADF images under the two projections. This characteristic is used to identify the polar direction in our STEM images, i.e. which atom is on top of which. This is helpful to confirm the observation is along the [110] projection, and to determine whether local ordering exists. The STEM images presented from here on were taken along the [110] projection, determined in the manner prescribed here.

The HAADF image from Sample A in Fig. 3.6 shows ordered GaInP structure with alternating In- and Ga- planes, with a zig-zag pattern in the image that indicates local ordering shifting between the $[\bar{1}11]$ and $[1\bar{1}1]$ directions. As Table III points out, the {111} planes with brighter contrast correspond to In-P planes with larger Z value, alternating with the darker Ga-P planes. The Fourier-filtered images in the lower row are of selected superstructure spots (½$[\bar{1}11]$ or ½$[1\bar{1}1]$), and show regions with $[\bar{1}11]$ ordering (lower left) and others with $[1\bar{1}1]$ ordering (lower right) in Fig. 3.6. The domains have a tendency to extend laterally, and are separated by domain boundaries.[52-54]

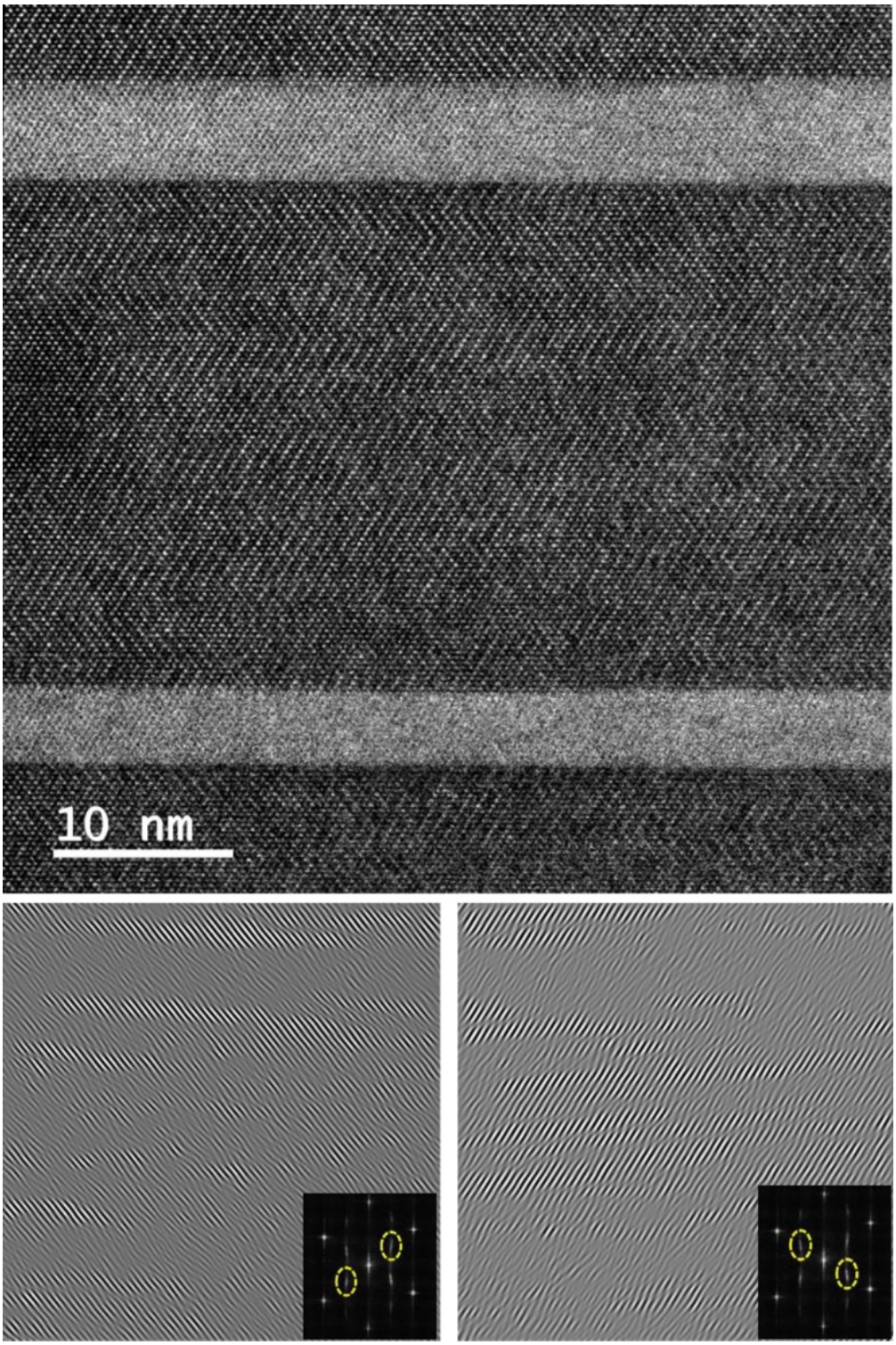

FIG. 3.6. HAADF image of Sample A viewed along the [110] zone axis (top) and Fourier-filtered images (lower row). The Fourier-filtered images of selected superstructure spots (½$[\bar{1}11]$ or ½$[1\bar{1}1]$ highlight the ordered $(\bar{1}11)$ planes (bottom left) and $(1\bar{1}1)$ planes (bottom right).

3.3.1 Effect of the GaAs Capping Layer Thickness on GaInP Ordering

The thickness of the GaAs film capping the InAs QDs can affect ordering in the GaInP barriers. In this section the results are present for samples with the same InAs QD deposition time of 2.4 s, but capped with different GaAs film thicknesses. Sample B in Table 3.2 has GaAs capping thickness of 6 nm, and presents in Fig. 3.3 a GaInP single peak emission at 645 nm (1.92 eV), indicating a disordered phase. Sample C, on the other hand, with a GaAs capping thickness of 9 nm, presents two emission peaks, one at 645 nm (as in Sample B), and another at 670 nm (1.85 eV), the latter indicative of an ordered phase.

Figure 3.7 shows HAADF and BF images of the active region in Sample B (with 6 nm GaAs cap thickness), where GaInP is disordered in regions without QDs [Fig. 3.7 (top row)], as well as in the presence of QDs [Fig. 3.7 (bottom row)]. Fast Fourier transform (FFT) diffractograms of selected areas are included as inserts to show evidence of disordered lattices.

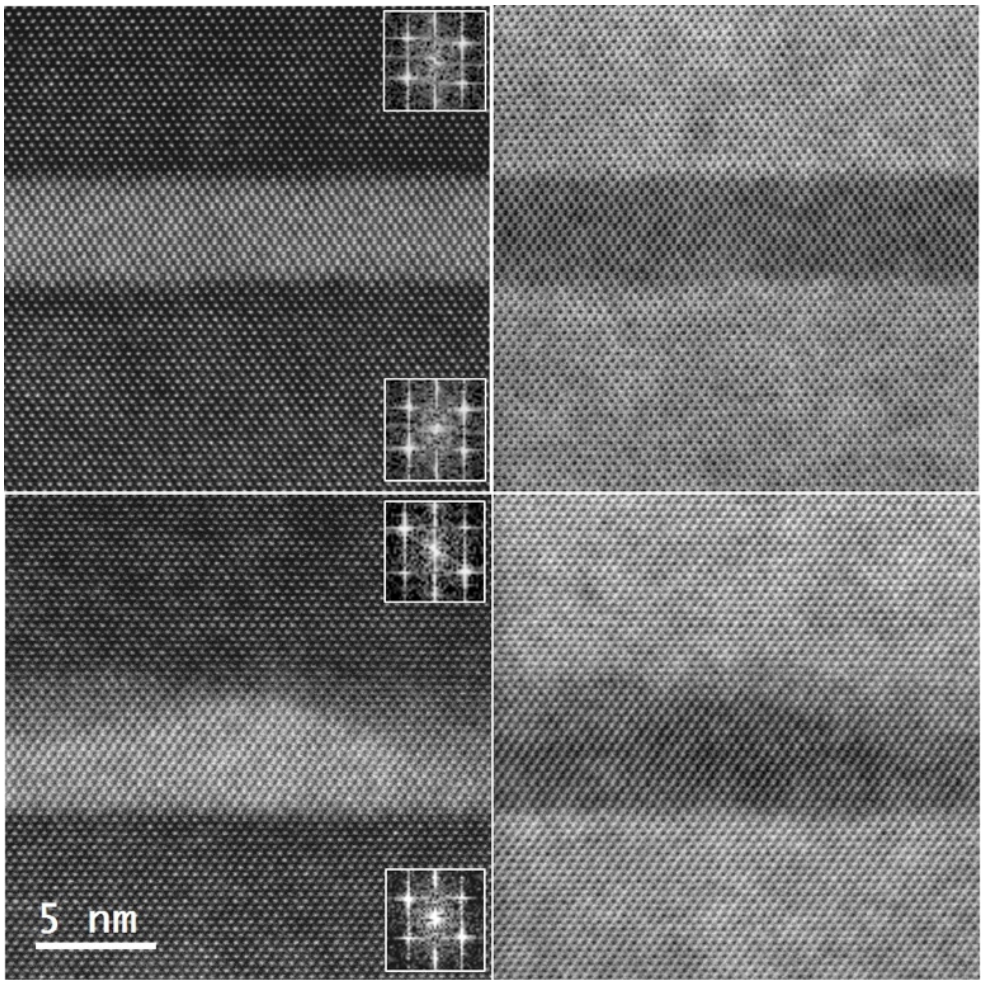

FIG. 3.7. Cross-sectional STEM images of Sample B, viewed along the [110] zone axis. (Top row) A HAADF image of the InAs QD layer capped with GaAs in a region without InAs QDs with inserted diffractograms that show no ordering in both top and bottom GaInP barrier layers (left), and a bright-field image of the same region showing the absence of QDs (right). (Bottom row) Portion of the same layer but in the vicinity of an InAs QD, with HAADF image showing disordered GaInP barriers (left) and a bright-field image of same region showing the presence of a lens-shaped QD (right).

Figure 3.8 shows HAADF and BF images of the active region in Sample C with 9 nm GaAs cap thickness. Ordering of {111} crystal planes is observed generating superstructure spots at half the {111} distance of the normal (disordered) lattice in the selected-area

diffractograms. Figure 3.8 (top row) is of a region without QDs, where ordering in GaInP is observed on both sides of the GaAs layer.

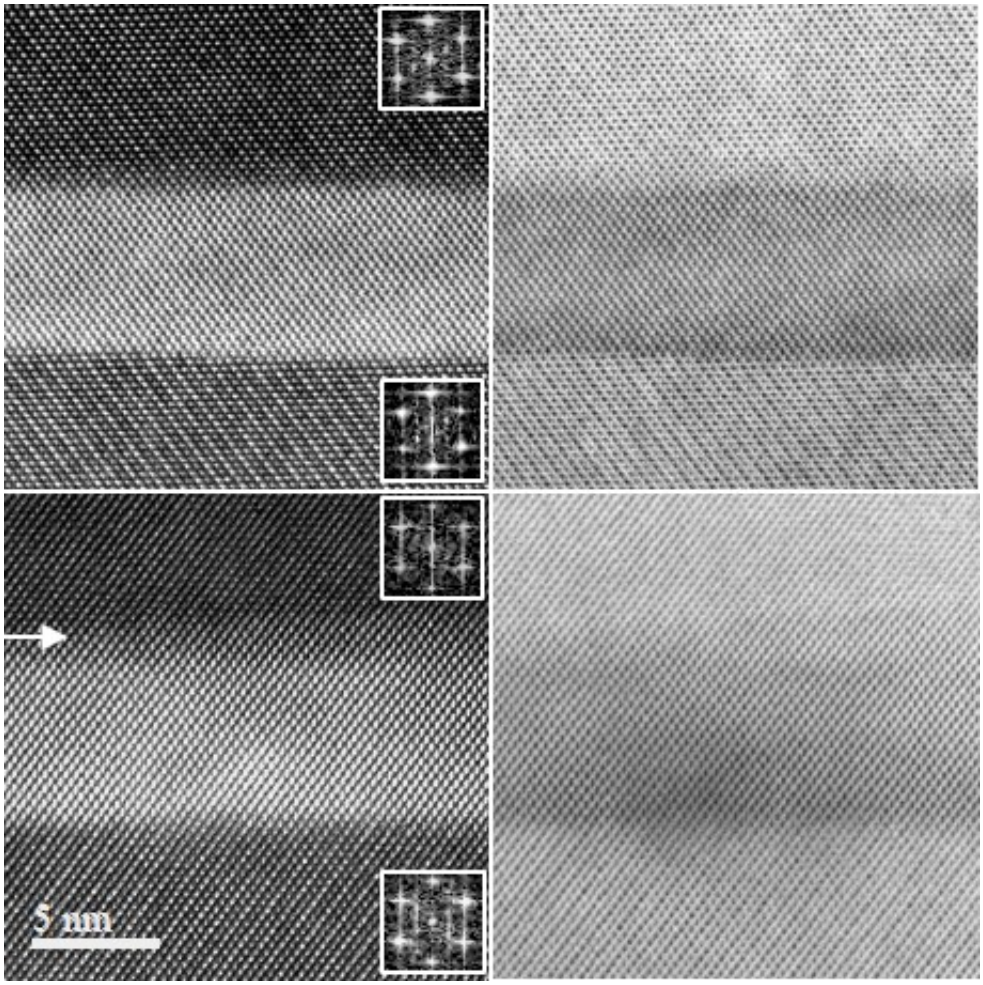

FIG. 3.8. Cross-sectional STEM images of Sample C, viewed along the [110] zone axis. (Top row) A HAADF image of the InAs QD layer capped with GaAs layer in region without InAs QDs and diffractograms showing ordering in both top and bottom GaInP barrier layers (left) and a bright-field image of the same region showing the absence of QDs (right). (Bottom row) Portion of same layer in the vicinity of an InAs QD, with HAADF image showing top disordered and bottom ordered GaInP barriers (left), arrow showing an indium-rich layer above the GaAs capping layer, and a bright-field image of same region showing the presence of a lens-shaped QD (right).

Figure 3.8 (bottom row) corresponds to a region in which a QD is present, where the GaInP below the QD layer is ordered, while it is disordered above the GaAs capping layer.

Ordered regions under the InAs QD layer and disordered regions in the neighborhood above InAs QDs have been observed throughout this sample. Since QDs, GaAs cap, and GaInP barrier layers repeat in the structure (see Fig. 3.2), the ordering state in the GaInP barriers must transition from disordered to ordered at some point in the barrier layer. Figure 3.9 shows the transition from disordered to ordered, which occurs in the top region (15 nm) of the 90 nm-thick GaInP barrier.

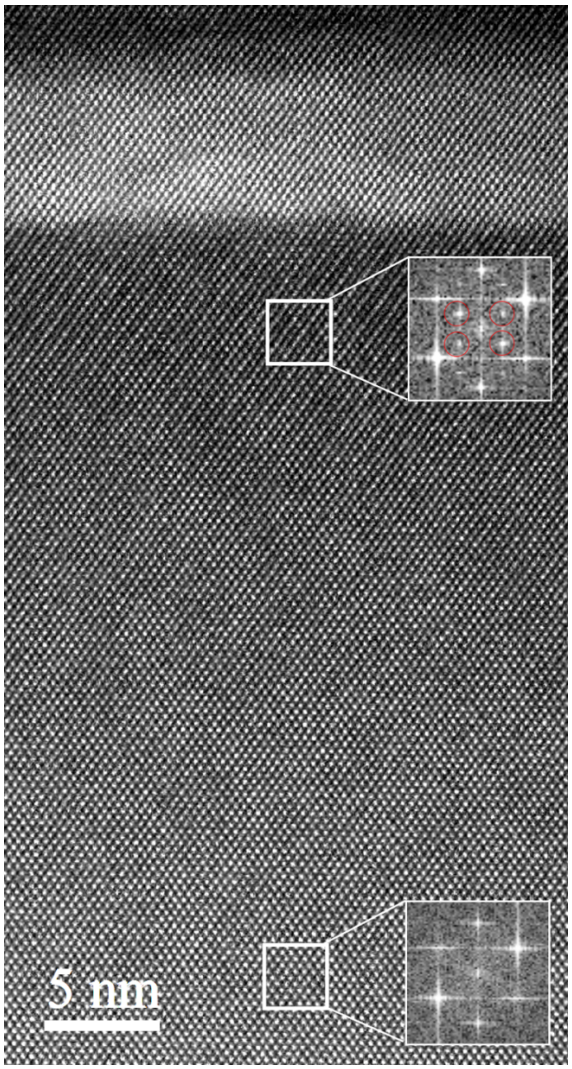

FIG. 3.9. HAADF image of Sample C viewed along the [110] zone axis. FFT patterns are shown of the indicated square regions from the bottom (disordered) and from the top (ordered) of the GaInP barrier. The superstructure spots are circled in the FFT of the upper region.

3.3.2 Effect of InAs Deposition Time on GaInP Ordering

In addition to the thickness of the capping layer, the deposition time of InAs also influences ordering in the GaInP layers. Now considering three samples, have all with 9 nm capping layers and with InAs deposition times of 2.4 s (our already-mentioned Sample C), 3.0 s (Sample D), and 3.5 s (Sample E). Their CL spectra are included in Fig. 3.3. As already mentioned, the two emission peaks observed in Sample C indicate that both ordered and disordered regions occur in the GaInP barrier layers. However, it is interesting to note that the spectra for Samples D and E only show one emission peak at 670 nm, attributed to the ordered phase of GaInP.

In the case of Sample C in Fig. 3.8(bottom row), the lens-shaped InAs QD has an average height of 4 nm and is fully covered by the 9 nm GaAs capping layer. The HAADF image shows disordered GaInP is on top of the GaAs capping layer. Increasing the InAs deposition time to 3.0 s [Sample D in Fig. 3.10(top row)] results in larger QDs whose height exceeds the thickness of the GaAs capping layer. In which case, the QD is observed to take the shape of a *spool* (bounded by two flat disks) whose height of 9 nm is defined by the thickness of the capping layer.[37] For Sample E, with a deposition time of 3.5 s, in Fig. 3.10(bottom row), the QD presents a more pronounced spool-shape. In this case, the thickness of the InAs layer on top of QD is about 1.5 nm, thicker than the 0.5-0.7 nm for sample D. The interface between the GaAs capping layer and the GaInP barrier of Samples D and E is more pronounced than in the case of Sample C, with the GaInP layer presenting an ordered structure immediately above the interface.

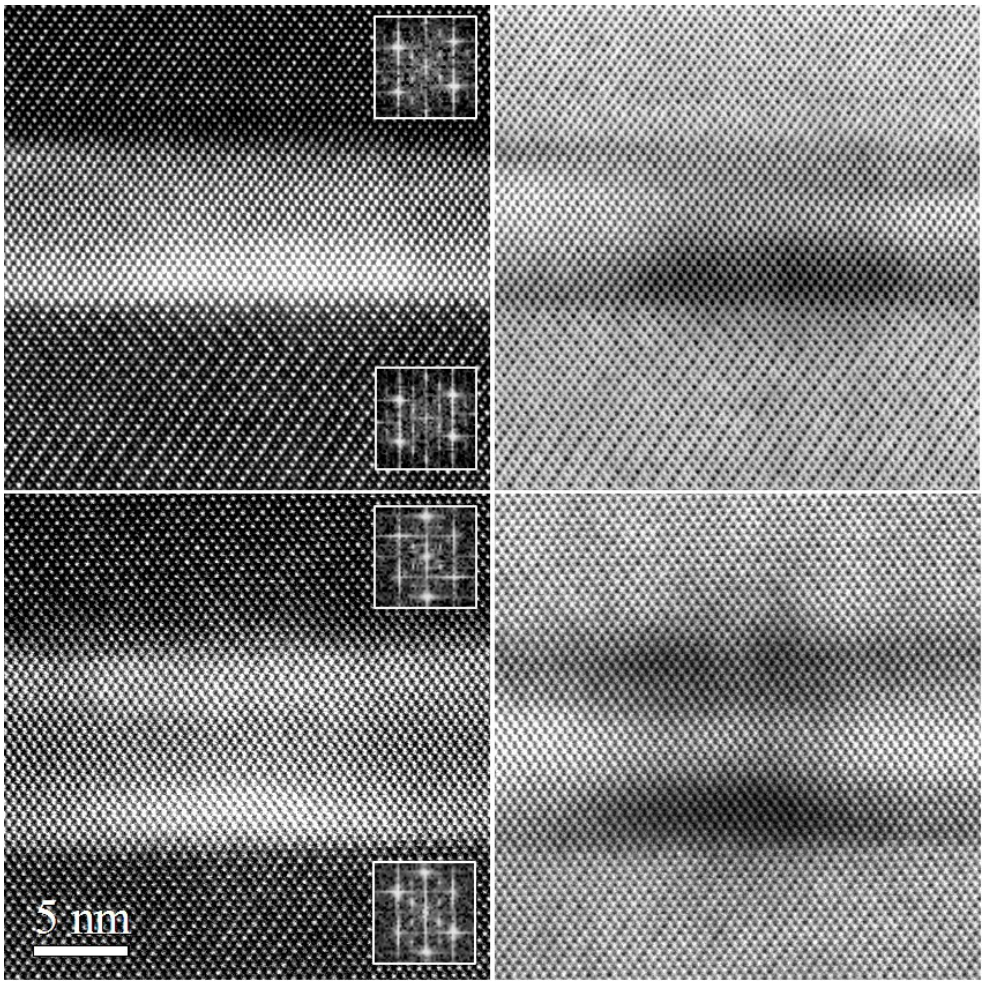

FIG. 3.10. Cross-sectional STEM images of InAs spool-shaped QD layers capped with GaAs viewed along the [110] zone axis. (Top row) For Sample D, HAADF image of an InAs QD layer capped with GaAs that shows ordered top and bottom GaInP barrier layers (left), bright-field image of the same region (right). (Bottom row) For Sample E, HAADF image showing ordered top and bottom GaInP barriers (left), bright-field image of the same region (right).

3.4 Discussion

GaInP thin films do not exhibit complete ordering.[55] An example is the imperfect ordering observed in Fig. 3.6, where ordered domains switch from $(\bar{1}11)$ to $(1\bar{1}1)$ planes, in a zig-zag pattern. The degree of ordering causes a variation in the bandgap of GaInP. Such variation has been modeled using a long-range order parameter (LRO) η, that ranges

from 0 to 1 for randomly distributed to fully ordered structures.[55] In practice, the typical GaInP is only partially ordered at the atomic scale, with a LRO $\eta \approx 0.4$-0.6. The peak emission energy for ordered GaInP (1.85 eV) corresponds to $\eta = 0.44$.[28] On the other hand, fully disordered GaInP with $\eta = 0$ has been observed experimentally.[56]

The nature of epitaxial growth from the vapor phase becomes important in the following discussion. The Stranski-Krastanov (S-K) growth mode describes the early stages of growth of InAs on GaAs (or equivalently on GaInP). The lattice mismatch between film and substrate is accommodated pseudomorphically by compressive elastic strain in the InAs layer. The compressive strain energy increases with layer thickness, making indium incorporation into the film more difficult, resulting in accumulation of indium in the gas phase next to the InAs surface, shown in Fig. 3.11(a).[57] At a certain thickness (of about two monolayers), two-dimensional growth is suppressed,[58] and the fraction of indium in the gas phase at the gas/solid interface increases.[57] At a critical point, three-dimensional InAs islands nucleate, producing additional surface area that has the effect of relaxing the misfit strain, shown in Fig. 3.11(b). Some of the accumulated indium in the gas phase gets absorbed by the nucleated islands, contributing to their growth.[59] In this manner, the formation of InAs islands consumes some of the accumulated indium in their vicinity. At a certain island size, the strain is relaxed by the introduction of misfit dislocations at the substrate interface, shown in Fig. 3.11(c). When the InAs island is capped with GaAs, misfit dislocation loops form around the island, minimizing the lattice mismatch strain.[60]

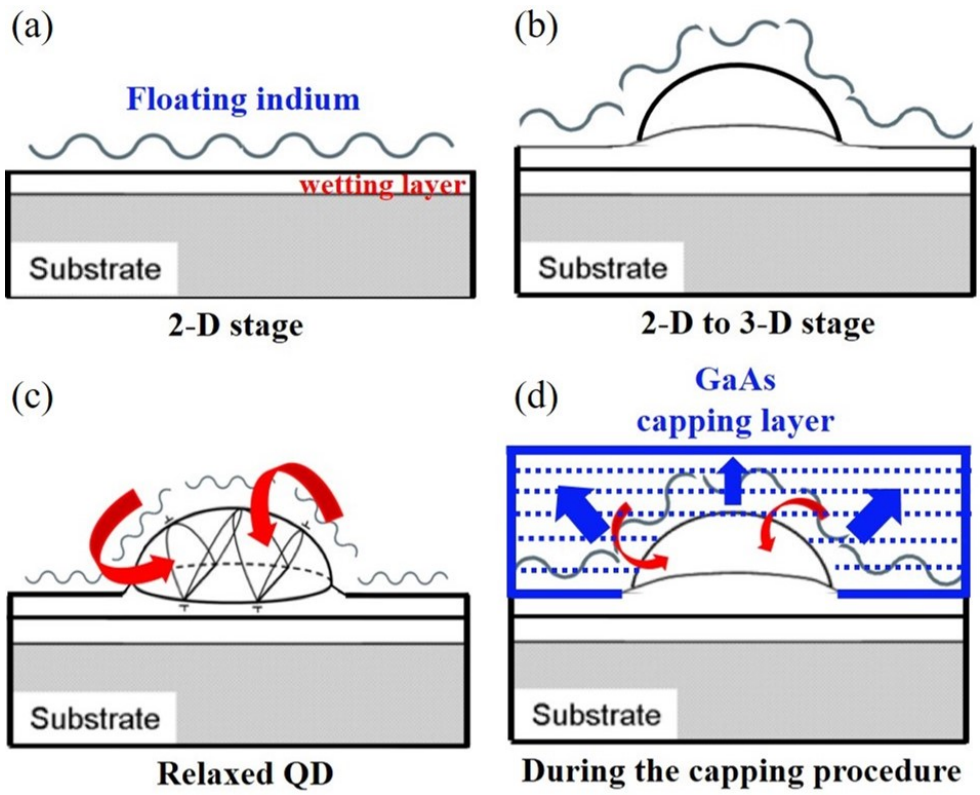

Fig. 3.11. Floating indium above the InAs QDs. (a) Floating indium above the 2-D InAs wetting layer. (b) At the critical later thickness, the 3-D InAs island starts to nucleate. (c) At the critical size, misfit dislocations are introduced at the interface between the 2-D layer and 3-D island. (d) Floating indium is absorbed during the GaAs capping procedure.

The absence of InAs islands causes excess indium in the gas phase to accumulate at the growth front. During subsequent growth, like GaAs capping, the excess indium will progressively be incorporated into the film, shown in Fig. 3.11(d).[57] On the other hand, when the InAs is already relaxed, little or no accumulated indium in the gas phase will be present at the growth front.

As the sufficient amount of InAs is deposited, larger QDs whose height is greater than the thickness of the GaAs capping layer are formed. The formation of spool-shaped QDs observed in Fig. 3.10 is related to the growth sequence: GaAs is deposited at 490°C, the temperature is then increased up to 675°C, at which point growth of the following GaInP

barrier is started. During the ramp up in temperature, the exposed InAs at the top of the QDs has a chance to diffuse laterally, wetting the surface of the GaAs capping layer, in a similar fashion to the early wetting of InAs on GaAs described by the S-K growth mode. The formation of this InAs top layer has been described in terms of thermodynamic arguments.[61] Some interdiffusion of the InAs and the GaAs may also take place.

Recall that it has been observed the following: (1) disordered GaInP immediately above thin GaAs capping layers that are not thick enough to consume the excess indium, which accumulates across the whole growth surface during the InAs QD growth step (Sample B, Fig. 3.7). (2) Localized, disordered GaInP directly above the InAs QDs with thicker GaAs capping layers that have consumed some of the excess surface indium [Sample C, Fig. 3.8(bottom row)]. (3) Localized, ordered GaInP directly above the wetting layer and away from QD, with the capping layer having consumed most of the excess surface indium [Sample C, Fig. 3.8(top row)]. (4) A transition from disordered to ordered in the GaInP barrier layers directly above an InAs QD, after remaining surface indium has gradually been consumed by the GaInP growth (Sample C, Fig. 3.9) or by the upper top layer of the spool-shaped InAs QD (Samples D and E, Fig. 3.10).[37]

The driving force for group-III sublattice ordering in GaInP at the atomic level is the formation of phosphorus dimers on the growth surface.[62,63] It is hypothesized that one mechanism consistent with the observations is that excess indium which persists for some time on the growth surface interferes with the formation of phosphorus dimers, or with the strain they induce on neighboring atoms in the top monolayers of the growing GaInP, thus interfering with the formation of group-III sublattice ordering in the GaInP. This mechanism would account for all the observed order/disorder phenomena.

In addition, it has been observed that the 1/2[115] X-ray diffraction peaks that correspond to GaInP ordering are significantly less pronounced for GaInP compositions that deviate by about 7-8% indium from the case with equal mole fractions of Ga and In ($Ga_{0.5}In_{0.5}P$) and the case lattice matched to Ge ($Ga_{0.505}In_{0.495}P$), indicating a lower tendency for the ordered phase to form at compositions away 50% Ga/ 50% In.[64] Measurement of GaInP composition well away from Ga/In = 1 in the disordered GaInP would be consistent with either or both proposed mechanisms, while a composition closer to unity would be more consistent with excess indium on the growth surface being able to thwart the ordering process independently of being incorporated at a higher concentration in the GaInP film.

It must be also clarify, in support of the above discussion that the observed microstructure of Sample C agrees well with the CL spectrum in Fig. 3.3. The peak at 645 nm is from the disordered lower portion of GaInP above InAs QDs. And, the emission peak at 670 nm corresponds to regions away from the QDs (both laterally as well as vertically distanced). It is possible that the greater strain in the GaInP barrier immediately above InAs QDs also impairs the driving force toward group-III sublattice ordering, contributing to disorder in the GaInP barriers above the quantum dots.

3.5 Conclusions

In summary, the ordering of $Ga_{0.5}In_{0.5}P$ used as barrier material for InAs QDs with GaAs capping layers for application in quantum-dot intermediate-band solar cells has been studied. Ordering reduces the bandgap of the ternary material threatening its adequacy for the development of such devices. It is found that both the thickness of the GaAs capping layer and the InAs deposition time affect the GaInP ordering. STEM and CL observations

show that the GaInP structure is fully ordered in the presence of GaAs layers without InAs. In the presence of InAs, fully ordered GaInP is not always observed. It has been attributed to the excess indium that builds up at the growth surface due to difficulty of incorporating indium during growth of the InAs QDs. If the excess indium is not fully consumed during the growth of the InAs QDs, or incorporated in the GaAs capping layer, an indium-rich layer or partial monolayer will be present on the growth surface at the onset of the GaInP barrier layer. Such a deviation from the ideal [In] to [Ga] ratio in the species adsorbed on the growth surface interferes with the group-III sublattice ordering mechanism, and gives rise to a disordered GaInP layer. Therefore, for a GaInP barrier material to be used in QD-IBSCs, smaller quantum dots and thinner capping layers are, in principle, advisable, since they should lead to a bandgap closer to the ideal value, which corresponds to the disordered phase.

ACKNOWLEDGMENTS

The materials were grown by Dr. Maurício P. Pires and his team at PUC-Rio. This research was funded by the Advanced Research Projects Agency-Energy (ARPA-E), U.S. Department of Energy, under Award Number DE-AR0000470, and by the National Science Foundation (NSF) and the Department of Energy (DOE) under NSF CA No. EEC-1041895. The research at PUC-Rio was partially supported by the Fundacão de Amparo a Pesquisa do Estado de Rio de Janeiro (FAPERJ), the Financiadora de Estudos e Projetos (FINEP), and by the Conselho Nacional de Desenvolvimento Científico e Tecnológico (CNPq). The authors gratefully acknowledge assistance in the determination of density of QDs by AFM from Dr. C. M. Almeida at INMETRO in Rio de Janeiro.

CHAPTER 4

EFFECTS OF LOW-ANGLE OFF-AXIS GaN SUBSTRATE ORIENTATION AND GROWTH RATES ON THE SURFACE MORPHOLOGY OF Mg-DOPED GaN EPILAYERS (*)

4.1 Introduction

There is much current activity in the development of gallium-nitride-based thin film device structures for applications in optoelectronic and high-power electronic devices.[65,66] This is due to the superior fundamental properties of these materials compared to SiC and Si, such as high bandgap energy, low intrinsic carrier concentrations, high critical breakdown electric fields, and high thermal conductivity.[66] For many of these applications it is essential to use high crystalline quality GaN substrates with low dislocation densities,[67] and to grow films with smooth planar morphologies. Recent approaches consist of coalescing the dislocations into bunches, resulting in high quality GaN regions. GaN crystals grown by hydride vapor phase epitaxy (HVPE), available today, present relatively low dislocation densities ($<10^7$ cm^{-2}) that propagate along the [0001] growth direction. However, the surface consists of pits and micropipes, and the dislocation distribution on the surface is not uniform. Far from the center of the pits, the dislocation density is low, but at the center of the pits the dislocation density is very high.[68,69]

---

*Results included in this chapter have been published as:

H. Liu, P.-Y. Su, Z. Wu, R. Liu, and F. A. Ponce, *Influence of substrate misorientation on the optical properties of Mg-doped GaN,* Journal of Applied Physics, 15 May 2020, Vol. **127**, 195701.

P.-Y. Su, H. Liu, S. Wang, Z. Wu, R. Liu, and F. A. Ponce, *The effect of low-angle off-axis GaN substrate orientation on the surface morphology of Mg-doped GaN epilayers*. Submitted to Journal of Applied Physics, 1 June 2020.

Another drawback is that for surfaces closely oriented to the basal plane, two-dimensional nucleation leads to the formation of hillocks and roughening of the surface.[70] On a positive note, steps in slightly misoriented (miscut) substrates facilitate lateral step-flow growth, which helps retain a smooth surface morphology and reduces unintentional doping.[71-73] On the other hand, growth on highly misoriented GaN surfaces has been reported to result in inhomogeneous compositional distribution in ternary compounds.[74]

The stability of step-flow growth can be affected by the growth temperature, by the surface step density, and by extended crystal defects and impurities, which may cause atomic steps to coalesce into step bunches.[75,76] Several mechanisms for step bunching have been proposed, including interactions between steps and adatoms migration on vicinal surfaces.[77-79] Since roughening of the growth front can significantly degrade the film quality and adversely affect device performance,[80,81] it is important to understand the nature of step evolution and mass transport on vicinal surfaces.

This study focuses on the effects of substrate misorientation and epitaxial growth rates on the morphology of Mg-doped GaN (GaN:Mg), for the purpose of understanding step flow growth and *p*-type doping efficiency at a microscopic-scale. The surface morphology was studied using atomic force microscopy (AFM) and cross-section transmission electron microscopy (TEM). The morphological evolution is explained in terms of surface step interaction and mass transport. A correlation has been established between growth surface morphology and growth rates.

4.2 Experimental Details

GaN epitaxial layers were grown by metal-organic chemical vapor depositions (MOCVD) on 350-μm-thick GaN substrates with the [0001] direction tilted toward a

<$1\bar{1}00$> direction, by an angle θ ranging from 0.3° to 4°, as shown in the schematic diagram in Fig. 4.1. The Ga and N sources used were trimethylgallium (TMGa) and ammonia (NH_3); the carrier gas was hydrogen. Unintentionally-doped GaN (*u*-GaN) layers were grown at 980 °C using TMGa and NH_3 flow rates of 270 and 50000 sccm, respectively, at a growth rate of 60 nm/min. Silicon-doped (GaN:Si) layers were grown at 980 °C with TMGa, NH_3, and silane (SiH_4) flow rates of 270, 50000, and 34 sccm, respectively; at a growth rate of 60 nm/min. Magnesium-doped GaN (GaN:Mg) layers were grown at 920 °C with TMGa, NH_3, and bis(cyclopentadienyl)magnesium (Cp_2Mg) flow rates of 90, 70000, and 1430 sccm, respectively, at a growth rate of 4 nm/min, for a Mg concentration of 1×10^{19} cm^{-3}, measured by secondary ion mass spectroscopy. Post-growth thermal activation of GaN:Mg was performed by rapid thermal annealing at 860 °C for 20 mins in a nitrogen atmosphere.

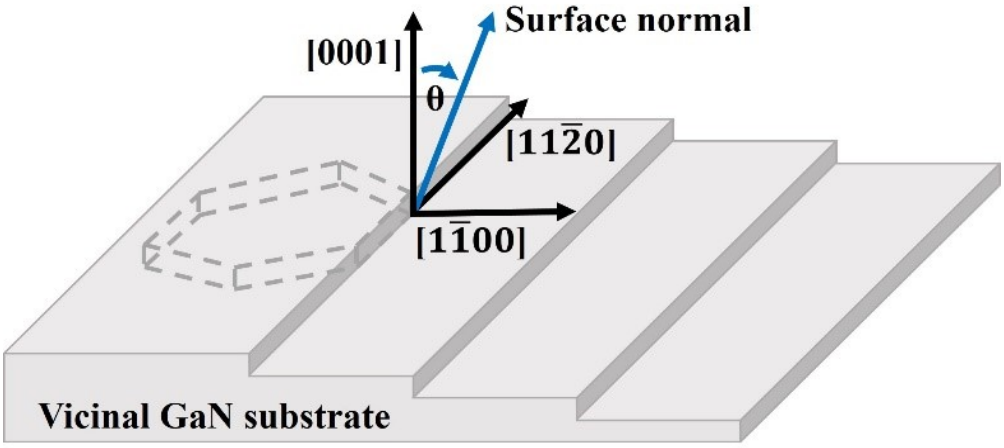

Fig. 4.1. Miscut angle θ and crystal directions in a vicinal GaN substrate.

A schematic layer arrangement of the samples used in this study is shown in Fig. 4.2. In all cases, the GaN substrates were first covered with a 2-μm-thick *u*-GaN layer, with

the purpose of decoupling the HVPE GaN substrate surface effects, which include sawing and mechanical and chemical polishing steps. A total of eleven epilayer structures were grown, labeled A to K.

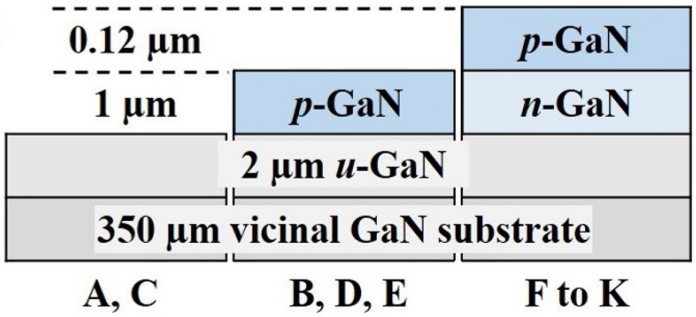

Fig. 4.2. Schematic diagram of the layer structures of *u*-GaN films (Samples A and C), GaN:Mg/*u*-GaN films (Samples B, D, E), and GaN:Mg/GaN:Si/*u*-GaN films (Samples F-K) on vicinal GaN substrates. The thickness of each layer is indicated.

A description of the first series (Samples A-E) is in Table 4.1. Samples A and C were the basic 2-µm-thick *u*-GaN layer grown on substrates with miscut angles of 0.3° (±0.15°) and 2° (±0.5°), respectively. Samples B, D and E were 1-µm-thick GaN:Mg grown on 2-µm-thick *u*-GaN layers on substrates with miscut angles of 0.3° (±0.15°), 2° (±0.5°), and 4° (±0.5°), respectively.

Table 4.1. Description of Samples A-E. The surface roughness was determined from AFM images over a 10x10 µm^2 area. The growth rates for *u*-GaN and GaN:Mg layers were 60 and 4 nm/min, respectively.

Sample ID	Structure	Miscut angle (°)	Roughness Rq (nm)
A	*u*-GaN	0.3	0.3
B	GaN:Mg/*u*-GaN	0.3	1.2
C	*u*-GaN	2	7.3
D	GaN:Mg/*u*-GaN	2	3.0
E	GaN:Mg/*u*-GaN	4	5.3

The second series, Samples F-K in Table 4.2, consists of GaN:Mg/GaN:Si/*u*-GaN layers grown on substrates with various miscut angles. The effect of a slower growth rate of the GaN:Si/*u*-GaN underlayers on the surface morphology of the GaN:Mg epilayers are evaluated. The only change of this set of samples was the growth rate of the underlayers, from 60 to 30 nm/min, while doubling their growth time in order to get the same film thickness. Thus, the Si-doped (GaN:Si) layers were grown with SiH_4 flow rates of 34 and 17 sccm, TMGa flow rates of 270 and 135 sccm, and growth times of 1000 and 2000 s (growth rates: 60 and 30 nm/min), respectively, and a NH_3 flow rate of 50000 sccm. Likewise, the *u*-GaN underlayers were grown with a TMGa flow rate of 270 and 135 sccm, a growth time of 2000 and 4000 s (growth rates: 60 and 30 nm/min), respectively, and a NH_3 flow rate of 50000 sccm.

Table 4.2. Growth parameters for GaN:Mg/GaN:Si/*u*-GaN layers (Samples F to K), grown on substrates with various miscut angles. The growth rate used for GaN:Mg layer was 4 nm/min. Two growth rates were used for the GaN:Si/*u*-GaN layers. The surface roughness was determined from AFM images.

Sample ID	TMGa flow rate (sccm)	Growth rate (nm/min)	Miscut angle (°)	Roughness Rq (nm)
F	135	30	0.3	0.17
G	270	60	0.3	0.20
H	135	30	2	3.2
I	270	60	2	5.1
J	135	30	4	5
K	270	60	4	13

The surface morphology of the *u*-GaN and GaN:Mg epilayers was studied using a Bruker AFM operated in tapping mode with a tip driven at frequencies above 1 kHz. The atomic arrangement at the surface was studied by TEM, from cross-section samples prepared by mechanical wedge polishing followed by Ar^+ ion milling at liquid N_2 temperatures with a 2 kV accelerating voltage, Images of the surface steps were obtained using a bright-field detector, in an aberration-corrected FEI Titan microscope operated at an electron beam accelerating voltage of 300 kV. A correlation with the microscopic optical characteristics was obtained using CL spectroscopic imaging, with an electron beam current of 100 pA in a JEOL 6300 scanning electron microscope equipped with an Oxford CL2 monochromator and with a photomultiplier tube. The electron beam acceleration voltage was 3 and 7 kV for plan-view and cross-sectional measurements, respectively.

4.3 Surface morphology of GaN epilayers

The threading dislocation density (TDD) in GaN thin films is significantly large compared to other semiconductor materials. For (0001) GaN grown by MOCVD on sapphire, the TDD is of the order of 10^{10} dislocations/cm^2.[14] Such dislocations are of the edge, screw, and mixed types, which are associated with crystal displacements (Burgers vectors, $\boldsymbol{b}$) with a magnitude of a, c, and $|a+c|$, respectively, where a = 0.319 nm and c= 0.518 nm are the lattice parameters of GaN.[82,83] The large displacement ($\boldsymbol{b} = \boldsymbol{c}$) of screw dislocations results in broken bonds due to inability to retain the atomic coordination, and leads to the existence of coreless dislocations (nanopipes).[83,84] The nanopipes have been reported to sometimes fill with GaN with inverted polarity (inversion domains).[85] Freestanding GaN substrates are produced by several techniques,[86] one of which is by

HVPE from seed crystals originally grown on substrates such as sapphire and GaAs.[68] During growth of thick HVPE GaN layers, the TDD is reduced down to about 10^6 cm^{-2} via dislocation recombination and mostly via coalescence of nanopipes into micropipes (where ***b*** = several ***c***). A useful review of the HVPE method is given in Refs. 69 and 86. Commercial GaN substrates with a low dislocation density are produced by growing GaN on a seed patterned with periodic stripes or dots, resulting in defects accumulating in specific regions and low dislocation region in between that can be used for device fabrication.[87,88] GaN substrate wafers are then cut from large crystals and the resulting surface damage is mechanically and chemically polished to a flat and smooth morphology. Subsequent epitaxial growth of *u*-GaN exhibits wavy features associated with the substrate misorientation and the threading defects. It has been observed pits on the epilayer surface corresponding to a density of ~10^6 cm^{-2}, which is similar to the nominal substrate TDD provided by the suppliers. The results presented here are representative of a number of commercial suppliers.

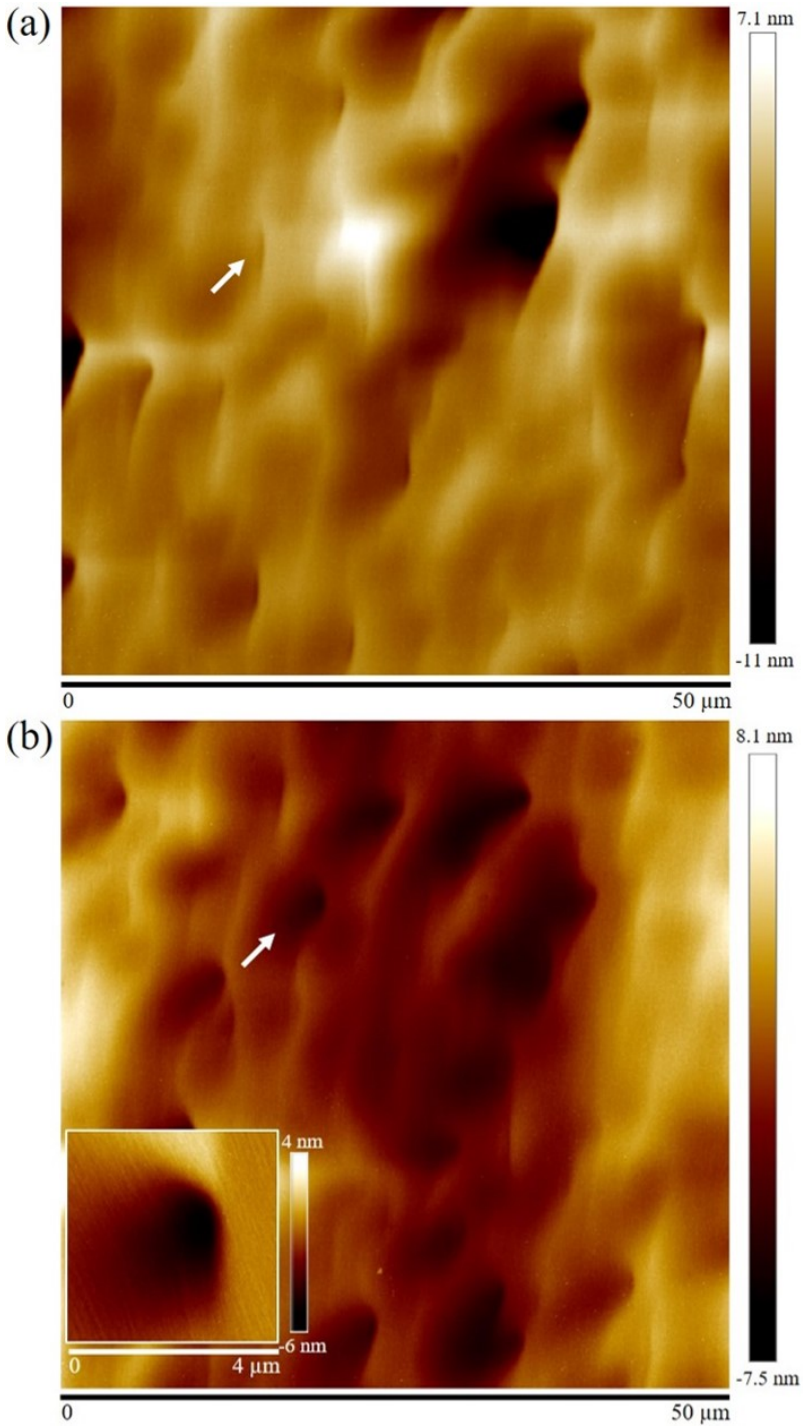

Fig. 4.3. AFM images of a *u*-GaN film (Sample A) grown on a 0.3° miscut GaN substrate. The presence of pinholes associated with threading screw dislocations significantly alter the surface morphology. (a) Region showing a lower density of micropipes, with dislocations pinning step flow (see arrow). (b) Region showing a high density of micropipes, with arrow indicating a micropipe with 2 µm in diameter in inset.

Figure 4.3 shows AFM images of the surface of a *u*-GaN layer grown on a 0.3° miscut GaN substrate. Fig. 4.3(a) shows the presence of pits, some of them barely visible at the image magnification and other pits with diameters of the order of microns. Single dislocation terminating at the surface prevents the lateral propagation of the atomic layers by pinning the step flow. The step pinning sites reflect the curved step front where multisteps are concentrated on one side and a terrace is present on the other side.[89] Other pits with diameters of the order of microns correspond to micropipes threading from the substrate. Fig. 4.3(b) shows a region with a high density of pinholes resulted from the collection of dislocations during growth.

Figure 4.4 is an AFM image of the surface of a GaN:Mg layer grown on a *u*-GaN layer on a 0.3° miscut substrate. A noticeable presence of surface steps indicates the tendency magnesium-doped layer to grow over the pinholes, as in the crater-like region indicated by the arrow. A higher magnification image of the micropipes indicated by the arrow is shown as the inset, where the step sequence nearly covers the micropipe.

The goal of this paper is to study the effect of substrate miscut on the surface morphology of epilayers. The relatively low dislocation density, about 10^6 cm^{-2} for our substrates vs. 10^{10} cm^{-2} for GaN/sapphire, means that the average separation between dislocations is 10 vs. 0.1 μm, respectively. Therefore, there are relatively flat regions where well-defined step-flow growth takes place parallel to the vicinal GaN substrates. Our AFM and TEM images shown in this paper were obtained from regions far from nanopipes.

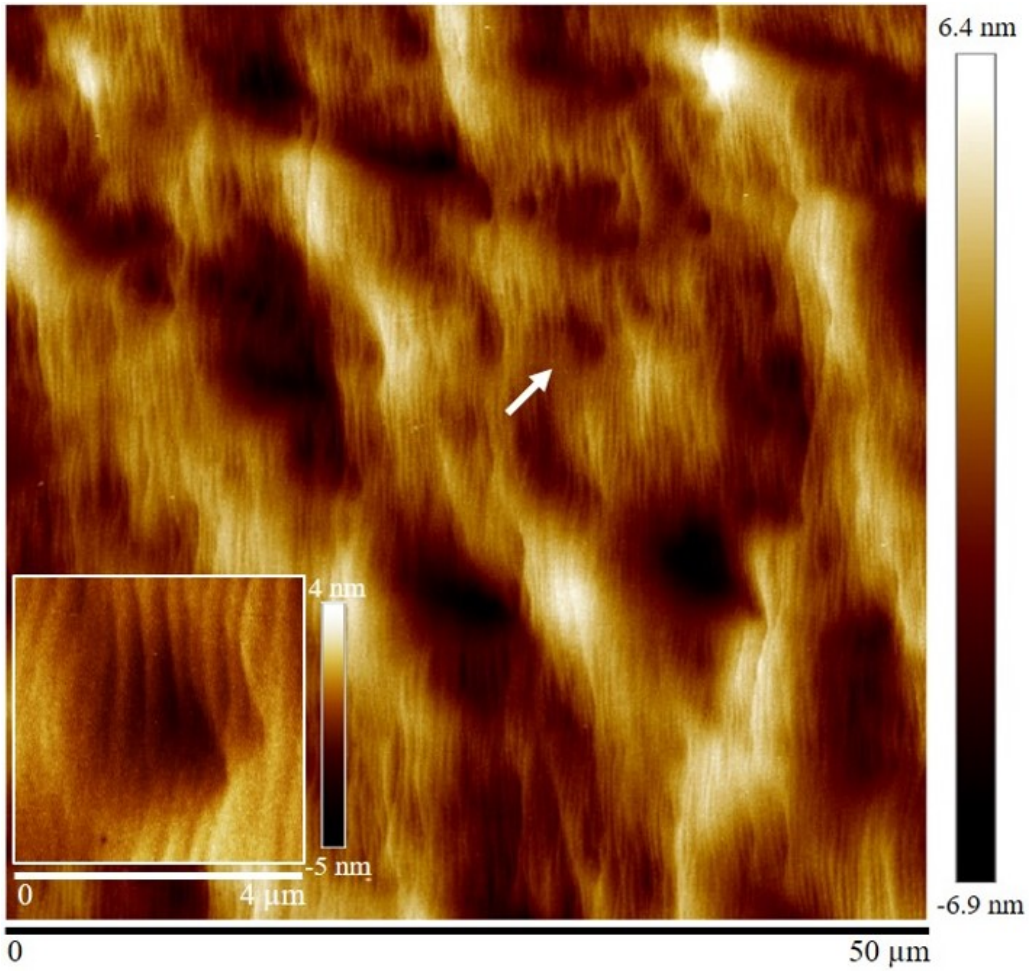

Fig. 4.4. AFM images of a GaN:Mg film (Sample B) grown on a 0.3° miscut GaN substrate showing the presence of pinholes (e.g. see the arrow) and the formation of steps, with partial coverage of the pinholes. A pinhole is magnified the inset.

The roughness of Samples A-E in Table I, determined from AFM images over an area of 10x10 μm^2, varies with the substrate miscut angle. Sample A with a *u*-GaN layer grown on a 0.3° miscut substrate, is rather smooth (R_q=0.3 nm), and follows the substrate specifications. For Sample B on a 2° miscut, the roughness increases (R_q=7.3 nm) and a hill-and-valley morphology is observed.

4.3.1 Mg-doping effects on vicinal-surface morphology

This session focuses on the effect of magnesium doping on the surface morphology of thin films grown on miscut substrates. The variation of surface roughness with substrate miscut for the *u*-GaN layers and the GaN:Mg layers is compared. The roughness of Samples A-E in Table 4.1, determined from AFM images over an area of 10x10 μm^2, varies with the substrate miscut angle. Sample A with a *u*-GaN layer grown on a 0.3° miscut substrate, is rather smooth (R_q=0.3 nm), and follows the substrate specifications. For Sample C on a 2° miscut, the roughness increases (R_q=7.3 nm).

The addition of a 1-μm-thick GaN:Mg layer in the 0.3° miscut case (Sample B) results in an increase in surface roughness from 0.3 to 1.2 nm (Table 4.1), and the appearance of straight surface steps (Figs. 4.2 and 4.3). In the 2° miscut case (Samples C and D), the surface roughness actually decreases from 7.3 to 3.0 nm (Table 4.1).

AFM images of all magnesium-doped films (Samples B, D, E in Fig. 4.5) show well-defined parallel steps with periodicity that varies with miscut angle. In low magnification images, surface depressions in the vicinity of micropipes disturb the step flow and affect the step periodicity. In high magnification images taken away from the micropipes, a uniform step distribution can be observed. In the 0.3° miscut case (Sample B in Fig. 4.5(a)), steps are observed with a period of 200 nm and a step height of ~ 1 nm. An increase in miscut angle to 2° (Sample D in Fig. 4.5(b)) results in the presence of supersteps with a period of 4.5 μm, coexisting with regions of parallel steps with a period of 150 nm and a step height of ~1.5 nm (oriented to the basal plane with an average tilt angle of 0.6°). At an even higher miscut angle of 4° (Sample E in Fig. 4.5(c)), single steps are observed with periods of less than 25 nm, and periodic supersteps with an average separation of ~2 μm.

The separation of single steps is close to our AFM resolution and the steps are not easy to visualize.

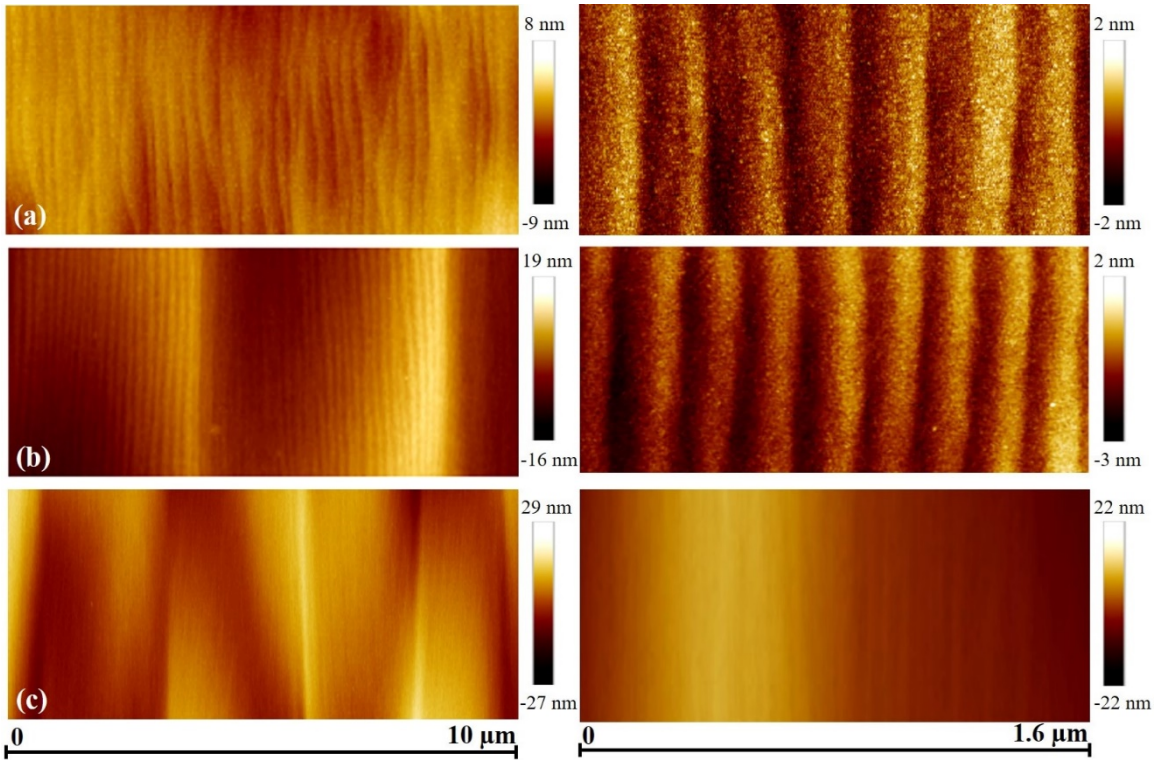

Fig. 4.5. AFM images of GaN:Mg films at low (left) and higher (right) magnifications, showing periodic arrays of atomic surface steps. (a) A step period of ~ 200 nm is observed in Sample B. (b) In Sample D, steps with ~ 150 nm period and step height of 1.5 nm, and supersteps with ~ 4.5 µm period are observed. (c) Sample E is dominated by supersteps with an average separation of ~ 2 µm.

The relationship between surface misorientation and step separation for possible step-heights is shown in Fig. 4.6. As expected, the step separation decreases with surface tilt angle and increases with step height. Monolayer and bilayer steps have been reported as stable units on the (0001) wurtzite GaN surface.[90,91] Monolayer-height steps reportedly constitute the equilibrium morphology for GaN surfaces grown by MOCVD at above 850 °C.[90] On the other hand, bilayer steps were observed in films grown by molecular beam epitaxy at 650 °C.[91] Cross-sectional TEM imaging has been used to identify the atomic

arrangement at the surface of GaN:Mg films. Straight step edges along the *a*-axis are observed, with step heights of *c*/2 (0.26 nm) or *c* (0.52 nm), depending on the surface inclination.

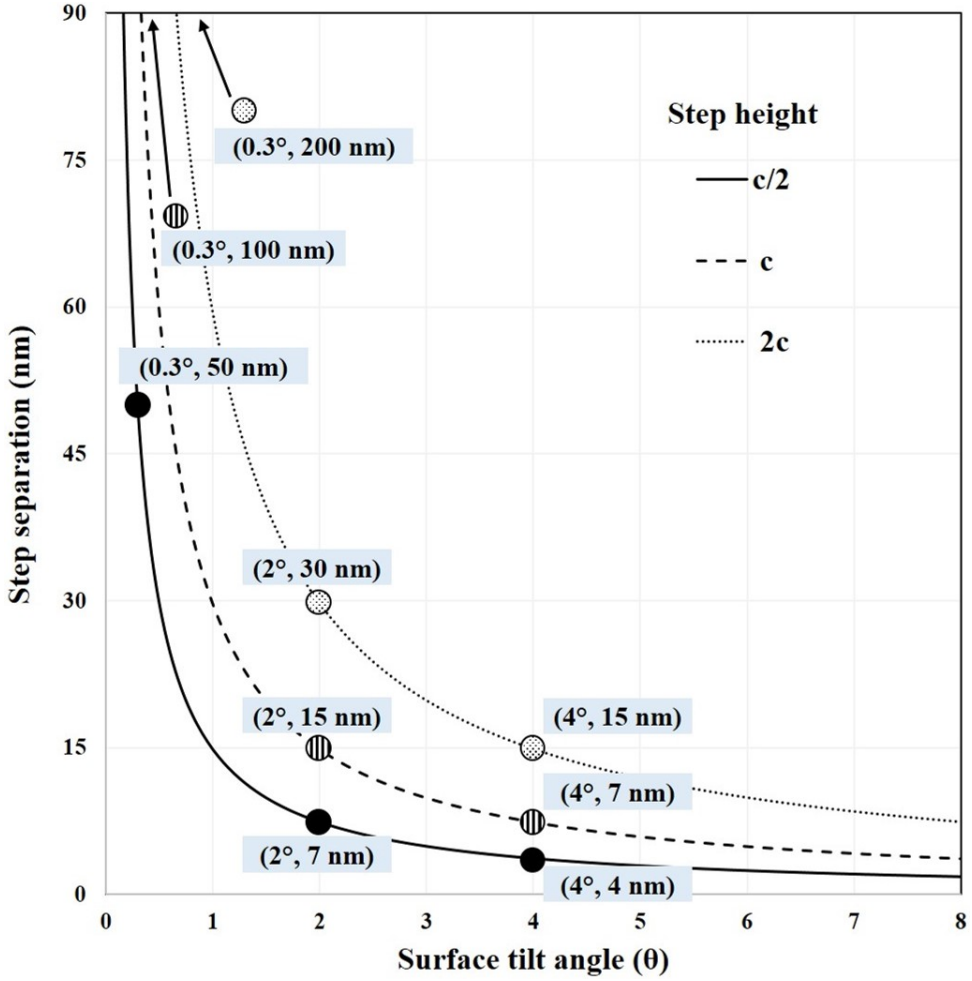

Fig. 4.6. Step separation vs. surface tilt angle for various step heights. Specific values are given for the substrate miscut angles used in this work.

For GaN:Mg grown on a 0.3° miscut substrate (Sample B), two different regions are observed in Fig. 4.7. The first is an atomic-flat region along a basal plane, without steps, and the second one has a tilt of ~ 1.1° with respect to the basal plane. The tilted region contains successive steps of height *c*/2 and an average step separation of 14 nm. The AFM

images in Fig. 4.5(a) give widths of 145 nm and 55 nm for the first and second regions, together making up for the average 0.3° miscut.

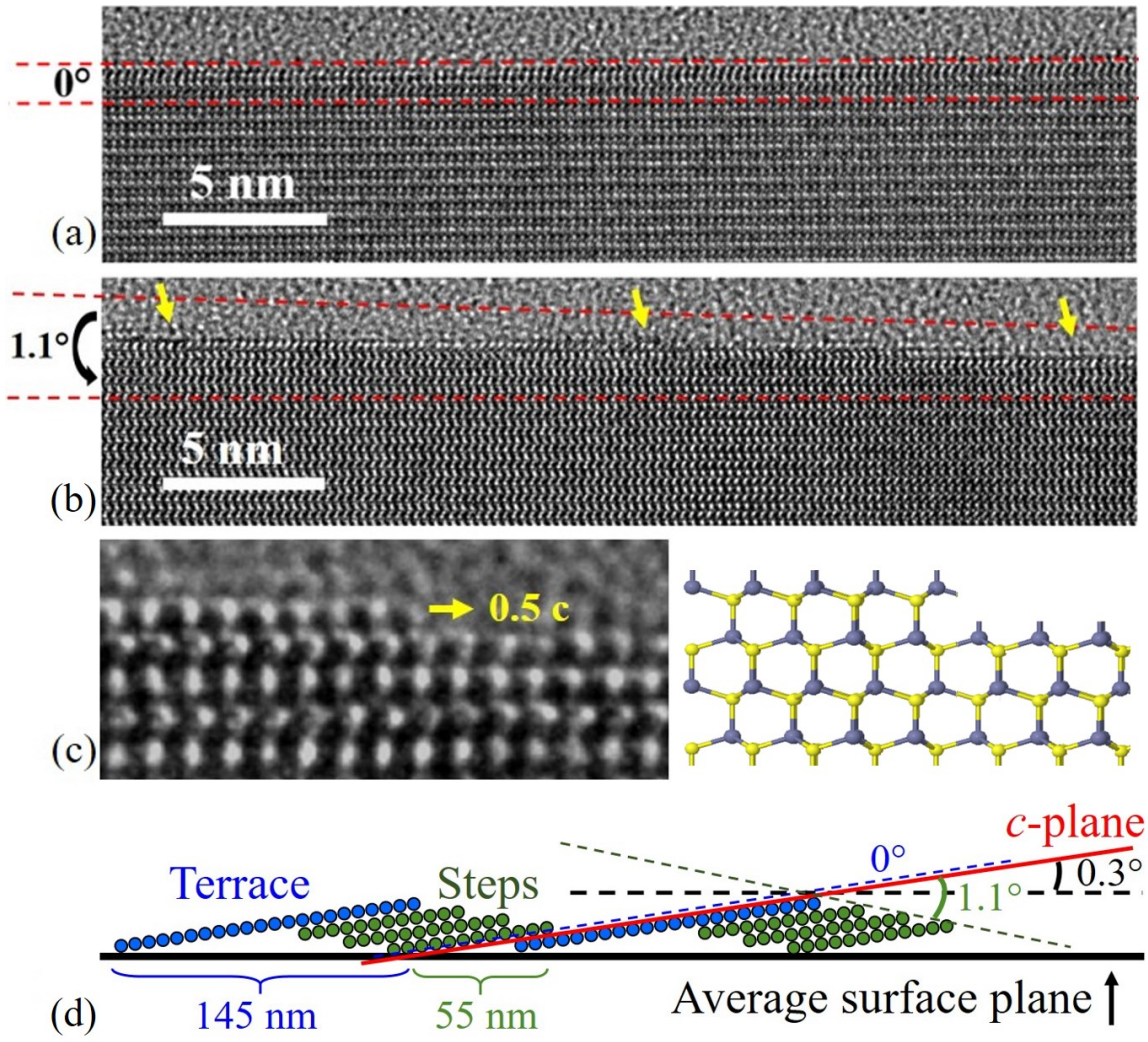

Fig. 4.7. TEM images of a GaN:Mg film grown on a 0.3° miscut GaN substrate (Sample B). (a) A surface region parallel to the *c*-plane. (b) A surface region with 1.1° tilt from the *c*-plane. (c) High magnification image of a step with height *c*/2, and a schematic diagram of the corresponding atomic arrangement. (d) Schematic diagram of the overall morphology of steps in Sample B. (For visualization purposes the angles are oversized and not to scale).

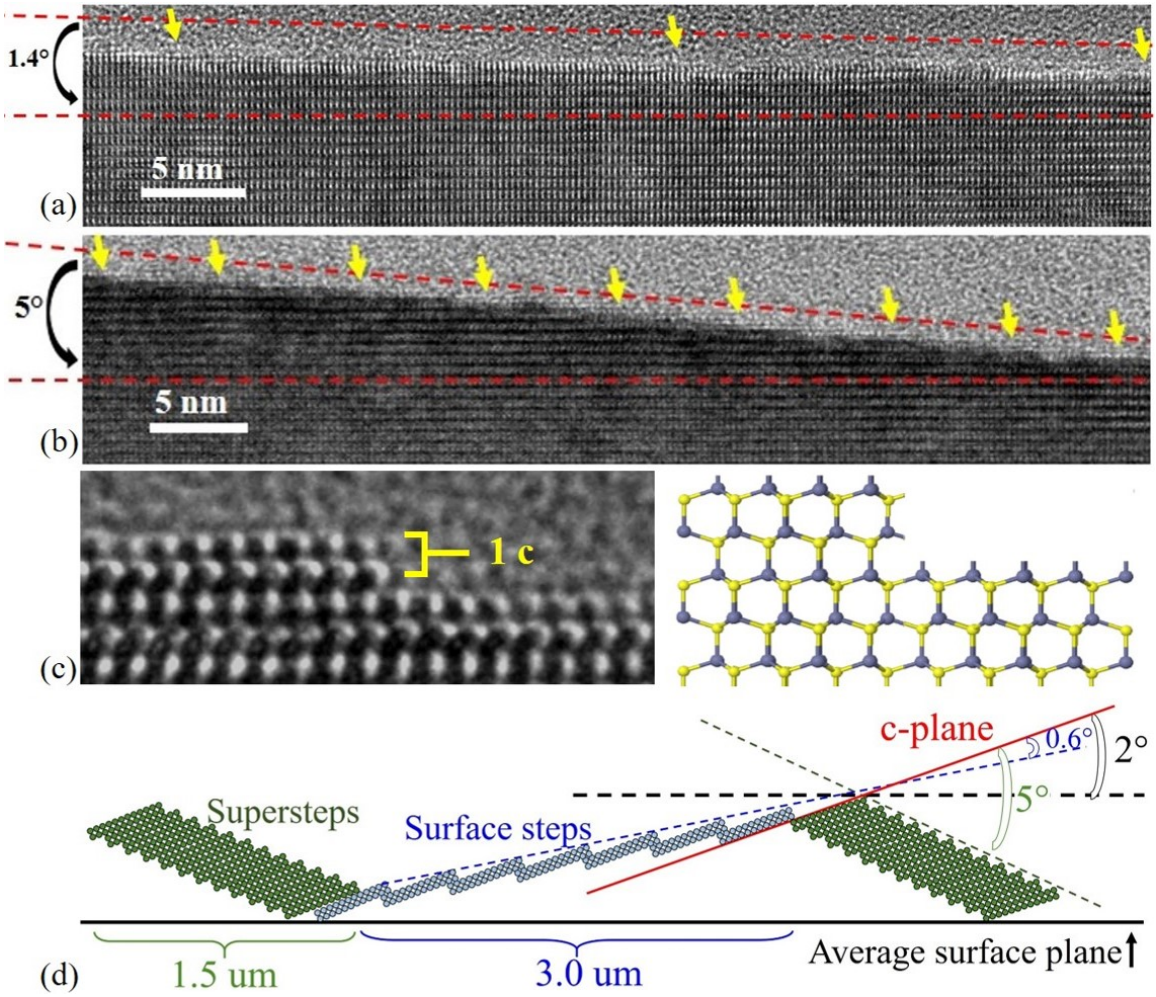

Fig. 4.8. TEM images of a GaN:Mg film grown on a 2° miscut GaN substrate (Sample D). (a) A surface region with 1.4° tilt from the c-plane. (b) A surface region with 5° tilt from the *c*-plane. (c) High magnification image of a step with height *c*, and a schematic diagram of the corresponding atomic arrangement. (d) Schematic diagram of the overall morphology of steps in Sample D. (For visualization purposes the angles are oversized and not to scale). A tendency towards formation of basal planes is corrected by the presence of supersteps.

For the 2° miscut case (Sample D), two regions with different tilt angles are shown in Fig. 4.8. The first region has a tilt of ~ 1.4° with respect to the basal plane, and average step separation of ~ 21 nm in Fig. 4.8(a), coupling with an atomic-flat region along a basal plane (not shown) to make an average 0.6° tilt, as observed by AFM in Fig. 4.5(b). The second region has a tilt of ~ 5° with respect to the basal plane, corresponding to the edge

of a superstep, consisting of several steps with a height of *c*. The AFM images in Fig. 4.5(b) give widths of 3.0 μm and 1.5 μm for the first and second regions, respectively, together making up for the average 2° miscut.

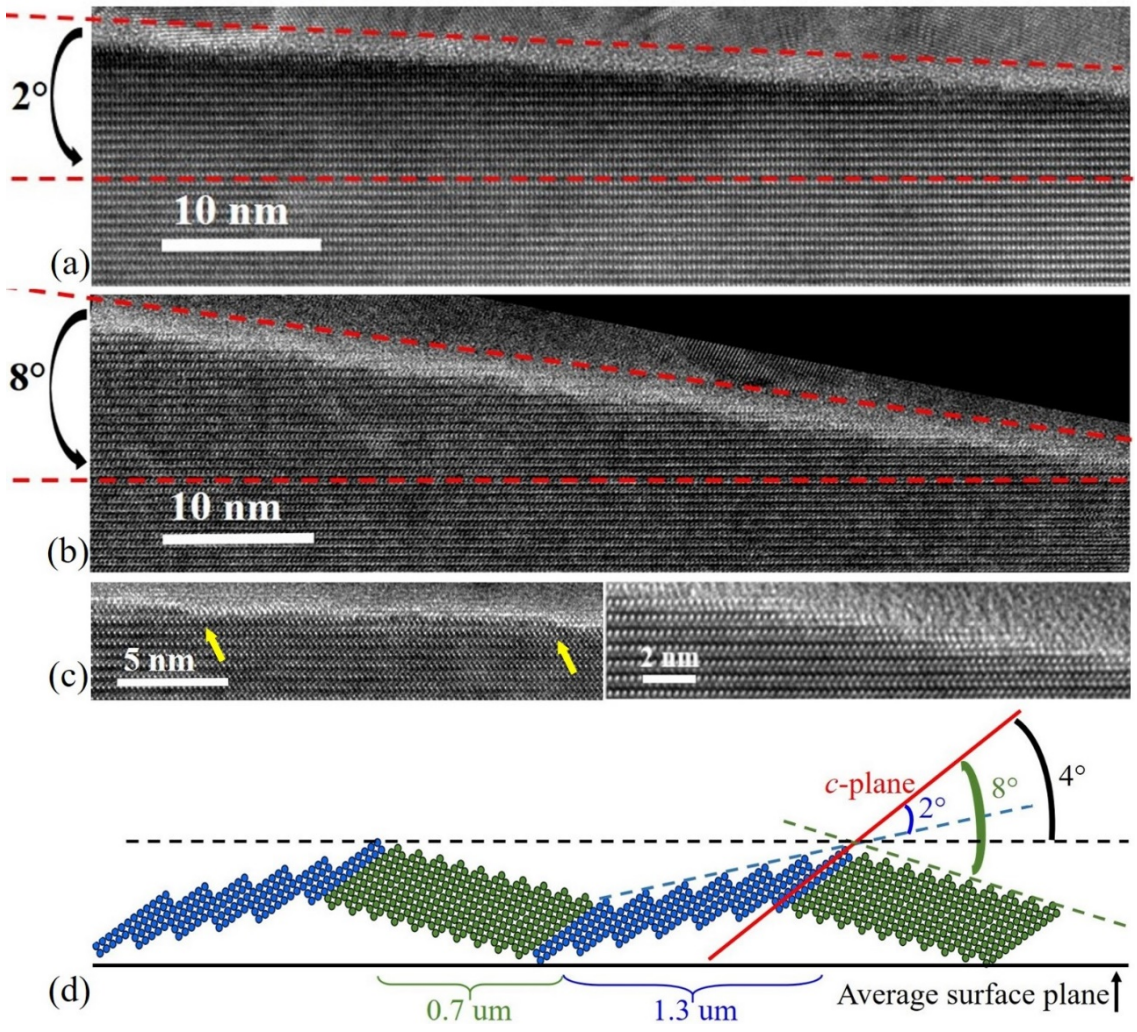

Fig. 4.9. TEM images of a GaN:Mg film grown on a 4° miscut GaN substrate (Sample E). (a) A surface region with 2° tilt from the *c*-plane. (b) A surface region with 8° tilt from the *c*-plane. (c-left) High magnification images of the 2° case with step separation of 15 nm, and (c-right) the 8° case with step separation of 4 nm. (d) Schematic diagram of the overall morphology of steps in Sample E. (For visualization purposes the angles are oversized and not to scale). A tendency towards formation of basal planes is corrected by the presence of supersteps.

For the 4° miscut case (Sample E), two different regions are observed in Fig. 4.9. The first has a tilt of ~ 2° with respect to the basal plane, and the second one has a tilt of ~ 8°.The two high-magnification TEM images in Fig. 4.9(c) show the step configuration of these two regions, with a step height of *c* and a separation of 15 and 4 nm, corresponding to the 2° and 8° cases, respectively. The AFM images in Fig. 4.5(c) give widths of 1.3 μm and 0.7 μm for the first and second regions, together making up for the average 4° miscut.

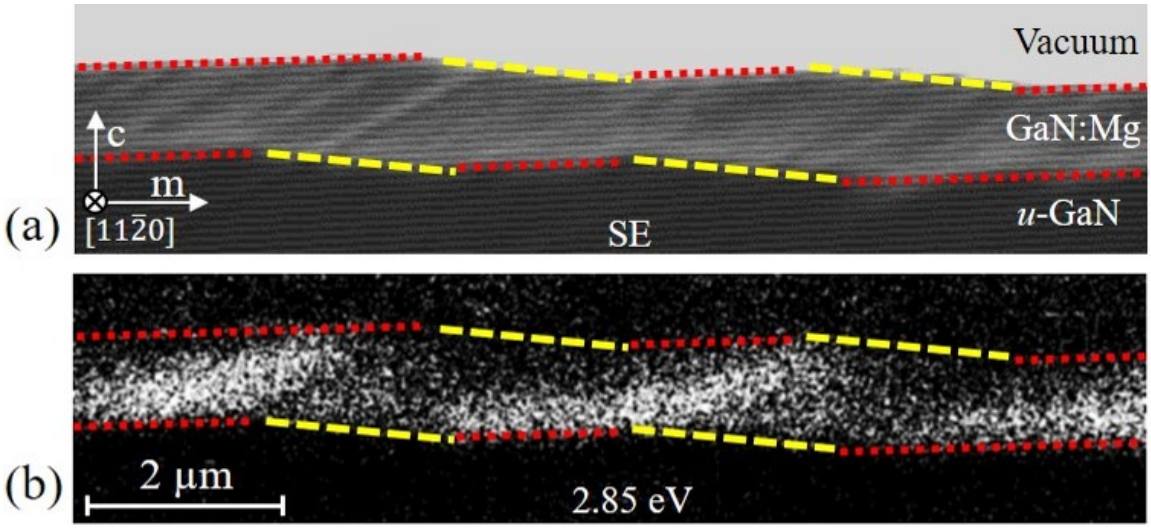

Fig. 4.10. Surface morphology and luminescence for the GaN:Mg film grown on a 4° vicinal GaN substrate (Sample E). (a) Cross-sectional SE image showing regions with surface orientation of ~2° (dotted red line) and ~8° (dashed yellow line). (b) Monochromatic CL image at 2.85 eV shows nonuniformity in luminescence across the film. (Courtesy of Hanxiao Liu)

Secondary-electron (SE) and monochromatic CL images in cross-section of Sample E are shown in Fig. 4.10. The interface of the GaN:Mg and *u*-GaN layers is marked by dashed lines, one with a ~2° tilt from the basal plane (red dashed line) followed by a region with a ~8° tilt (yellow dashed line), which alternate to produce the overall 4° surface tilt. Bright bands with strong 2.85 eV luminescence intensity are observed originating from 2° tilted

regions (red dash lines). Darker bands are observed originating from the 8° tilted regions (yellow dashed line).

4.3.2 Effect of growth rates on surface morphology of GaN:Mg

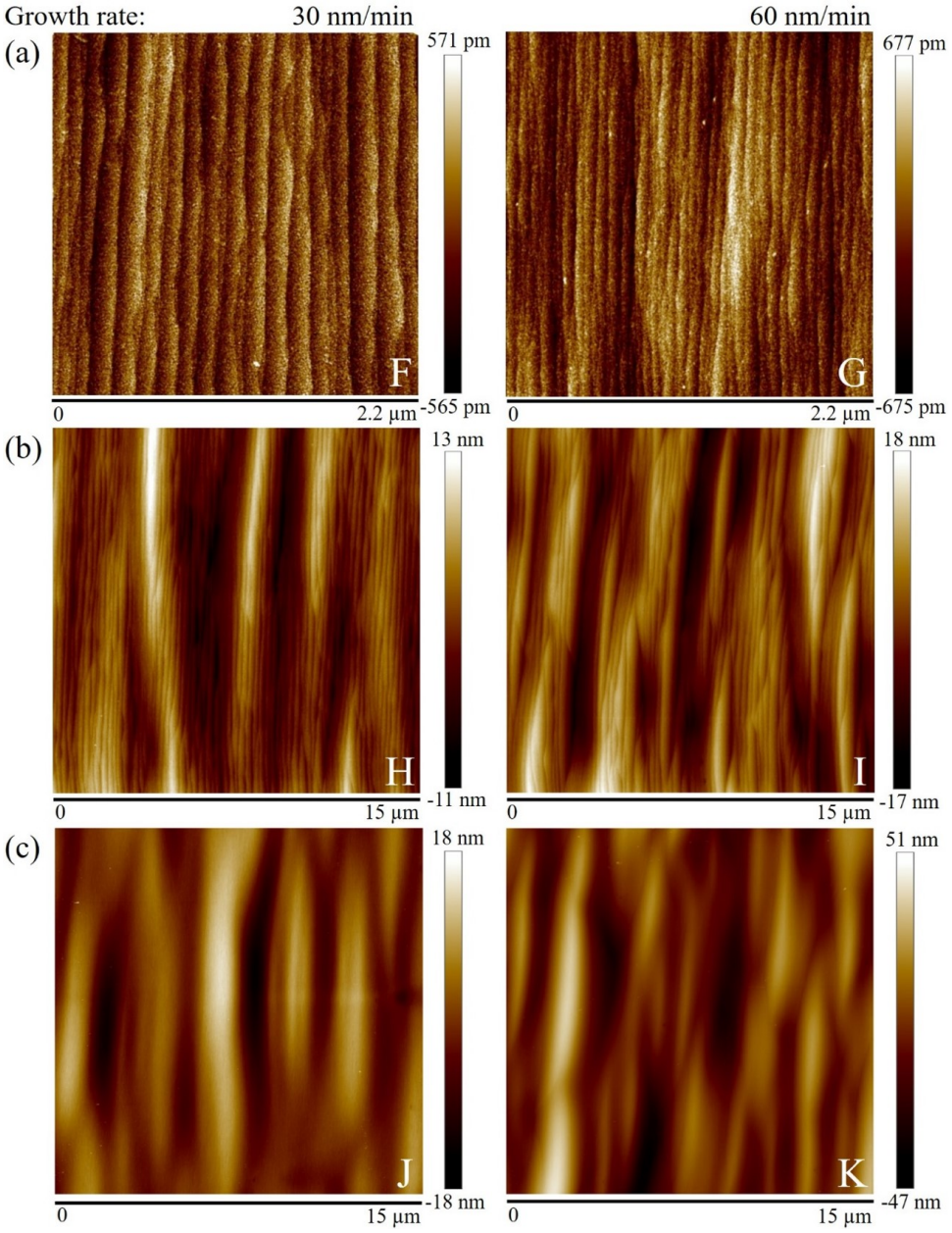

Fig. 4.11. GaN:Mg films grown at 4 nm/min, on underlaying GaN:Si/*u*-GaN with growth rates of 30 nm/min (left column) and 60 nm/min (right column). It is observed that step bunching becomes more prominent with growth rates for (a) 0.3°, (b) 2°, and (c) 4° miscut substrates.

This session focuses on the effect of growth rates on the surface morphology of GaN:Mg thin films grown on vicinal GaN surfaces. It is found that slower growth rates result in smother surfaces. AFM images of Samples F-K are shown in Fig. 4.11, and the respective surface roughness values are given in Table 4.2. In summary, the roughness and the density of step bunches increase with miscut angles. The samples grown at a slow growth rate exhibit smoother surfaces, compared to a fast growth rate. Plan-view CL spectra of these samples are shown in Fig. 4.12. The CL emission peaks at 3.4 and 2.85 eV correspond to near-band-edge transitions and deep-donor-to-acceptor transitions, respectively.[92,93] The intensity of the 2.85 eV peak is stronger in Samples F, G, H, and I, and weaker in Samples J and K. In particular, a significant decrease in intensity of the 2.85 eV peak is observed in Sample K.

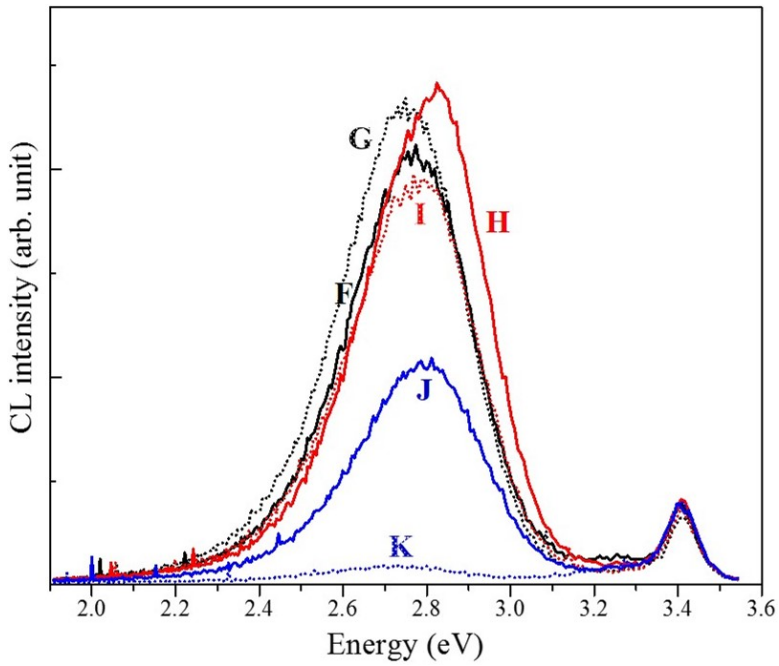

Fig. 4.12. Plan-view CL spectra of Samples F to K. The intensities of the 2.85 eV peaks from Samples F to I are similar; while Samples J and K exhibit weaker intensities. The CL spectra were acquired at 298 K, with an acceleration voltage of 3 kV, an electron current of 100 pA, scan magnification of 2000 times, using a slit of 2 µm. (Courtesy of Hanxiao Liu)

4.4 Discussion

The presence of micropipes significantly alter the surface morphology of thin GaN films, as observed in Figs. 4.3 and 4.4. Frank predicted that dislocations with Burgers vectors exceeding a critical value should have a hollow tube at the core.[94] Elastic strain considerations for a cylindrical core gives an equilibrium core radius of the hollow core proportional to b^2,

$$r_{eq} = \frac{\mu b^2}{8\pi^2\gamma} \qquad (1)$$

where μ is the shear modulus, b the Burgers vector, and γ is the surface energy. For $b = c$ in GaN, coreless dislocations have a diameter between 5 and 25 nm.[84] As mentioned in Section II, screw dislocations tend to coalesce during growth of thick layer, with $\boldsymbol{b}$ being a multiple of $\boldsymbol{c}$, leading to the different pinhole diameters observed on our GaN surfaces. The surface depression around the pinholes can be explained by considering the force balance between surface tension and the dislocation line tension, as in Fig. 4.13(a).[94,95] A SEM secondary electron image of a pinhole with core radius of ~ 0.25 μm, present on a GaN surface is shown in Fig. 4.13(b). Considering the diameter of a screw dislocation with $b = c$ ranges from 5 to 25 nm, the observed pinhole with this size may correspond to a screw dislocation with $b = nc$, where n=5 to 20. It is worth mentioning that hexagonal features observed inside the hollow core, are associated with screw dislocations with screw components c, coming out from the crystal to create free surfaces inside the core. The growth spirals follow the Burgers circuit to generate the hexagonal columns, see arrows in Fig. 4.13(b).

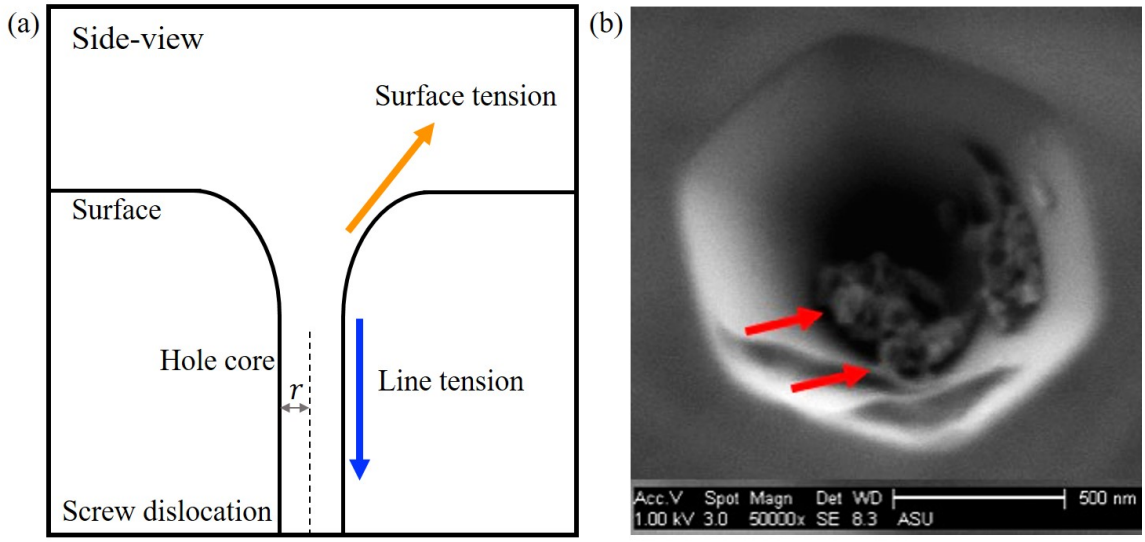

Fig. 4.13. Schematic diagram of the force balance and a SEM Image of a Pin Hole. (a) The force balance at the termination of a threading coreless dislocation. (b) A top-view secondary-electron image of a pinhole (nanopipe) present on a GaN surface, the arrows indicate hexagonal columns.

The growth mechanisms of thin films involve nucleation and surface diffusion processes, and have been classified into three growth modes: one-dimensional step-flow, two-dimensional layer-by-layer, and three-dimensional island growth.[96-98] At low supersaturation, the presence of periodic steps on a vicinal surface allows *one-dimensional* lateral growth via step-flow growth. Higher supersaturation results on nucleation on the terraces between steps, and contributes with a *layer-by-layer* growth. At even higher supersaturations, higher layer nucleation rates result in three-dimensional island growth.[98,99]

The density of steps depends on the surface tilt with respect to the basal plane (miscut angle), as shown in Fig. 4.6. The termination of a layer at a step results in a distortion in the bonding configuration and an elastic strain field, leading to inter step interaction and step redistribution that results in regions with different surface orientations. The

rearrangement of the surface into periodic regions with different step densities produces a *hill-and-valley* structure that has a lower energy than the average flat surface.[100] Such rearrangement has been termed *faceting*.[101] It was found that this type of rearrangement associated with vicinal surfaces (Figs. 4.5 and 4.7-9). The phenomenon of periodic facets has also been attributed to a dipole-dipole interaction between steps.[101]

Step-flow growth happens when adatoms diffusing on the surface are incorporated into steps.[96] The direction with which an atom approaches a step determines the probability of capture. A diffusing atom approaching the top of a step senses a decrease in coordination (leading to reflection), while approaching the bottom of a step senses an increase in coordination (leading to capture).[78] This process has been modeled using an electrostatic potential known as the *Ehrlich-Schwoebel* barrier (ESB).[79] In this model, step-flow growth leads to smooth surfaces associated with the advancement of the parallel step array. Roughening can happen under supersaturation conditions, where an increase in the local adatom concentration near down-step edges can lead to two-dimensional nucleation.

For the undoped case (Samples A and C), it has been observed in Table 4.1 a significant increase in the surface roughness from 0.3 to 7.3 nm with an increase in miscut angle. This is due to the occurrence of growth on macrosteps at higher tilted surfaces, suggesting the existence of a critical transition angle between 0.3° and 2°. The surface roughening can be explained by the rate of advancement of steps.[102] Instead of monolayer steps advance, multiple steps can come together due to local fluctuation of atomic flux, impurity atoms, and lattice imperfection. The advance rate of multisteps will be lower than that of the monolayer steps, since they need a greater flux of atoms in order to advance at

the same rate as a monolayer step. For surfaces with hexagonal symmetry and vicinal to the basal plane, the velocity of advancement of steps has been derived to be: [103]

$$v = \frac{4J\lambda_s h_0}{n_0 h} \qquad (2)$$

where J is the flux of reactants arriving at the surface, λ_s is the surface diffusion length of adatoms, h_0 is the single basal plane spacing (0.26 nm for (0002) 2H-GaN and for (0006) 6H-SiC), n_0 is the density of adatom sites on the surface, and h is the step height. It indicates that at given reactants flux and growth conditions, the step velocity is inversely proportional to the step height. Thus, in the case of closer step separation as for 2° miscut of Sample B, the preceding equation indicates that if two steps coalesce, their velocity will become half of that of a single step, and other steps will be able to catch up, leading to the formation of macrosteps.

4.4.1 Mg-doping effects on vicinal-surface morphology

Surface steps on *u*-GaN films were not able to be visualized using AFM, possibly because steps associated with the miscut angle are not straight and meander (zig-zag) on the surface. The situation is quite different for Mg-doped GaN films, where the formation of well-defined steps are observed (as in Fig. 4.5). In the case of a 0.3° miscut, steps meander on the surface of undoped GaN (such as in Sample A, Fig. 4.3) which is indicative of a lower excess free energy per unit length (line tension) of the step, as in Fig. 4.14(a).

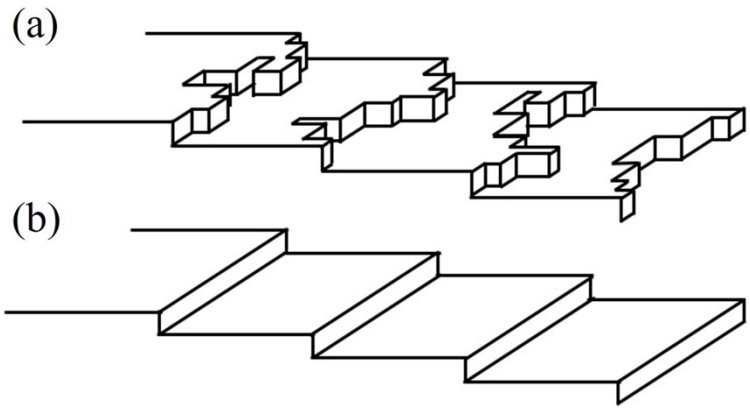

Fig. 4.14. The transition in surface morphology of vicinal GaN films with Mg doping. (a) Meandering steps on the undoped GaN surface. (b) Straight steps on the GaN:Mg surface.

The presence of Mg increases the line tension of the steps,[104] making them straight, and leading to the formation of well-defined periodic step arrays (such as in Figs. 4.3 and 4.14(b)), as well as the formation of clusters of steps, also known as supersteps or macrosteps (Fig. 4.5). The origin of the clusters has been attributed to the elastic strain of steps and to dipole interactions between steps.[105] The differently oriented surface regions associated with macrosteps are also referred as facets.

The effect of Mg doping becomes more prominent for the 2° miscut case. Comparing *u*-GaN and GaN:Mg films (Samples C and D in Table 4.1), a significant decrease in surface roughness from 7.3 to 3.0 nm were observed. The phenomenon of smoothing out the roughness has also been attributed to an increase in lateral growth by Mg doping.[106] In the case of a 4° miscut with a higher step density, step-step interaction becomes more important, resulting in well-defined facets with two different orientations (as in Fig. 4.9). Nonuniform CL luminescence at 2.85 eV is associated with the difference in acceptor incorporation efficiency for low- and high-tilted facets (as in Fig. 4.10).[107] More details on the influence of surface inclination on the optical properties are given in Ref. 107.

In summary, it has been observed that the surface of GaN:Mg epilayers evolve into regions with different step densities and hence different inclinations, but altogether averaging to the miscut orientation. Similar observations were reported for vicinal (111) Si surfaces, where the original surface decouples into regions with different orientations and lower surface free energies.[105] The difference between monolayer steps (like Sample B in Fig. 4.7) and bilayer steps (like Samples D and E in Figs. 4.8 and 4.9) has been attributed to the difference in surface free energy.[108] Similar effects have also been reported for (100) Si vicinal surfaces, where experiment and theory show a transition between single-layer and double-layer stepped surfaces that occurs in the vicinity of 2° tilt.[108]

4.4.2 Effect of growth rates on Mg-doped vicinal-surface morphology

Growth rates can affect the surface morphology of GaN films as seen in Fig. 4.11. It has been observed that a slow growth rate results in an increase of the step-flow growth and a lower degree of step bunching, resulting in a smoother surface. As mentioned earlier, when the supersaturation α_{max} on terraces is large enough to exceed a critical value α_{crit}, the step-flow growth turns into a two-dimensional nucleation mode that roughens the surface. The supersaturation α_{max} can be expressed as:[109]

$$\alpha_{max} = 1 + \frac{\lambda_0 n_0 R}{2\lambda_s h} \frac{\tau_s}{n_{s0}} tanh\left(\frac{\lambda_0}{4\lambda_s}\right) \qquad (3)$$

where λ_0 is the mean inter-step distance, R is the growth rate, τ_s is the mean residence time of adatoms, and n_{s0} is the adatom concentration at equilibrium; λ_s, n_0, and h are as defined for the Eq. (2). The growth rate R is associated with the precursor flux rates, which in our case concerns only the TMGa flux. The other parameters are inherent of the material

at a given temperature. Therefore, reducing the precursor flux rates leads to a smaller supersaturation α_{max}, which makes the step-flow growth dominant, resulting in a smoother morphology.

Another factor affecting the surface morphology is the parasitic reactions in the gas phase of MOCVD growth.[110] It has been known that the parasitic reaction between groups III and V precursors in the gas phase results in small clusters of atoms, that disturbs the step-flow growth and degrade the surface morphology. A slow growth rate with lower TMGa flow rate can suppress the parasitic reaction, with an improvement in morphology.

From Figs. 4.11 and 4.12, a correlation between the morphology of GaN:Mg films and the intensity of the 2.85 eV emission can be established. It has previously been suggested that Mg atoms incorporation as clusters at the surface steps may lead to reductions in acceptor concentration and in the corresponding 2.85 eV emission intensity.[107] Step evolution should affect Mg incorporation, and as the surface misorientation reaches a critical angle θ_{crit}, a significant reduction should occur in the acceptor density, leading to very weak 2.85 eV emission in that region. Fast growth rates lead to the formation of facets with higher tilted surfaces, that are close to or exceed the critical angle, resulting in a lower 2.85 eV emission intensity and a strong reduction of the acceptor density.

Our studies are based on AFM and TEM observations of surfaces which had been extracted from the reactor. The free energy of steps should make them susceptible to chemical reactions in air, and our observations may not reflect the exact nature of steps during growth.

4.5 Conclusion

It has been observed that the surface morphology of GaN:Mg epilayers are significantly affected by the miscut angle of the GaN substrates. Mg doping increases the line tension of steps, resulting in the formation of well-defined steps with a tendency to cover micropipes propagating from the substrate. Atomic-resolution imaging shows the transition of step height from monolayer steps to bilayer steps with increasing vicinal angle. It is found that facets with various step densities coexist, while the average orientation of vicinal surfaces is preserved. The titled facets can be correlated to the nonuniform Mg incorporation in GaN epilayers grown on miscut substrates. It has also been showed that a slow growth rate can suppress step bunching, leading to smoother surfaces and higher 2.85 eV emissions.

ACKNOWLEDGMENTS

The materials were grown by Dr. Zhihao Wu and his team at HC SemiTek Corporation, China. We acknowledge the use of facilities within the Eyring Materials Center at Arizona State University.

CHAPTER 5

INDUCTIVELY COUPLED PLASMA-INDUCED DAMAGE STUDY FOR GaN EPILAYERS

5.1 Introduction

Gallium nitride with superior fundamental properties, such as high bandgap energy, low intrinsic carrier concentrations, high critical breakdown electric fields, and high thermal conductivity, shows promising in high-power electronic applications.[66] The fabrication of GaN-based devices, dry etching techniques are commonly used to make device patterning, due to the high bond energy and inherent chemical stability of GaN.[111] Among typical dry etching techniques, inductively coupled plasma (ICP) etching yields high density of plasma and reduced ion energy, compared to reactive ion etching (RIE), attempting to minimize the damage from the high energy ion bombardment.[111]

Accelerating ions from the plasma to the sample surface in etching processes affects several aspects, including surface morphology, and the optical and electrical properties. It is essential to optimize the plasma or ions conditions in order to produce low surface damage and to optimize the device performance. In this work, the surface morphology and optical properties of GaN films, and leakage current of devices in the reverse bias region were investigated, for the purpose of understanding the damage induced by ICP etching. The nature of surface morphology was studied using atomic force microscopy (AFM) and the spatially-resolved optical characteristics was studied by cathodoluminescence (CL). A correlation has been established between etched surface morphology, the nanoscale optical, and electrical properties.

5.2 Experimental Details

A series of GaN epitaxial layers were grown by metal-organic chemical vapor depositions (MOCVD) on free standing *c*-plane GaN substrates, with hydrogen as the carrier gas, at a growth temperature of 1050 °C. The Ga and N sources were trimethylgallium (TMGa) and ammonia (NH3), respectively.

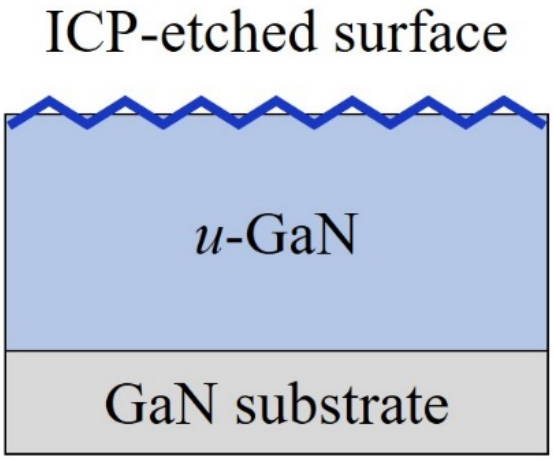

Fig. 5.1. Schematic structure of the series of samples: *u*-GaN epilayers grown on free standing GaN substrates (Samples A-F). Different ICP etching processes were applied to the *u*-GaN surfaces.

A total of six epilayer structures were grown, labeled A to F. The GaN substrates were first covered with a 2.5 μm thick unintentionally-doped GaN (*u*-GaN) epilayers, followed by different chlorine-based ICP etching processes. The schematic structure and etching parameters of samples are shown in Fig. 5.1 and Table 5.1, respectively. The etching processes involve varied ICP and RF powers, with Cl_2 and BCl_3 flow rates of 30 and 8 sccm, respectively, and a pressure of 5 mTorr.

Table 5.1. Description of ICP etching parameters of Samples A-F. The RF and ICP powers are varied, but the Cl_2 and BCl_2 flow rates are kept constant. Sample A without an etching process serves as a reference.

Sample ID	RF (W)	DC bias (V)	ICP (W)	Cl_2 (sccm)	BCl_2 (sccm)
A	-	-	-	-	-
B	5	39	100	30	8
C	5	29	200	30	8
D	5	21	400	30	8
E	35	95	400	30	8
F	70	159	400	30	8

The surface morphology of the *u*-GaN epilayers was studied using a Bruker AFM operated in ScanAsyst peak force tapping mode with a tip driven at frequencies above 1 kHz. The optical properties were studied CL spectroscopy. The CL system consists of a JEOL 6300 scanning electron microscope connected to an Oxford CL2 monochromator and a photomultiplier tube. The electron beam current used in the CL studies was 100 pA, with an acceleration voltage ranged between 2 to 10 kV for plain-view measurements. A Keithley 2410 sourcemeter was used for current-voltage (I-V) measurements.

5.3 Results and Discussion

5.3.1 Surface morphology of etched GaN films

In Fig. 5.2, AFM images show the surface morphology of Samples A-F, varies with the etching parameters (Table I). Periodic surface steps with a height of ~ 0.25 nm (c/2) are observed on non-etched surface of Sample A, corresponding to a 0.3° miscut, as the

one of substrates. The Samples B-F with etching processes show rougher surfaces, comparing to the non-etched surface (Sample A). In the case of a fixed RF power at 5 W, the surface of Sample B shows roughest with a highest DC bias. The uniform contrast in AFM images of Samples C and D etched by ions with a higher density but a lower energy, indicates the surfaces are relatively smooth, and the roughness is close to the one of Sample A (R_q= ~ 0.2 nm). On the other hand, as the ICP was held constant at 400 W, a clear trend was observed that the surface roughness increases as the RF powers increased from 5, 35, to 70 W, corresponding to Samples D, E, and F, respectively. The contrast variation in AFM images of Samples C, D, and E becomes more prominent with the ion energy, and the height variation increases to 2 nm in Sample E which the highest DC bias was applied. From the AFM measurements, it is found that the bias voltage controlling the ion energy, determines the morphological quality of etched samples. Rather than physical bombardments (ion density), energetic ion bombardments (ion energy) show a stronger correlation with the surface damage during etching processes.

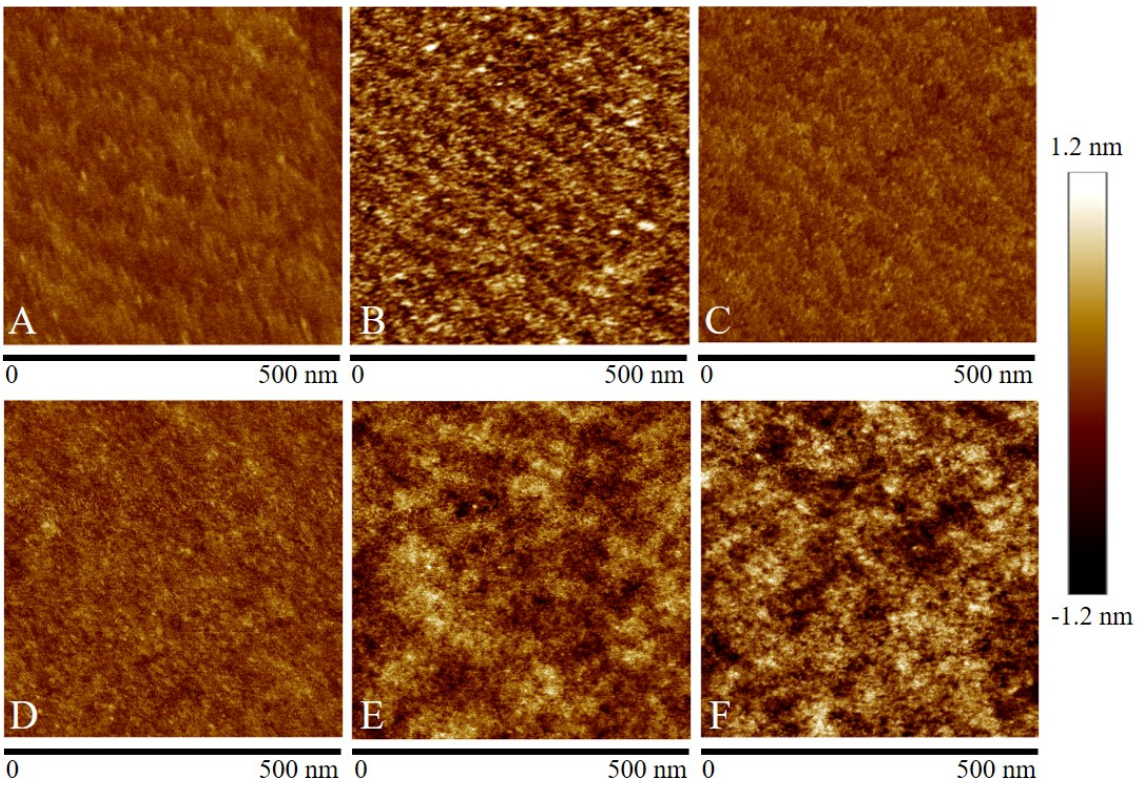

Fig. 5.2. AFM images showing the surface morphology of samples with different ICP etching parameters. Compared to a non-etched surface (Sample A), increasing ICP power (higher ion density) shows a minor effect on the morphology (Samples B, C, and D). Increasing RF power (higher ion energy) shows significant increase on the surface roughness of GaN epilayers (Samples D to F).

5.3.2 Optical properties of etched GaN films

Figure 5.3 shows the CL spectra of Samples A-F with accelerating voltage of 2 kV at room temperature. In Fig. 5.3(Top), the band-edge CL intensity at 3.4 eV of GaN films decreases following ICP etching. With increasing ICP powers from 100 to 400 W (Samples B, C and D), where DC bias varies from 21 to 39 V, the intensity remains about the same; while with increasing RF power (Samples D, E, and F), where DC bias varies from 21 to 159 V, the intensity significantly decreases. At an RF power at 70 W and a DC bias of 159 V (Sample F), the band-edge intensity decreases down to ~ 2% of the intensity of nonetched

one (Sample A). In Fig. 5.3(Bottom), the normalized spectra show the relative intensity of yellow luminescence (YL) at 2.2-2.5 eV, compared to the band-edge intensity increases after etching. The origin of the point defects responsible for yellow luminescence has been attributed to gallium vacancies (V_{Ga}).[112,113] When varying the ICP power (Samples B, C and D), the YL intensity remains about the same; while in the case of varying RF powers (Samples D, E, and F), the YL intensity notably increases. The decrease in the band-edge CL intensity can be explained in terms of gap states acting as nonradiative recombination centers introduced during the etching processes.[114] The higher density of nonradiative recombination centers is related to the ion accelerating voltage. Since higher DC bias produces more damage, the noticeable degradation of band-edge CL performance observed in Samples E and F is quite understandable. On the other hand, the increase in intensity of YL is associated with the formation of point defects near the surface resulting from the energetic ion bombardments. A decrease in the intensity with an increase in the DC bias is indicative of damage induced during the etching process.

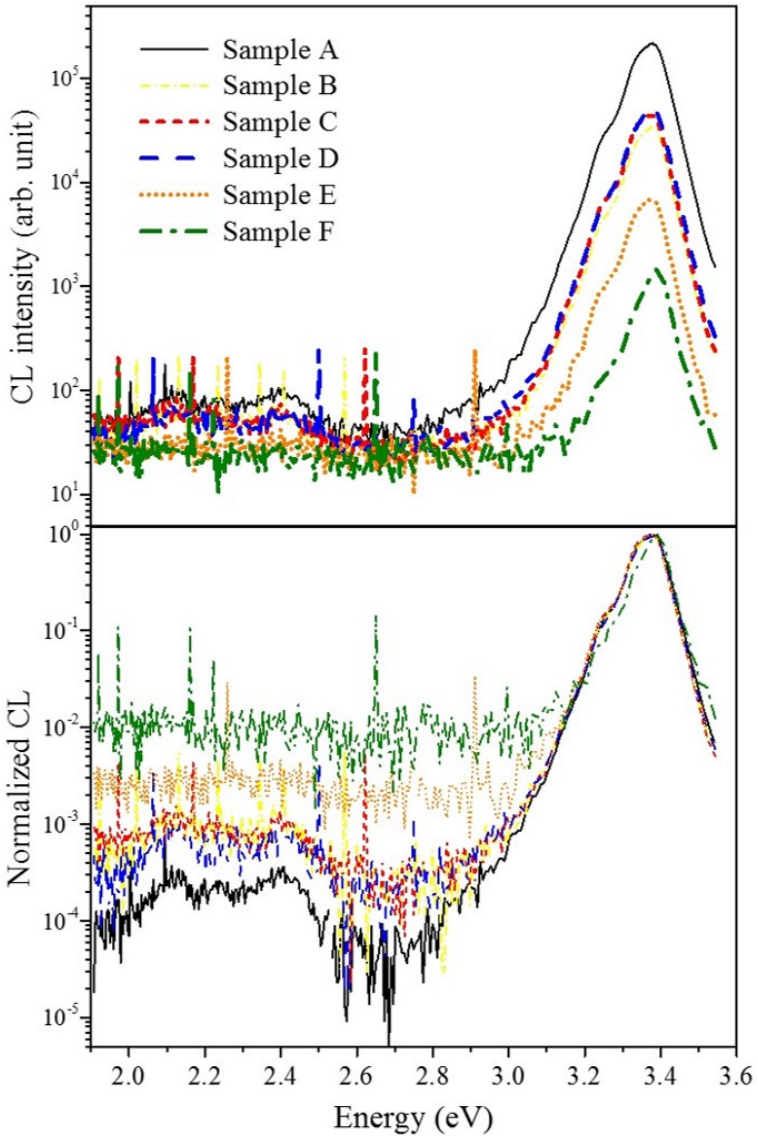

Fig. 5.3. CL spectra of band-edge emissions and yellow luminescence of GaN films. (Top) The band-edge CL intensity decreases following the ICP etching. The intensity shows minor change by increasing ICP powers (Samples B and C), while decreases with increasing RF powers (Samples C, D, and E). (Bottom) The intensity of yellow luminescence (~2.2 eV) increases after etching. The intensity shows minor change by increasing ICP powers (Samples B and C), while increases with increasing RF powers (Samples C, D, and E). (Courtesy of Hanxiao Liu)

In order to further study the damage caused by the etching processes, CL depth profiling is performed at various electron acceleration voltages (2–10 keV), as shown in Fig. 5.4(a). In the cases of 2 and 5 kV, the intensity of band-edge emission decreases with

the accelerating voltage used in the etching processes. In particular, Sample D etched under high ion density but the lowest ion energy, shows the highest CL emission. In the case of 7 kV, the intensity of CL emission of Samples B and C is about the same; the intensity of CL emissions of Samples E and F is also about the same. For an electron beam energy of 10 kV, samples etched with relatively low DC bias, from 21 to 39 V (Samples B, C, and D), show similar CL emission intensities; Samples E and F, etched with relatively high DC bias of 95 and 159 V, respectively, show similar emission intensities. The depth profile of the band-edge intensity compared with the non-etched sample ($I_{etched}/I_{Sample\ A}$) is shown in Fig. 5.4(b). The maximum penetration depths where injected electrons come to a rest, corresponding to different accelerating voltages, are indicated in the *x*-axis.[115,116] An increase in relative intensity with penetration depth indicates that the damage created from the etching is more prominent near the top surface, and decreases with depth. It notes that the luminescence signal is generated within a tear-shaped interaction volume above the maximum penetration depth, with maximum photon generation happening at ~1/3 of the maximum penetration depth. From CL depth profiling, the depth of the ICP-induced damage region can be qualitatively estimated. In order to minimize the etching damage, one can expect that an etching process with a low bias voltage following one with a high bias voltage can reduce the damaged layer and improve the materials properties.

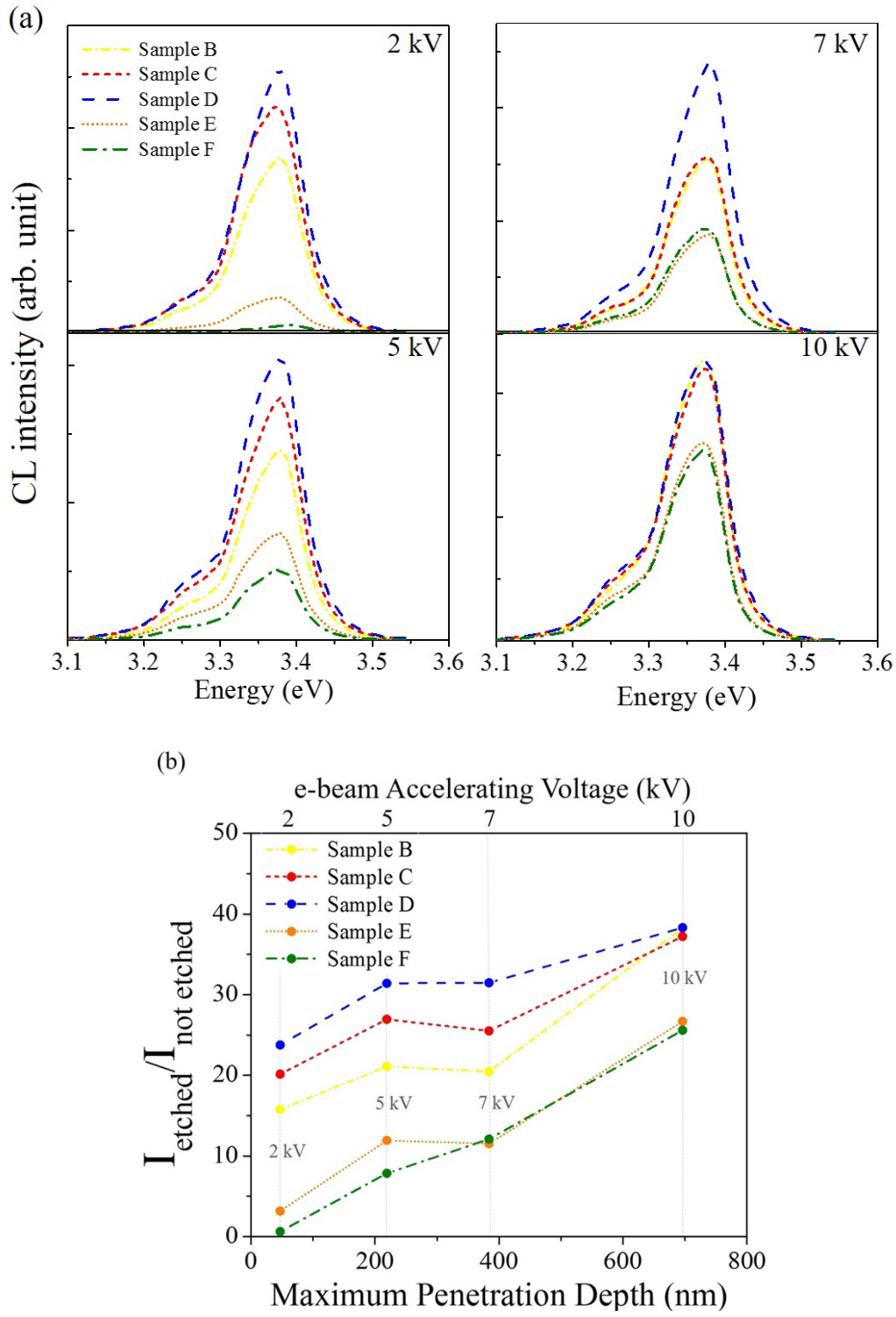

Fig. 5.4. Luminescence for samples with various ICP etching parameters. (a) The band-edge CL intensity of etched samples with four different accelerating voltages. (b) Depth profile of the relative band-edge CL intensity compared with the non-etched Sample A ($I_{etched}/I_{not\ etched}$). (Courtesy of Hanxiao Liu)

In order to correlate etched damage to device performance, two different etching processes (with ICP power of 400 W and RF powers of 5 and 70 W) were applied to two samples to see the effect on the reverse leakage characteristics of GaN *p*-*n* junctions. The samples are *u*-GaN/GaN layers, followed by etched and regrowth, plus a thin *u*-GaN layer insertion layer and a 500 nm *p*-GaN layer. Metal layers were deposited as *p*- and *n*-contacts. More details on the device fabrications can be found in Ref. 117.

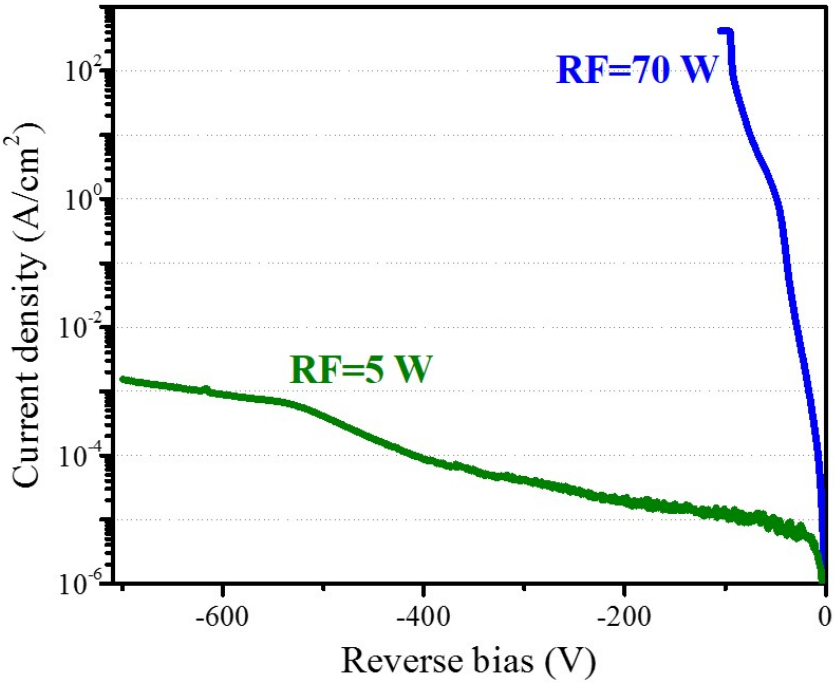

Fig. 5.5. Reverse I-V curves for samples with two different etching parameters (RF powers of 5 and 70 W, and an ICP power fixed as 400 W). The sample etched with a RF power of 70 W shows a larger reverse leakage current. (Adapted from Ref. 116)

Figure 5.5 shows the reverse I-V curves of samples with two different etching parameters (RF powers of 5 and 70 W, and an ICP power fixed as 400 W). In the case of the sample etched with an RF power of 5 W, the reverse leakage current is significantly lower than the one etched with an RF power of 70 W. The reverse leakage current has been attributed to an increase of the surface channel conduction resulting from the etched

damage.[117] Therefore, the sample etched with an RF power of 70 W, where incident ions have a higher energy, shows a larger reverse leakage current.

5.4 Conclusion

The surface morphology and optical properties of GaN films etching with different ICP parameters were investigated. It has been showed that a bias voltage rather than an ion density is the significant cause of plasma-induced damage. A high bias voltage results in a roughened surface due to high energy ion irradiation. The irradiation can also create nonradiative recombination centers and point defects in the vicinity of the surface, leading to a low CL band-edge emission and a high yellow luminescence, respectively. It has also been demonstrated that the depth of damaged can be estimated by CL depth profiling, and an optimized etching parameter to minimize etch-induced damage can be developed.

ACKNOWLEDGMENTS

The materials were grown by Dr. Kai Fu and team in Prof. Yuji Zhao's research group at ASU. This work was supported by the ARPA-E PNDIODES Program monitored by Dr. Isik Kizilyalli. We acknowledge the use of facilities within the Eyring Materials Center at Arizona State University. The device fabrication was performed at the Center for Solid State Electronics Research at Arizona State University.

CHAPTER 6

LATERAL VS. VERTICAL GROWTH OF Mg-DOPED GaN ON TRENCH-PATTERNED GaN FILMS (*)

6.1 Introduction

Some of the current designs of high-power GaN-based devices involve lateral *p*-*n* junctions, which can be achieved via etch-and-regrowth steps.[117] This approach may consist of an *n*-GaN film which is selectively etched to produce vertical patterns, with regrown Mg-doped GaN filling the trenches. The regrowth of Mg-doped GaN films at the selectively-etched regions involves growth perpendicular to the basal plane as well as lateral growth from the sidewalls. Uniform film growth and uniform Mg distribution in *p*-GaN are required to deplete the *n*-GaN channel in a vertical-junction FET under a normally OFF operation.[118] Visualizing growth from different growth fronts and the nature of Mg incorporation is essential for the understanding of the electronic performance of devices.

Pressure and growth temperature play a significant role on the anisotropic growth of GaN films in epitaxial lateral overgrowth (ELO) on mask pattern substrates.[119] Impurity incorporation modifies the growth rates of GaN on basal plane and inclined facets,[106,120-122] resulting in planarization of GaN films by coalescence of expanding facets in two-step ELO on patterned substrates.[120] However, there is not much knowledge about the structural and optical properties of Mg-doped GaN films regrown at selectively-etched areas.

---

*Results included in this chapter have been submitted as:
P.-Y. Su, H. Liu, C. Yang, K. Fu, H. Fu, Y. Zhao, and F. A. Ponce, *Lateral and vertical growth of Mg-doped GaN on trench-pattern GaN films,* submitted to Appl. Phys. Lett. on Jun. 22, 2020.

In this work, secondary-electron (SE) imaging and cathodoluminescence (CL) monochromatic mapping are used to study the microstructure and optical properties of Mg-doped GaN films grown at selectively-etched area (trench patterns). The correlation between anisotropic growth and the variation in acceptor incorporation efficiency in regions along the sidewall and near-basal plane is established.

6.2 Experimental Details

The epitaxial structures were grown by metal-organic chemical vapor deposition (MOCVD) on free-standing *c*-plane GaN substrates, with hydrogen as the carrier gas, at a growth temperature of 1050 °C, and a reactor pressure of 200 Torr. The Ga and N sources were trimethylgallium (TMGa) and ammonia (NH_3). The precursor for Mg doping is bis(cyclopentadienyl)magnesium (Cp_2Mg).

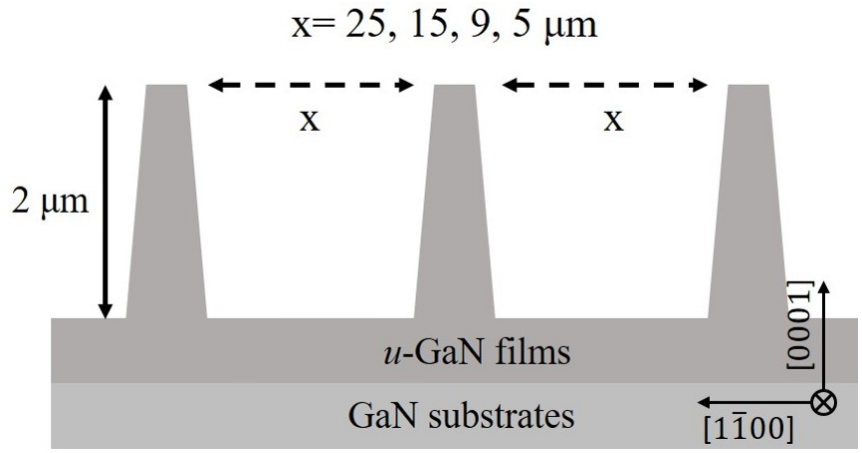

Fig. 6.1. Schematic diagram of trench pattern on GaN substrates. The width of trenches varies from 35 to 5 μm, with a depth of 2 μm. A 2-μm-thick Mg-doped film was subsequently deposited on the trench pattern.

Our thin film structures consist of 4-μm-thick undoped GaN (*u*-GaN) films grown on *c*-plane GaN substrates. The *u*-GaN layers were selectively etched to produce a periodic

array of two-sided sloped trenches with a depth of 2 μm. The trench widths were 25, 15, 9, and 5 μm, as shown in Fig. 6.1.

Etching was done by photolithography and chlorine-based inductively coupled plasma (ICP) dry etching at an ICP/RF power of 400/70 W, a Cl_2/BCl_3/Ar flow rate of 30/8/5 sccm, and a pressure of 0.67 Pa. Following the etching, a 2-μm-thick Mg-doped GaN was grown over the trench pattern. The Mg-doped GaN film was grown with a TMGa flow rate of 12 sccm and a Cp_2Mg flow rate of 100 sccm, at a temperature of 975 °C, for a Mg concentration of 3×10^{19} cm^{-3} measured by secondary ion mass spectroscopy. Post-growth thermal activation of Mg-doped GaN was performed using rapid thermal annealing at 700 °C for 20 mins in a nitrogen atmosphere.

The microstructure of Mg-doped GaN films was studied by secondary electron microscopy (SEM), from cross-section samples prepared by mechanical polishing using diamond lapping films. CL system consists of a JEOL 6300 scanning electron microscope (SEM) connected to an Oxford CL2 monochromator and a photomultiplier tube. A correlation with microscopic optical characteristics was obtained using CL monochromatic mapping by setting the monochromator to a certain wavelength and recording the spatial variation of luminescence intensity over an area, with an electron beam current of 100 pA and an acceleration voltage of 7 kV in a JEOL 6300 scanning electron microscope equipped with an Oxford CL2 monochromator and with a photomultiplier tube.

6.3 Results and Discussion

6.3.1 Structural properties of GaN:Mg films grown on trench patterns

SE images of Mg-doped GaN films grown on trench patterns are shown in Fig. 6.2. where Mg-doped GaN has a brighter SE contrast than *u*-GaN.[123] The variation in the surface morphology of Mg-doped GaN results from competition between lateral growth from the sidewall and vertical growth from the bottom surface, leading to notches located at the top center of the trenches, as seen in Fig. 6.2. For wide trench widths, the length of the top-sidewall is larger than 4 μm, and the outer slope increases with decreasing trench width. When the trench width is 5 μm, growth from opposite sides of the trench have coalesced, and a *c*-plane front creates a flat surface. The anisotropic growth of Mg-doped GaN films results from three factors: one is due to the presence of the sidewall, two is a dependence on growth temperature and pressure, and three is Mg-doping effects.[78,106,119,124] The sidewall can be viewed as a highly tilted facet consisting of a high density of basal-plane steps, each step being an efficient sink for adatoms.[78,124] Growth temperature and chamber pressure do significantly affect the growth morphology (lateral vs vertical growth direction).[124] Mg doping promotes the diffusion of adatoms,[106] promoting the accumulation of adatoms in the vicinity of sidewalls. The competition between lateral and vertical growth results in a thicker layer near the sidewalls and a thinner layer away from the sidewalls near the trench center.

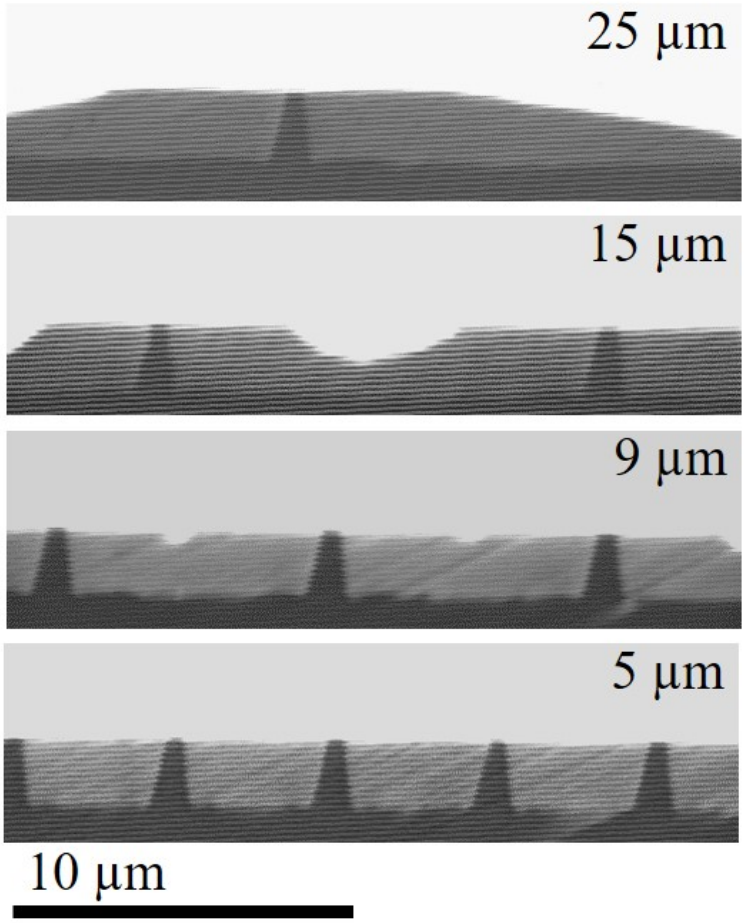

Fig. 6.2. Cross-section secondary-electron images of Mg-doped GaN films grown on trench patterns. Mg-doped GaN has a brighter contrast than the *u*-GaN. Its surface is flat next to the fin, and decreases after a distance of about 3.8 μm. The film thickness at the trench center increases with decreasing trench width. For a trench width of 5 μm, the Mg-doped GaN from opposite sides coalesce and a flat surface is achieved. (Courtesy of Hanxiao Liu)

6.3.2 Optical properties of GaN:Mg films grown on trench patterns

Monochromatic CL images of optical emissions at 2.85 and 3.25 eV of Mg-doped GaN films grown on the trench patterns with various widths are shown in Figs. 6.3. The 3.25 eV peak is due to transitions from a shallow-donor to a Mg-acceptor, and the 2.85 eV peak is due to deep-donor to Mg-acceptor transitions.[93,125-127] When the magnesium concentration

increases, the intensity of the 3.25 eV emission decreases and the 2.85 eV emission increases.

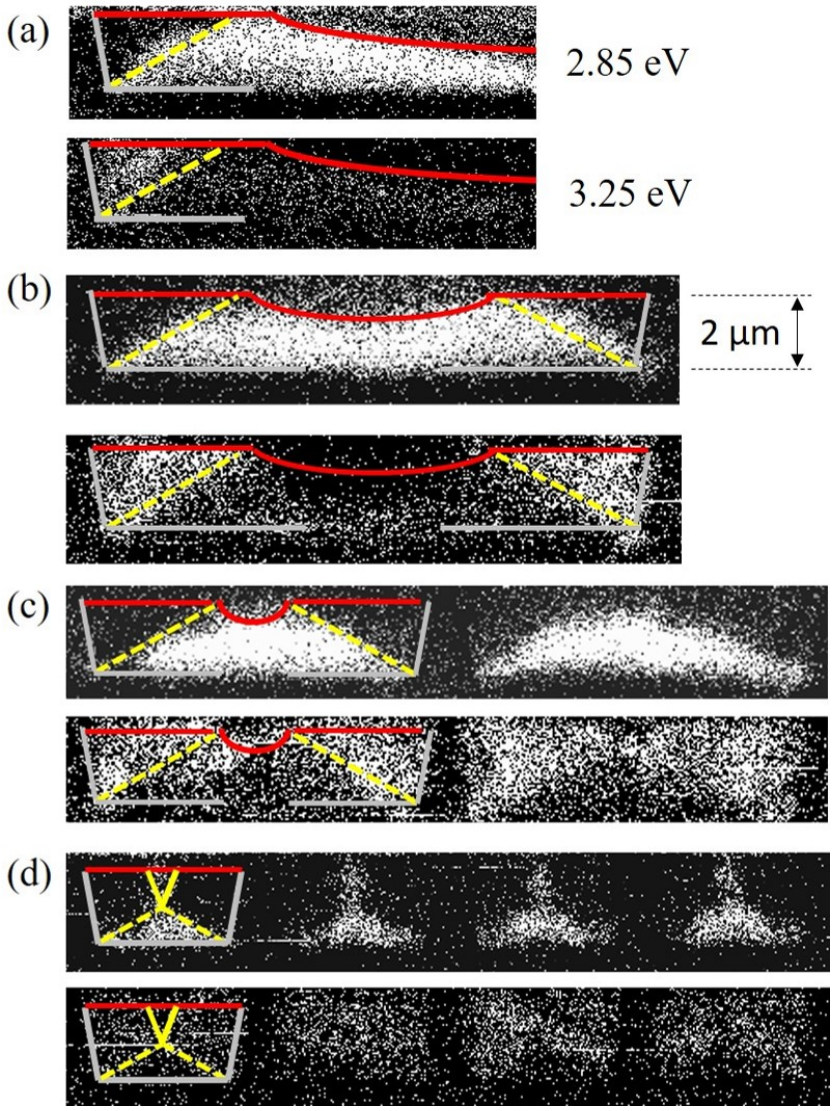

Fig. 6.3. Monochromatic CL mappings of GaN:Mg films at 2.85 and 3.25 eV. Trench patterns with a width of (a) 25 µm, (b) 15 µm, (c) 9 µm, and (d) 5 µm. The Mg-doped GaN shows a strong emission at 2.85 eV near the center of the trench base; while a strong emission at 3.25 eV is observed near the sidewall. The 2.85 and 3.25 eV emissions are complementary. (Courtesy of Hanxiao Liu)

When the trench is partially filled by Mg-doped GaN, as in Figs. 6.3(a)-(c), the upper CL images at 2.85 eV show a lower emission in the vicinity of sidewalls and a higher

intensity in the lower 3.25 eV images. In case (d), where the trench is fully filled by Mg-doped GaN, the upper CL image at 2.85 eV also shows the lower emission in the vicinity of the sidewalls, and additionally a region of higher emission is observed at the top center of the trench, the results when the lateral fronts coalesce and basal plane growth leads to a flat surface. As in Figs. 6.3(a)-(c), the lower CL image taking at 3.25 eV shows complementary emissions.

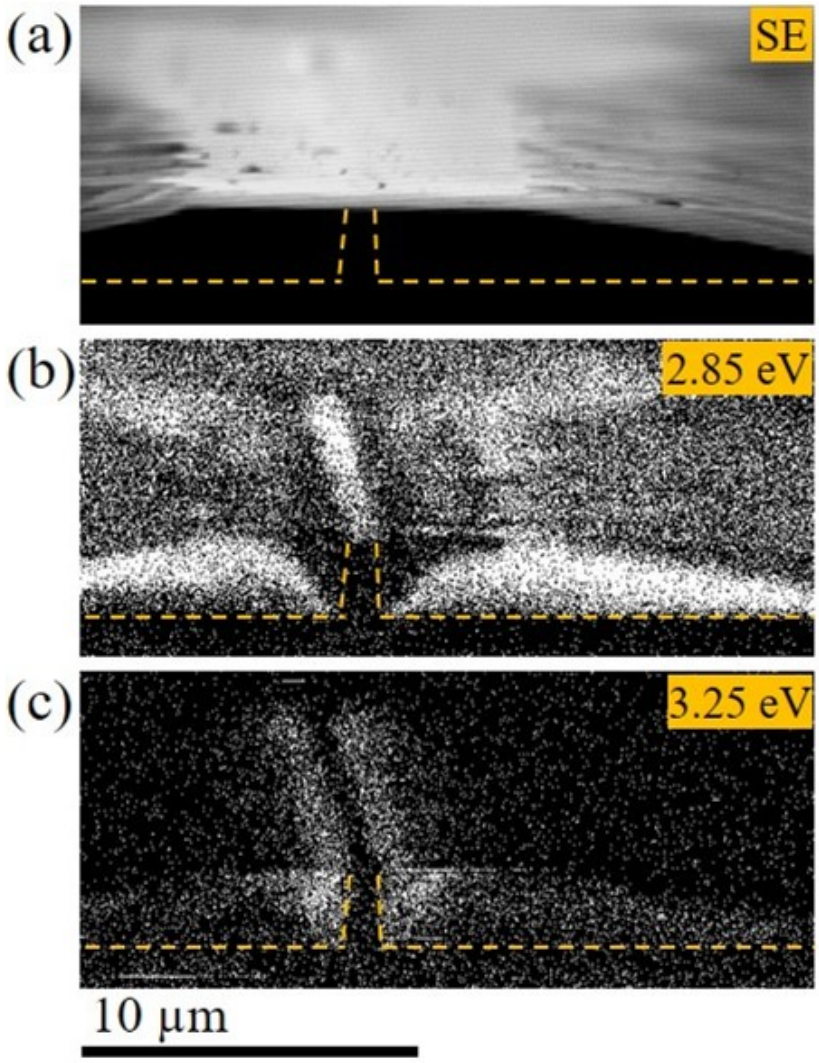

Fig. 6.4. Tilted cross-sectional secondary-electron and monochromatic CL images of Mg-doped-GaN grown on trench patterns with a width of 25 μm. A strong 2.85 eV emission is observed on top of the mesa. The 2.85 and 3.25 eV emissions are complementary. (Courtesy of Hanxiao Liu)

Figure 6.4 shows tilted cross-section SE and CL images for the case where a trench width is 25 μm. Complementary emissions at 2.85 and 3.25 eV are observed near sidewalls and trench bases, as discussed earlier. Note that a strong emission at 2.85 eV is also observed on top of the mesa, which is barely seen in the edge-on cross-section images in Fig. 6.3.

Previous reports have indicated that for GaN grown along highly tilted facets the doping efficiency of magnesium is reduced, leading to the formation of semi-insulating regions (p^--GaN).[107,127] Note that the *p*-GaN region near the center of trenches results from the vertical growth along the basal plane.

From the monochromatic CL images in Figs. 6.3 and 6.4, the geometry of etch-and-regrowth region consisting of trenched-patterns, *p*-GaN and p^--GaN can be determined: a sidewall with 2 μm in height has sides slanted approximately 78° toward the basal plane, resulting from the ICP etching. The *p*-GaN and p^--GaN regions are separated by a yellow dash line tilted about 28° away from the basal plane, independent of the trench widths, as in Fig. 6.5(a). This boundary corresponds to a $(01\bar{1}1)$ plane originating from the fin sidewall, and vertical growth on (0001) basal planes. The two growth fronts meet at a boundary with an angle of 28° with the basal plane, as shown in Fig. 6.5(b). The image suggests that when a (0001) monolayer is grown, two monolayers on a $(01\bar{1}1)$ plane are formed, in order to provide coincidence between the lateral and vertical growth fronts. The anisotropic growth of Mg-doped GaN along the sidewall facet results in a lateral growth rate faster than that the vertical growth rate with a ratio of lateral to vertical growth about 2. In the case where a trench width is 5 μm, the thick sidewalls from two sides coalesce to fill the trench. Note that the vertical growth reappears and planarizes the film structure

when the sidewalls from opposite sides coalesce at the top center of the trench, leading to a strong CL emission at 2.8 eV observed in Fig. 6.3(d).

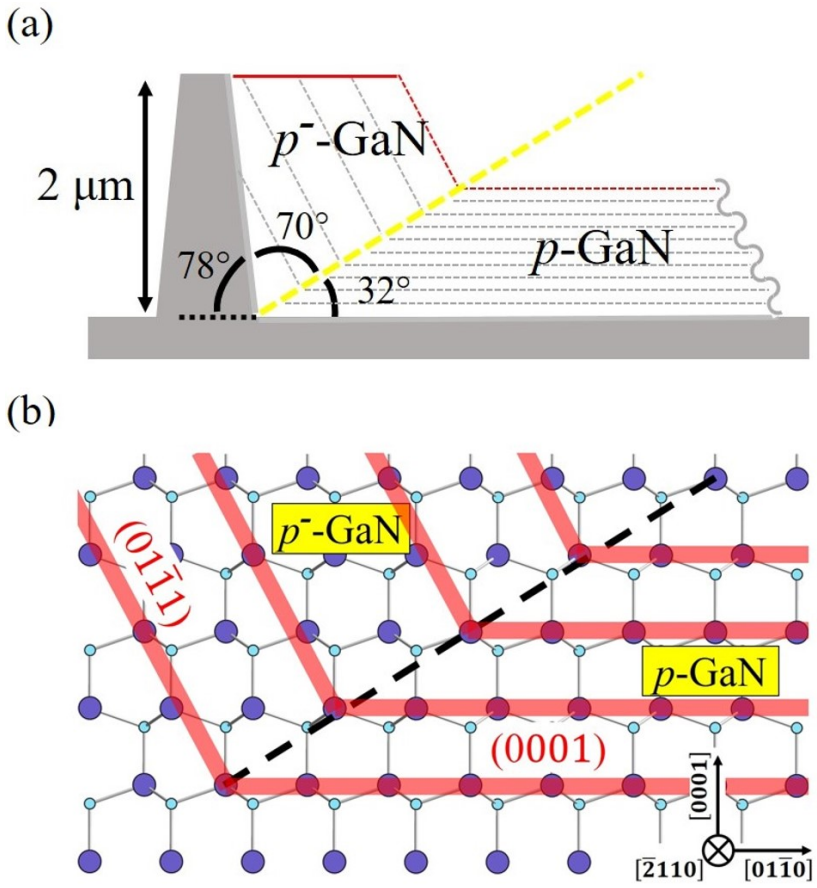

Fig. 6.5. Schematic diagrams of Mg-doped GaN grown on trench patterns. (a) The sidewall slants 78° toward the basal plane, resulting from the ICP etching. The *p*-GaN and *p*⁻-GaN regions are separated by a boundary (yellow dash line) making an angle of 32° with the basal plane, independent of trench widths. (b) The boundary between *p*-GaN and *p*⁻-GaN regions corresponds the coalescence of growth fronts on $\{01\bar{1}1\}$ and {0001} planes, with a ratio of lateral to vertical growth of about 2.

6.4 Conclusion

The growth evolution and non-uniform luminescence of Mg-doped GaN films grown on trench patterns have been studied. The anisotropic growth of Mg-doped GaN films along sidewalls due to the promotion of lateral growth during Mg incorporation is observed.

CL mappings show the non-uniform luminescence at 2.85 and 3.25 eV, resulted from the differences in acceptor incorporation efficiency in regions grown along different growth fronts. The ratio of lateral to vertical growth determined from the CL images is about 2.

ACKNOWLEDGMENTS

The materials were grown by Dr. Kai Fu and team in Prof. Yuji Zhao's research group at ASU. This work was supported by the ARPA-E PNDIODES Program monitored by Dr. Isik Kizilyalli. We acknowledge the use of facilities within the Eyring Materials Center at Arizona State University. The device fabrication was performed at the Center for Solid State Electronics Research at Arizona State University.

CHAPTER 7

SUMMARY AND FUTURE WORK

7.1 Summary of the Dissertation

In this dissertation, an investigation on the structural and optical properties of III-V semiconductor for photovoltaics and power electronic applications has been reported. TEM and AFM have been used to analyze the microstructures which are closely related to the nature of the materials and their growth conditions. CL has been used to characterize the optical properties, correlated with the structural properties.

In Chapter 3, InAs QDs are grown by MOCVD and covered with GaAs capping layers. The effects of QDs deposition time and thickness of GaAs capping layers on the structure of GaInP as barrier layers have been studied.[128] A shorter QDs deposition time and thinner capping layers lead to a disordered phase of GaInP layers with random distribution of group III elements. As the QDs deposition time and thickness of capping layers increase, GaInP layers show ordered with alternating In- or Ga-plane lying along {111} directions, and a shrinkage of the bandgap from 1.92 to 1.85 eV is observed. The floating indium accumulated at the growth front due to difficulty of incorporation during growth of the InAs QDs, is attributed to the structural transition in GaInP layers. The excess indium interferes with the group-III sublattice ordering mechanism, and gives rise to a disordered GaInP layer.

In Chapter 4, the effects of vicinal substrates and growth rates on surface morphology of Mg-doped GaN epilayers grown on vicinal GaN substrates have been studied.[124] As the miscut angle increases, individual steps tend to coalesce into step bunches to form hill-and-valley morphology. After Mg is incorporated, periodic surface steps are observed on the

surface. Facets with different steps density coexist on the surface in order to conserve the net orientation, and the unit height of atomic steps becomes bilayers from a monolayer as the surface tilting angle increases. It is also showed that slower growth rates can enhance step-flow growth and suppress step bunching, leading to higher *p*-type doping efficiency.

In Chapter 5, the effects of inductively coupled plasma (ICP) etching processes by varying RF and ICP powers on GaN epilayers are investigated. It has been showed that the RF power which controls ions energy with changing dc biases, significantly influences the films properties. Higher ions energy enhancing the bombardment effect, results in a rougher surface morphology, a decrease in intensity of band-edge emission, and a higher yellow luminescence of GaN films.

In Chapter 6, the anisotropic growth and non-uniform luminescence of Mg-doped GaN grown on trench patterns have been observed. For the growth conditions lateral growth on the trench sidewall occurs at a faster rate than on the trench base. With a narrow trench width, growth fronts from the two sidewalls coalesce and leads to eventual planarization of the film. The regions with lateral and vertical growth of the Mg-doped GaN films grown on trench patterns have been imaged, and a lateral-to-vertical growth rate ratio is about 2.

7.2 Future Work

7.2.1 Towards Type-II Quantum Dots for Higher IBSC Efficiencies

Most QDs used in intermediate band solar cells are made of InAs QDs embedded in a host (matrix) GaAs material. They are called Type-I QDs, which form a straddling band offset, attracting both electrons and holes towards the QDs, as shown in Fig. 7.1(a).[129] Therefore, two sets of bound states at energy levels within the bandgap of matrix are

formed in the both valence and conduction bands. It has been reported that sub-bandgap adsorptions between hole bound states are attributed to the voltage reduction of the intermediate band solar cells.[127] In other materials systems (for examples: InP QDs/GaInP matrix and InAsP QDs/GaAs matrix), a staggered band offset is formed to attract electrons and repel holes, called Type-II QDs, as shown in Fig. 7.1(b).[131,132] The hole bound states are not present in this case, expecting to minimize an undesirable voltage reduction in solar cells applications. On the other hand, the misfit strain between QDs and matrix can alter the local band edges, creating a ring shape potential well to capture the holes surrounding the QDs.[133] Therefore, the overlap between electron and hole wavefunctions is reduced, leading to lower electron-hole recombination and a longer carrier radiative lifetime.

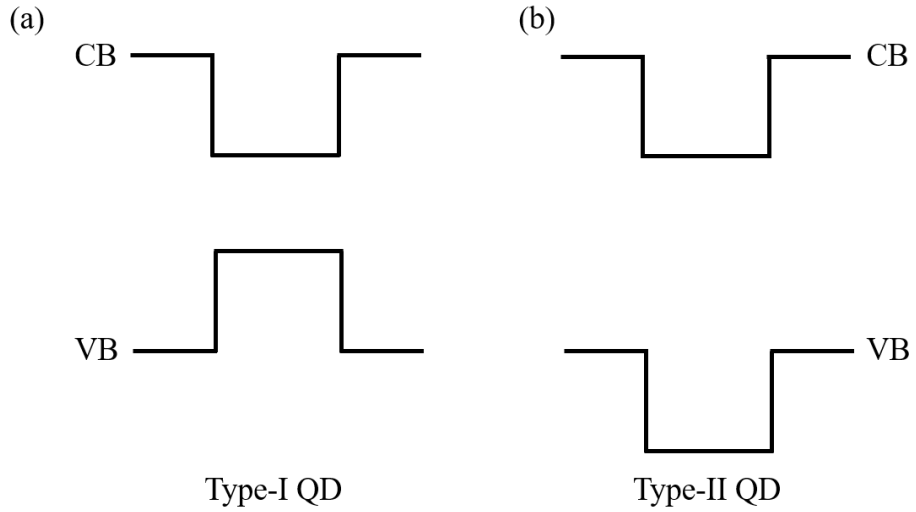

Figure 7.1 Schematic diagrams show band alignments of Type-I and –II quantum dots. (a) Type-I QD shows a straddling band offset, trapping both electrons and holes. (b) Type-II QD shows a staggered band offset, attracting one type of carriers (electrons) and repel the other one (holes).

Chapter 3 contained results from Type-I QDs. Type-II QDs have more demanding refinements. We did some work which revealed the difficulty as discussed next. One of the Type-II QDs systems has been studied, which is InAsP QDs embedded in a GaInP matrix.

Figure 7.2(a) shows the relationship of misfit strain between deposited materials and substrate, versus the thickness of deposited materials for spontaneous island formation. In order to obtain coherent islands, three monolayers of InAsP were deposited on a GaInP substrate. The InAsP QDs/GaInP sample was grown by metalorganic vapor phase epitaxy on (001) GaAs substrates in an Aixtron AIX 200 horizontal reactor at 100 mbar. A pre-growth treatment at 720 °C for de-oxidation was applied to the GaAs substrates for 15 min under AsH_3 overpressure. The hydrogen carrier gas flow rate was 8 liters/min. The precursors were tri-methyl gallium (TMGa), tri-methyl indium (TMIn), phosphine (PH_3) and arsine (AsH_3). GaAs was grown at 630 °C at a growth rate of 0.16 nm/s and a V/III ratio of 160. The Ga/(Ga + In) gas phase ratio was calibrated for growth of $Ga_{0.5}In_{0.5}P$ layers at 650 °C, with a growth rate of 0.27 nm/s and a V/III ratio of 345. The schematic structure of the sample is shown in Fig. 7.2(b). The growth sequence was as follows: A 500-nm-thick GaAs buffer layer was grown on an *n*-doped (001) GaAs substrate, followed by a 500-nm-thick $Ga_{0.5}In_{0.5}P$ layer. The active region consists of an InAsP QD layer and GaInP capping film. The QDs are grown with an amount of InAsP deposition equivalent to 3-monolayer-thick InAsP layers at 580 °C. After the QD growth, the temperature was being raised to 650 °C, with a ramp rate of 46 °C/min. After reaching 650 °C, the temperature was held constant for 1.5 min to achieve surface stabilization. Then, 30 and 70 nm thick $Ga_{0.5}In_{0.5}P$ layers acting as the capping layer and barrier, respectively, were grown; and the growth sequence of the active region and barrier was repeated five times. An extra QD layer was grown at the top surface for the purpose of determining the dot morphology and distribution.

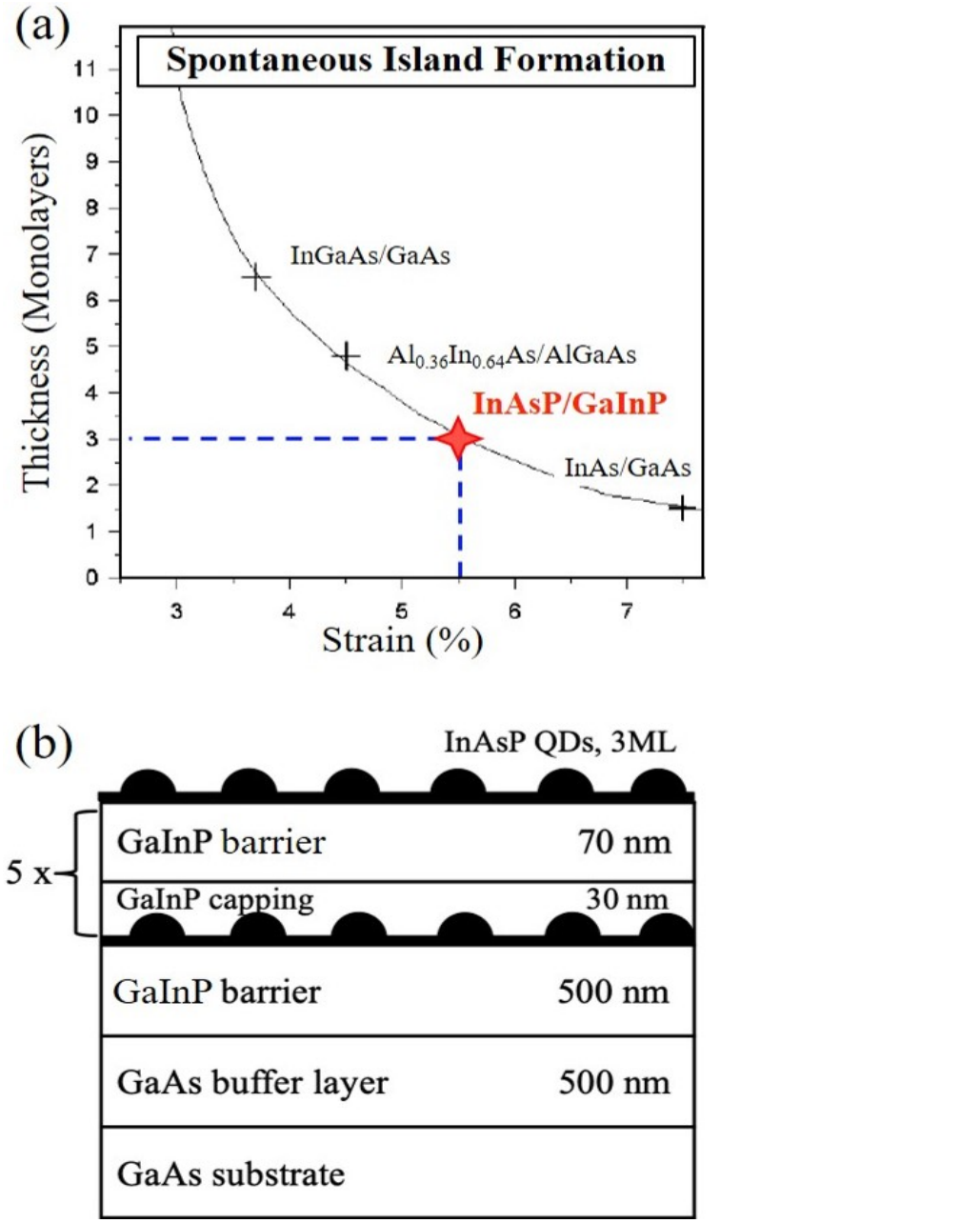

Figure 7.2 Strain for island formation and schematic diagram of InAsP QDs/GaInP (a) Thickness of deposited materials vs. strain for spontaneous island formation. (b) Schematic diagram of the InAsP QDs/GaInP thin film structure. (Courtesy of Dr. Patricia L. Souza)

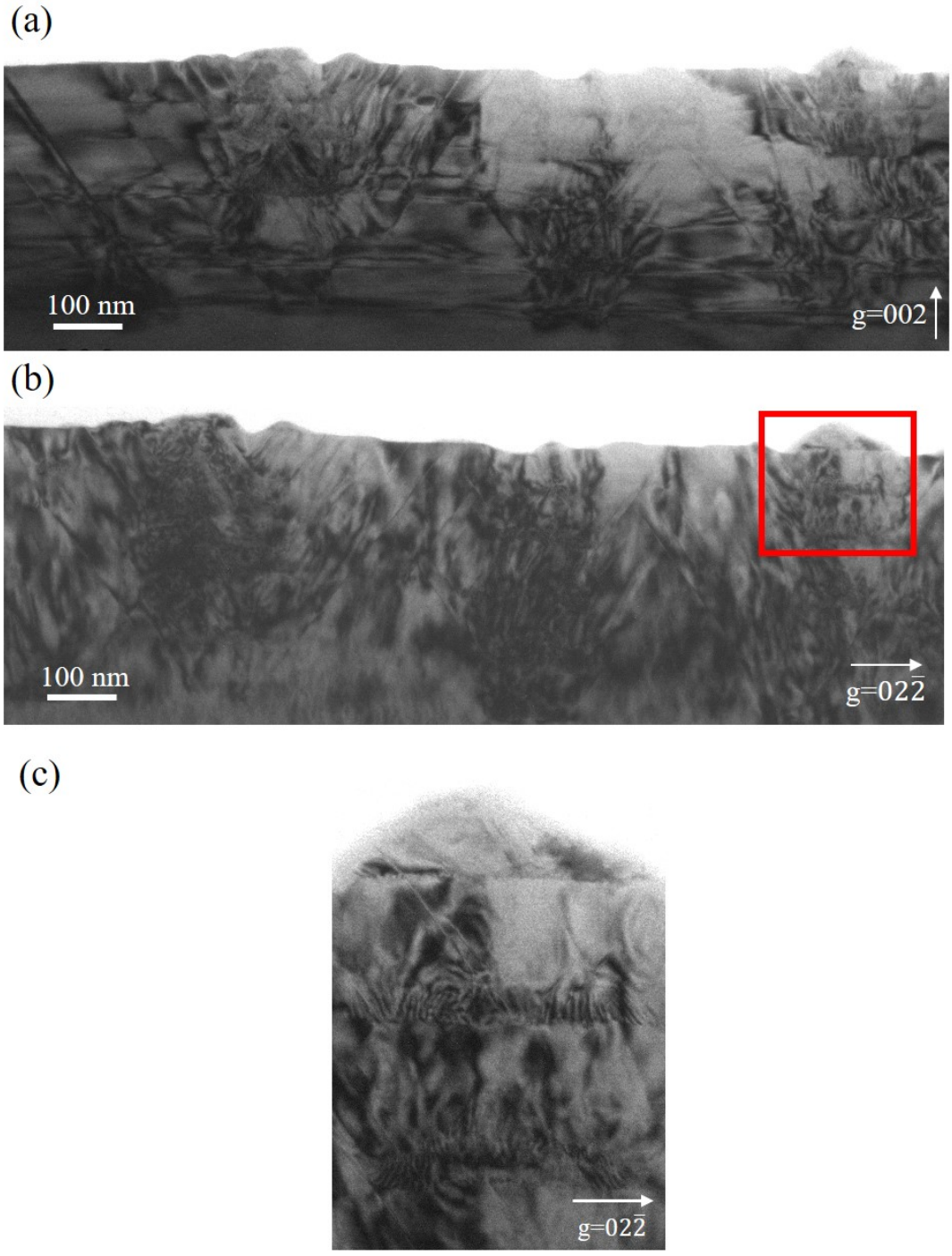

Figure 7.3 TEM two-beam bright-field images of InAsP QDs/GaInP thin film structure under two different diffraction conditions. (a) Image taken under the g=002 condition. (b) Image taken under the g=02$\bar{2}$ condition. (c) High magnification image taken from the marked region in (b), with the presence of Moiré fringes at the interfaces between InAsP QDs and GaInP layers.

TEM two-beam bright-field imaging was performed on the sample to study the strain and the structure of QDs, as shown in Fig. 7.3. The images in Figs. 7.3(a) and (b) show five periods of dislocations emanated from the dots, forming V-shape defects lying on {111} planes are generated, in order to relax the lattice mismatch strain between QDs and a substrate. Fig. 7.3(c) shows a high magnification image taken from the marked region in Fig. 7.3(b) with the presence of Moiré fringes at the interface between QDs and substrate. The fringes resulted from the interaction of two incoherent waves, indicates the lattice misfit relaxation occurring at the interface.

Different growth parameters were modified, including changes of the amount of QDs deposition, and the materials of capping layers, in order to improve the materials quality. However, the samples are still defective, and the generation of misfit dislocations cannot be suppressed. It is attributed to the difficulty of controlling the stoichiometry of group-V elements. This is the work that need to be done next, as discussed next. To modify the alloy composition of ternary $III_xIII_{1-x}V$ and $IIIV_xV_{1-x}$ QDs are very different. Ternary $III_xIII_{1-x}V$ QDs have been produced and studied extensively, the concentration of two group-III element is closely proportional to their arrival rates to the surface.[134] Considering the fact that incorporation of group-III elements is close to 100%, the stoichiometry shows easier to control in this system. However, for the growth of $IIIV_xV_{1-x}$ QDs, the higher volatility of group-V elements complicates the nucleation of islands.[135] Also, the difference in decomposition temperature for arsine and phosphine may lead to the incomplete pyrolysis at lower growth temperatures.[136] In other words, arsine is fully activated, but phosphine is not, at the given temperature. And equal flows of arsine and phosphine would lead to form QDs with higher concentration of arsenic, resulting in the QDs with higher misfit strain.

To increase the growth temperature may not work because indium would re-evaporate to the gas phase at high temperatures. To solve the problems, the growth rate has been modified to control the growth in a kinetic region.[135] It has been shown that this method can control the mixing of group-V elements and improve the stoichiometry of $IIIV_xV_{1-x}$ QDs. On the other hand, to increase the phosphine flow rate may also balance the compositions of As and P elements in the QDs, leading to the formation of coherent islands.

7.2.2 Growth of GaN:Mg on Different Substrates and Growth Conditions

Hydride vapor phase epitaxy (HVPE) is currently the most common approach to fabricate GaN substrates with a low dislocation density (of the order of 10^6 cm^{-2}) and at a relatively high growth rate (>100 μm per hour).[137,138] As discussed in Chapter 4, the steps present on vicinal HVPE-GaN substrates facilitate lateral step-flow growth, leading to a smooth surface morphology. The substrate with a normal surface tilt toward the $< 1\bar{1}00 >$ direction results in straight and well-defined step edges on *p*-GaN surfaces. For *p*-GaN epilayer grown on a vicinal HVPE-GaN substrates with a tilt toward both $< 1\bar{1}00 >$ and $< 11\bar{2}0 >$ directions, straight steps with some degree of jaggedness were observed, as shown in Fig. 7.4, and the jaggedness correlates to the miscut toward the $< 11\bar{2}0 >$ direction.[139]

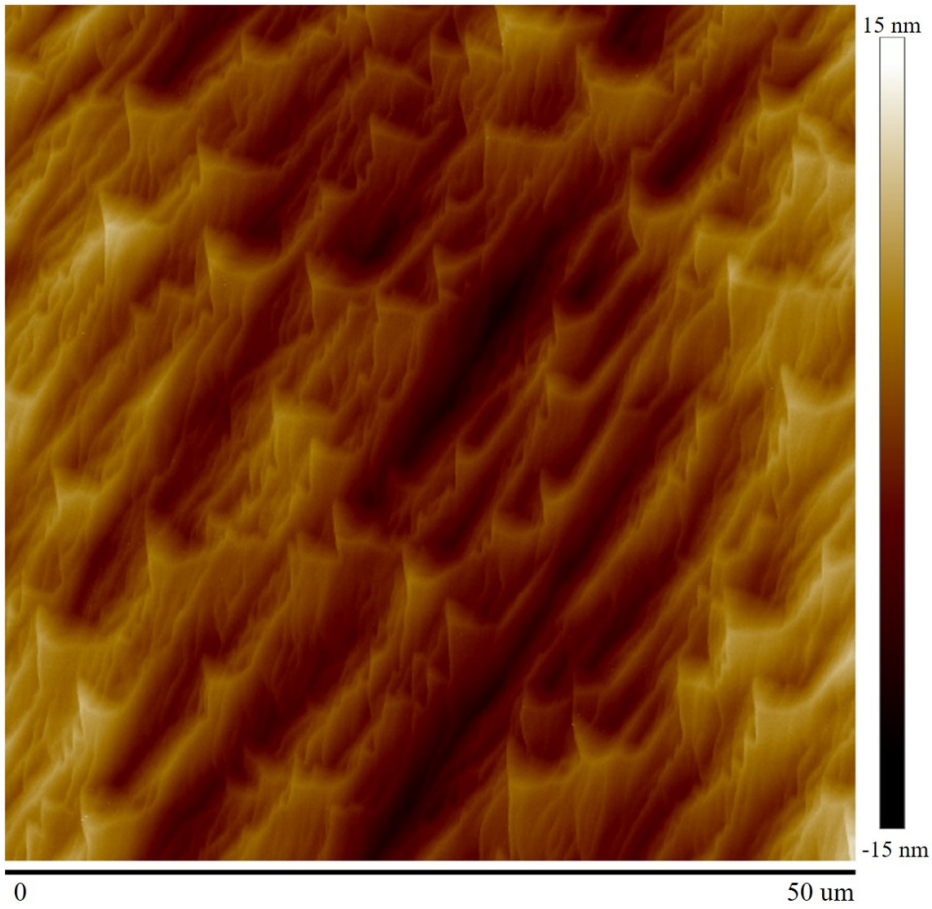

Figure 7.4 AFM image shows the surface morphology of *p*-GaN epilayer grown on a vicinal GaN substrate, with tilts toward both $< 1\bar{1}00 >$ and $< 11\bar{2}0 >$ directions. Straight steps with some degree of jaggedness are observed.

It would be interesting to study the step evolution of *p*-GaN layers grown on vicinal GaN substrates toward $< 11\bar{2}0 >$ or both $< 1\bar{1}00 >$ and $< 11\bar{2}0 >$ directions with larger tilting angles and see how they correlate with the optical properties. Understanding growth on *m*-plane should be explored.

In addition, it has been reported that the growth rates in vertical and lateral directions can be controlled by the reactor pressure, the growth temperature, and the [Mg]/[Ga] mole ratio.[119,120] It is found that decreasing temperature and increasing pressure stabilize the sidewall facets growth.[119] On the other hand, the ratio of lateral to vertical growth increases

with the Mg concertation.[120] In the case of the growth on vicinal N-polar $(000\bar{1})$ GaN/sapphire substrates, it has been shown that to keep the Mg/Ga ratio in the intermediate range of 10^{-3} can maintain the smooth surface morphology of *p*-GaN layers on vicinal N-polar $(000\bar{1})$ GaN/sapphire substrates.[140] Further study can be done on the surface morphology of GaN layers doped with different Mg doping concentrations, and to see the local doping efficiency on vicinal (0001) GaN substrates.

On the other hand, it has been observed that the step flow is disturbed or even interrupted as it meets the pinholes on the GaN surface. Such disturbance also effects the rate of step advancement, leading to step bunching. In order to improve the surface morphology or the interface quality for devices applications, it is necessary to further reduce the dislocation density of GaN substrates. Recently, the ammonothermal growth of GaN substrates shows a higher structural quality than the HVPE-GaN substrates.[141,142] The dislocation density of ammonothermal GaN crystal is in an order of 10^3 cm^{-2}, comparing with that of typical HVPE GaN crystal (of the order of 10^6 cm^{-2}). In addition, the crystal lattice of ammonothermal GaN is much flatter (i.e. built-in stress is minor), where the HVPE GaN is well known for its lattice bending. Therefore, the layers grown on vicinal ammonothermal GaN substrates are expected to maintain the step-flow growth in terms of the better crystal quality, resulting in a smooth morphology and improved acceptor incorporation efficiency.

REFERENCES

1. F. A. Ponce and D. P. Bour, *Nitride based semiconductors for blue and green light-emitting devices*, Nature **386**, 351 (1997).

2. C. Y. Yeh, Z. W. Lu, S Froyen, and A. Zunger, *Zinc-blende–wurtzite polytypism in semiconductors*, Phys. Rev. B **46**, 10086 (1992).

3. J. S. Blakemore, *Semiconducting and other major properties of gallium arsenide*, J. Appl. Phys. **53**, 123 (1982).

4. D. L. Partin, L. Green, D. T. Morelli, J. Heremans, B. K. Fuller, and C. M. Thrush, *Growth and characterization of indium arsenide thin films*, J. Electron. Mater. **20**, 1109 (1991).

5. S. Adachi, *GaAs, AlAs, and $Al_xGa_{1-x}As$: Material parameters for use in research and device applications*, J. Appl. Phys. **58**, R1 (1985).

6. S. M. Sze and J. C. Irvin, *Resistivity, mobility and impurity levels in GaAs, Ge, and Si at 300°K*, Solid State Electron. **11**, 599 (1968).

7. A. G. Milnes and A.Y. Polyakov, *Indium arsenide: a semiconductor for high speed and electro-optical devices*, Mater Sci Eng B-Solid **18**, 237 (1993).

8. H. J. Yeh and J. S. Smith, *Fluidic self-assembly for the integration of GaAs light-emitting diodes on Si substrates*, IEEE Photon. Technol. Lett. **6**, 1041 (1994).

9. N. Kirstaedter, O. G. Schmidt, N. N. Ledentsov, D. Bimberg, V. M. Ustinov, A. Yu. Egorov, A. E. Zhukov, M. V. Maximov, P. S. Kop'ev, and Zh. I. Alferov, *Gain and differential gain of single layer InAs/GaAs quantum dot injection lasers*, Appl. Phys. Lett. **69**, 1226 (1996).

10. V. Aroutiounian, S. Petrosyan, A. Khachatryan, and K. Touryan, *Quantum dot solar cells*, J. Appl. Phys. **89**, 2268 (2001).

11. C. G. Bailey, D. V. Forbes, R. P. Raffaelle, and S. M. Hubbard, *Near 1 V open circuit voltage InAs/GaAs quantum dot solar cells*, Appl. Phys. Lett. **98**, 163105 (2011).

12. A. Luque and A. Martí, *Increasing the efficiency of ideal solar cells by photon induced transitions at intermediate levels*, Phys. Rev. Lett. **78**, 5014 (1997).

13. W. W. Bi, H. H. Kuo, P. Ku, and B. Shen, *Handbook of GaN semiconductor materials and devices* (CRC Press, Boca Raton, FL, 2017), pp. 5-6.

14. S. D. Lester, F. A. Ponce, M. G. Craford, and D. A. Steigelwald. *High dislocation densities in high efficiency GaN-based light-emitting diodes*, Appl. Phys. Lett. **66**, 1249 (1995).

15. S. Nakamura, Y. Harada, and Masayuki Seno, *Novel metalorganic chemical vapor deposition system for GaN growth*, Appl. Phys. Lett. **58**, 2021 (1991).

16. S. Nakamura, M. Senoh, S. Nagahama, N. Iwasa, T. Yamada, T. Matsushita, H. Kiyoku, Y. Sugimoto, T. Kozaki, H. Umemoto, M. Sano, and K. Chocho, *High-power, long-lifetime InGaN/GaN/AlGaN-based laser diodes grown on pure GaN substrates*, Jpn. J. Appl. Phys. **37**, 309 (1998).

17. M. Meneghini, G. Meneghesso, and E. Zanoni, *Power GaN devices, materials, applications and reliability* (Springer International Publishing, Switzerland, 2017), pp. 2-4.

18. D. B. Williams and C. B. Carter, *Transmission electron microscopy: a textbook for materials science* (2nd Ed, Springer, NY, 2009), pp. 414.

19. D. B. Williams and C. B. Carter, *Transmission electron microscopy: a textbook for materials science* (2nd Ed, Springer, NY, 2009), pp. 25.

20. P. B. Hirsch, A. Howie, and M. J. Whelan, *A kinematical theory of diffraction contrast of electron transmission microscope images of dislocations and other defects*, *Phil. Trans. R. Soc. **252**, 499 (1960)*.

21. P. Hartel, H. Rose, and C. Dinges, "*Conditions and reasons for incoherent imaging in STEM*," Ultramicroscopy **62**, 93 (1996).

22. O. L. Krivanek, M. F. Chisholm, V. Nicolosi, T. J. Pennycook, G. J. Corbin, N. Dellby, M. F. Murfitt, C. S. Own, Z. S. Szilagyi, M. P. Oxley, S. T. Pantelides, and S. J. Pennycook, *Atom-by-atom structural and chemical analysis by annular dark-field electron microscopy*, Nature **464**, 571 (2010).

23. L. J. Brillson, *Applications of depth-resolved cathodoluminescence spectroscopy*, J. Phys. D: Appl. Phys. **45**, 183001 (2012).

24. B. G. Yacobi and D. B. Holt, *Cathodoluminescence microscopy of inorganic solids* (Springer, NY, 1990), pp. 55.

25. G. Binnig, C. F. Quate, and Ch. Gerber, *Atomic force microscope*, Phys. Rev. Lett. **56**, 930 (1986).

26. G. Meyer and N. M. Amer, *Novel optical approach to atomic force microscopy*, Appl. Phys. Lett. **53**, 1045 (1988),

27. G. Meyer and N. M. Amer, *Erratum: Novel optical approach to atomic force microscopy (Appl. Phys. Lett. **53**, 1045 (1988))*, Appl. Phys. Lett. **53**, 2400 (1988).

28. S. B. Kaemmer, *Introduction to Bruker's ScanAsyst and PeakForce Tapping AFM Technology*, retrieved from https://www.bruker.com (2011).

29. K. W. J. Barnham and G. Duggan, *A new approach to high-efficiency multi-band-gap solar cells*, J. Appl. Phys. **67**, 3490 (1990).

30. A. J. Nozik, *Quantum dot solar cells*, Physica E **14**, 115 (2002).

31. W. Shockley and H. J. Queisser, *Detailed balance limit of efficiency of p-n junctions solar cells*, J. Appl. Phys. **32**, 510 (1961).

32. S. P. Bremner, R. Corkish, and C. B. Honsberg, *Detailed balance efficiency limits with quasi-Fermi level variations*, IEEE Trans. Electron Devices **46**, 1932 (1999).

33. T. Sogabe, Y. Shoji, M. Ohba, K. Yoshida, R. Tamaki, H.-F. Hong, C.-H. Wu, C.-T. Kuo, S. Tomić, and Y. Okada, *Intermediate-band dynamics of quantum dots solar cell in concentrator photovoltaic modules*, Sci. Rep. **4**, 4792 (2014).

34. E. Antolín, A. Martí, C. D. Farmer, P. G. Linares, E. Hernández, A. M. Sánchez, T. Ben, S. I. Molina, C. R. Stanley, and A. Luque, *Reducing carrier escape in the InAs/GaAs quantum dot intermediate band solar cell*, J. Appl. Phys. **108**, 064513 (2010).

35. A. Datas, E. López, I. Ramiro, E. Antolín, A. Martí, and A. Luque, *Intermediate band solar cell with extreme broadband spectrum quantum efficiency*, Phys. Rev. Lett. **114**, 157701 (2015).

36. R. Jakomin, R. M. S. Kawabata, R. T. Mourão, D. N. Micha, M. P. Pires, H. Xie, A. M. Fischer, F. A. Ponce, and P. L. Souza, *InAs quantum dot growth on $Al_xGa_{1-x}As$ by metalorganic vapor phase epitaxy for intermediate band solar cells*, J. Appl. Phys. **116**, 093511 (2014).

37. H. Xie, R. Prioli, G. Torelly, H. Liu, A. M. Fischer, R. Jakomin, R. Mourão, R. Kawabata, M. P. Pires, P. L. Souza, and F. A. Ponce, *Correlation between size distribution and luminescence properties of spool-shaped InAs quantum dots*, Semicond. Sci. Technol. **32**, 055013 (2017).

38. R. R. King, D. C. Law, K. M. Edmondson, C. M. Fetzer, G. S. Kinsey, H. Yoon, R. A. Sherif, and N. H. Karam, *40% efficient metamorphic GaInP/GaInAs/Ge multijunction solar cells*, Appl. Phys. Lett. **90**, 183516 (2007).

39. I. Ramiro, J. Villa, P. Lam, S. Hatch, J. Wu, E. Lopez, E. Antolin, H. Liu, A. Mart, and A. Luque, *Wide-bandgap InAs/InGaP quantum-dot intermediate band solar cells*, IEEE J. Photovolt. **5**, 840 (2015).

40. J. M. Olson, R. K. Ahrenkiel, D. J. Dunlavy, B. Keyes, and A. E. Kibbler, *Ultralow recombination velocity at $Ga_{0.5}In_{0.5}P$/GaAs heterointerfaces*, Appl. Phys. Lett. **55**, 1208 (1989).

41. N. Dharmarasu, M. Yamaguchi, A. Khan, T. Yamada, T. Tanabe, S. Takagishi, T. Takamoto, T. Ohshima, H. Itoh, M. Imaizumi, and S. Matsuda, *High-radiation-resistant InGaP, InGaAsP, and InGaAs solar cells for multijunction solar cells*, Appl. Phys. Lett. **79**, 2399 (2001).

42. G. B. Stringfellow, *The importance of lattice mismatch in the growth of $Ga_xIn_{1-x}P$ epitaxial crystals*, J. Appl. Phys. **43**, 3455 (1972).

43. C. P. Kuo, S. K. Vong, R. M. Cohen, and G. B. Stringfellow, *Effect of mismatch strain on band gap in III-V semiconductors*, J. Appl. Phys. **57**, 5428 (1985).

44. T. Suzuki, A. Gomyo, S. Iijima, K. Kobayashi, S. Kawata, I. Hino, and T. Yuasa, *Band-gap energy anomaly and sublattice ordering in GaInP and AlGaInP grown by metalorganic vapor phase epitaxy*, J. Appl. Phys., **27**, 2098 (1988).

45. B. T. McDermott, K. G. Reid, N. A. El-Masry, S. M. Bedair, W. M. Duncan, X. Yin, and F. H. Pollak, *Atomic layer epitaxy of GaInP ordered alloy*, Appl. Phys. Lett. **56**, 1172 (1990).

46. L. C. Su, I. H. Ho, and G. B. Stringfellow, *Effects of substrate misorientation and growth rate on ordering in GaInP*, J. Appl. Phys. **75**, 5135 (1994).

47. M. Zorn, P. Kurpas, A.I. Shkrebtii, B. Junno, A. Bhattacharya, K. Knorr, M. Weyers, L. Samuelson, J.-T. Zettler, and W. Richter, *Correlation of InGaP (0001) surface structure during growth and bulk ordering*, Phys. Rev. B **60,** 8185 (1999).

48. P. Hartel, H. Rose, and C. Dinges, *Conditions and reasons for incoherent imaging in STEM*, Ultramicroscopy **62**, 93 (1996).

49. O. L. Krivanek, M. F. Chisholm, V. Nicolosi, T. J. Pennycook, G. J. Corbin, N. Dellby, M. F. Murfitt, C. S. Own, Z. S. Szilagyi, M. P. Oxley, S. T. Pantelides, and S. J. Pennycook, *Atom-by-atom structural and chemical analysis by annular dark-field electron microscopy*, Nature **464**, 571 (2010).

50. D. D. Perovic, C. J. Rossouw, and A. Howie, *Imaging elastic strains in high-angle annular dark field scanning transmission electron microscopy*, Ultramicroscopy **52**, 353 (1993).

51. C. S. Baxter, W. M. Stobbs, and J. H. Wilkie, *The morphology of ordered structures in III-V alloys: inferences from a TEM study*, J. Cryst. Growth **112**, 373 (1991).

52. P. Bellon, J. P. Chevalier, E. Augarde, J. P. André, and G. P. Martin, *Substrate-driven ordering microstructure in $Ga_xIn_{1-x}P$ alloys*, J. Appl. Phys. **66**, 2388 (1989).

53. G. S. Chen, D. H. Jaw, and G. B. Stringfellow, *Atomic ordering in GaAsP*, J. Appl. Phys. **69**, 4263 (1991).

54. G. S. Chen and G. B. Stringfellow, *Effects of step motion on ordering in GaInP*, Appl. Phys. Lett. **59**, 324 (1991).

55. S.-H. Wei, D. B. Laks, and A. Zunger, *Dependence of the optical properties of semiconductor alloys on the degree of long-range order*, Appl. Phys. Lett. **62**, 1937 (1993).

56. M. C. DeLong, D. J. Mowbray, R. A. Hogg, M. S. Skolnick, J. E. Williams, K. Meehan, Sarah R. Kurtz, J. M. Olson, R. P. Schneider, M. C. Wu, and M. Hopkinson, *Band gap of ''completely disordered'' $Ga_{0.52}In_{0.48}P$*, Appl. Phys. Lett. **66**, 3185 (1995).

57. J. M. Garcia, J. P. Silveira, and F. Briones, *Strain relaxation and segregation effects during self-assembled InAs quantum dots formation on GaAs (001)*, Appl. Phys. Lett. **77**, 409 (2000).

58. I. Sagnes, I. Prévot, G. Patriarche, G. Le Roux, B. Gayral, A. Lemaître, and J. M. Gérard, *High-quality InAs/GaAs quantum dots grown by low-pressure metalorganic vapor-phase epitaxy*, J. Cryst. Growth **195**, 524 (1998).

59. D. Alonso-Álvarez, B. Alén, J. M. Ripalda, A. Rivera, A. G. Taboada, J. M. Llorens, Y. González, L. González, and F. Briones, *Strain driven migration of In during the growth of InAs/GaAs quantum posts*, APL Materials **1**, 022112 (2013).

60. H. Xie, R. Prioli, A. M. Fischer, F. A. Ponce, R. M. S. Kawabata, L. D. Pinto, R. Jakomin, M. P. Pires, and P. L. Souza, *Improved optical properties of InAs quantum dots for intermediate band solar cells by suppression of misfit strain relaxation*, J. Appl. Phys. **120**, 034301 (2016).

61. D. Bimberg, M. Grundmann, and N. N. Ledentsov, *Quantum Dot Heterostructures* (John Wiley & Sons, Chicester, 1999), pp. 54-56.

62. H. Murata, I. H. Ho, L. C. Su, Y. Hosokawa, and G. B. Stringfellow, *Surface photoabsorption study of the effects of growth temperature and V/III ratio on ordering in GaInP*, J. Appl. Phys. **79**, 6895 (1996).

63. G. B. Stringfellow, J. K. Shurtleff, R. T. Lee, C. M. Fetzer, and S. W. Jun, *Surface processes in OMVPE – the frontiers*, J. Cryst. Growth **221**, 1 (2000).

64. R. R. King, C. M. Fetzer, P. C. Colter, K. M. Edmondson, J. H. Ermer, H. L. Cotal, H. Yoon, A. P. Stavrides, G. Kinsey, D. D. Krut, and N. H. Karam, *High-Efficiency Space and Terrestrial Multijunction Solar Cells Through Bandgap Control in Cell Structures*, Proc. 29th IEEE Photovoltaic Specialists Conf., (IEEE, New York, 2002), ISBN 0-7803-7471-1, pp. 776-781.

65. S. Nakamura, T. Mukai, and M. Senoh, *High-power GaN p-n junction blue-light-emitting diodes*, Jpn. J. Appl. Phys. **30**, 1998 (1991).

66. I. C. Kizilyalli, A. P. Edwards, O. Aktas, T. Prunty, and D. Bour, *Vertical power p-n diodes based on bulk GaN*, IEEE Trans Electron Devices **62**, 414 (2015).

67. K. Fujito, S. Kubo, H. Nagaoka, T. Mochizuki, H. Namita, and S. Nagao, *Bulk GaN crystals grown by HVPE*, J. Cryst. Growth **311**, 3011 (2009).

68. K. Motoki, T. Okahisa, R. Hirota, S. Nakahata, K. Uematsu, and N. Matsumoto, *Dislocation reduction in GaN crystal by advanced-DEEP*, J. Cryst. Growth **305,** 377 (2007).

69. K. Xu, J.-F. Wang, and G.-Q. Ren, *Progress in bulk GaN growth*, Chin. Phys. B **24**, 066105 (2015).

70. F. Oehler, T. Zhu, S. Rhode, M. J. Kappers, C. J. Humphreys, and R. A. Oliver, *Surface morphology of homoepitaxial c-plane GaN: hillocks and ridges*, J. Cryst. Growth **383**, 12 (2013).

71. I. C. Kizilyalli, D. P. Bour, T. R. Prunty, and G. Ye, *High power gallium nitride electronics using miscut substrates*, U.S. Patent 20150123138 (4 November 2013).

72.T. Suski, E. Litwin-Staszewska, R. Piotrzkowski, R. Czernecki, M. Krysko, S. Grzanka, G. Nowak, G. Franssen, L. H. Dmowski, M. Leszczynski, P. Perlin, B. Łucznik, I. Grzegory, and R. Jakieła, *Substrate misorientation induced strong increase in the hole concentration in Mg doped GaN grown by metalorganic vapor phase epitaxy*, Appl. Phys. Lett. **93**, 172117 (2008).

73. L. Jiang, J. Liu, A. Tian, X. Ren, S. Huang, W. Zhou, L. Zhang, D. Li, S. Zhang, M. Ikeda, and H. Yang, *Influence of substrate misorientation on carbon impurity incorporation and electrical properties of p-GaN grown by metalorganic chemical vapor deposition*, Appl. Phys. Express **12**, 055503 (2019).

74. M. Kryśko, G. Franssen, T. Suski, M. Albrecht, B. Łucznik, I. Grzegory, S. Krukowski, R. Czernecki, S. Grzanka, I. Makarowa, M. Leszczyński, and P. Perlin, *Correlation between luminescence and compositional striations in InGaN layers grown on miscut GaN substrates*, Appl. Phys. Lett. **91**, 211904 (2007).

75. M. Shinohara and N. Inoue, *Behavior and mechanism of step bunching during metalorganic vapor phase epitaxy of GaAs*, Appl. Phys. Lett. **66**, 15 (1995).

76. G. S. Bales and A. Zangwill, *Morphological instability of a terrace edge during step-flow growth*, Phys. Rev. B **41**, 5500 (1990).

77. J. Frohn, M. Giesen, M. Poensgen, J. F. Wolf, and H. Ibach, *Attractive interaction between steps*, Phys. Rev. Lett. **67**, 3543 (1991).

78. R. L. Schwoebel and E. J. Shipsey, *Step motion on crystal surfaces*, J. Appl. Phys. **37**, 3682 (1966).

79. N. A. K. Kaufmann, L. Lahourcade, B. Hourahine, D. Martin, and N. Grandjean, *Critical impact of Ehrlich–Schwöbel barrier on GaN surface morphology during homoepitaxial growth*, J. Cryst. Growth **433**, 36 (2016).

80. J. E. Chung, J. Chen, P. K. Ko, C. Hu, and M. Levi, *The effects of low-angle off-axis substrate orientation on MOSFET performance and reliability*, IEEE Trans. Electron Devices **38**, 3 (1991).

81. T. Saku, Y. Horikoshi, and Y. Tokura, *Limit of electron mobility in AlGaAs/GaAs modulation-doped heterostructures*, Jpn. J. Appl. Phys. **35**, 34 (1996).

82. F. A. Ponce, D. Cherns, W. T. Young, and J. W. Steeds, *Characterization of dislocations in GaN by transmission electron diffraction and microscopy techniques*, Appl. Phys. Lett. **69**, 770 (1996).

83. F. A. Ponce, W. T. Young, D. Cherns, J. W. Steeds, and S. Nakamura, *Nanopipes and inversion domains in high-quality GaN epitaxial layers*, MRS Proc. Vol. **449**, 405 (1996). DOI: 10.1557/PROC-449-405

84. D. Cherns, W. T. Young, J. W. Steeds, F. A. Ponce, and S. Nakamura, *Observation of coreless dislocations in α-GaN*, J. Cryst. Growth **178**, 201 (1997).

85. D. Cherns, W. T. Young, J. W. Steeds, F. A. Ponce, and S. Nakamura, *Determination of the atomic structure of inversion domain boundaries in GaN by transmission electron microscopy*, Phil. Mag. **A77**, 273 (1998).

86. H. Amano, *Progress and prospect of the growth of wide-band-gap group III nitrides*, Jpn. J. Appl. Phys. **22**, 05001 (2013).

87. K. Motoki, R. Hirota, T. Okahisa, and S. Nakahata, *Single crystal GaN substrate, method of growing single crystal GaN and method of producing single crystal GaN substrate*, U. S. Patent No. 7.534,310 B2 (19 May 2009).

88. K. Iso, H. Kimura, Y. Saito, and Y. Enatsu, *C-plane GaN substrate*, U. S. Patent No. 10, 177, 217 B2 (8 January 2019).

89. J. S. Ozcomert, W. W. Pai, N. C. Bartelt, and J. E. Reutt-Robey, *Step configurations near pinning sites on Ag(110)*, Surf. Sci. **293**. 183 (1993).

90. M. V. Ramana Murty, P. Fini, G. B. Stephenson, Carol Thompson, J. A. Eastman, A. Munkholm, O. Auciello, R. Jothilingam, S. P. DenBaars, and J. S. Speck, *Step bunching on the vicinal GaN(0001) surface*, Phys. Rev. B **62**, R10661 (2000).

91. M. H. Xie, S. M. Seutter, W. K. Zhu, L. X. Zheng, Huasheng Wu, and S. Y. Tong, *Anisotropic step-flow growth and island growth of GaN(0001) by molecular beam epitaxy*, Phys. Rev. Lett. **82**, 2749 (1999).

92. F. Shahedipour and B. W. Wessels, *Investigation of the formation of the 2.8 eV luminescence band in p-type GaN:Mg*, Appl. Phys. Lett. **76**, 3011 (2000).

93. U. Kaufmann, M. Kunzer, M. Maier, H. Obloh, A. Ramakrishnan, B. Santic, and P. Schlotter, *Nature of the 2.8 eV photoluminescence band in Mg doped GaN*, Appl. Phys. Lett. **72**, 1326 (1998).

94. F. C. Frank, *Capillary equilibria of dislocated crystals*, Acta Cryst. **4**, 497 (1951).

95. B. Heying, E. J. Tarsa, C. R. Elsass, P. Fini, S. P. DenBaars, and J. S. Speck, *Dislocation mediated surface morphology of GaN*, J. Appl. Phys. **85**, 6470 (1999).

96. W. K. Burton, N. Cabrera, and F. C. Frank, *The growth of crystals and the equilibrium structure of their surfaces*, Philos. Trans. R. Soc. London Ser. A **243**, 299 (1951).

97. J. A. Venables, G. D. T. Spiller, and M. Hanbucken, *Nucleation and growth of thin films*, Rep. Prog. Phys. **47**, 399 (1984).

98. G. B. Stephenson, J. A. Eastman, C. Thompson, O. Auciello, L. J. Thompson, A. Munkholm, P. Fini, S. P. DenBaars, and J. S. Speck, *Observation of growth modes during metal-organic chemical vapor deposition of GaN*, Appl. Phys. Lett. **74**, 3326 (1999).

99. J. Y. Tsao, *Materials Fundamentals of Molecular Beam Epitaxy* (Academic, San Diego, 1993), pp. 239.

100. C. Herring, *Some theorems on the free energies of crystal surfaces*, Phys. Rev. **82**, 87 (1951).

101. V. A. Shchukin and D. Bimberg, *Spontaneous ordering of nanostructures on crystal surfaces*, Rev. Mod. Phys. **71**, 1125 (1999).

102. I. V. Markov, *Crystal growth for beginners: fundamentals of nucleation, crystal growth and epitaxy*, World Scientific, Singapore, pp. 192 (2016).

103. T. Kimoto and H. Matsunami, *Surface diffusion lengths of adatoms on 6H-SiC(0001) faces in chemical vapor deposition of SiC*, J. Appl. Phys. **78**, 3132 (1995). See eq. 3.

104. N. Toyoda, M. Mihara, and T. Hara, *Impurity effect on the formation of terraces in GaAs LPE growth*, Phys. Stat. Sol. (a) **54**, 225 (1979).

105. E. D. Williams, *Surface steps and surface morphology: understanding macroscopic phenomena from atomic observations*, Surf. Sci. **299/300**, 502 (1994).

106. B. Beaumont, S. Haffouz, and P. Gibart, *Magnesium induced changes in the selective growth of GaN by metalorganic vapor phase epitaxy*, Appl. Phys. Lett. **72**, 921 (1998).

107. H. Liu, P.-Y. Su, Z. Wu, R. Liu, and F. A. Ponce, *Influence of substrate misorientation on the optical properties of Mg-doped GaN*, J. Appl. Phys., **127**, 195701 (2020).

108. O. L. Alerhand, A. N. Berker, J. D. Joannopoulos, D. Vanderbilt, R. J. Hamers, and J. E. Demuth, *Finite-temperature phase diagram of vicinal Si(100) surfaces*, Phys. Rev. Lett. **64**, 2406 (1990).

109. T. Kimoto and H. Matsunami, *Surface kinetics of adatoms in vapor phase epitaxial growth of SiC on 6H-SiC{0001} vicinal surfaces*, J. Appl. Phys. **75**, 850 (1994). See eq. 7.

110. A. V. Lobanova, E. V. Yakovlev, R. A. Talalaev, S. B. Thapa, and F. Scholz, *Growth conditions and surface morphology of AlN MOVPE*, J. Cryst. Growth **310**, 4935 (2008).

111. S. J. Pearton, R. J. Shul, and F. Ren, *A Review of Dry Etching of GaN and Related Materials*, MRS Internet J. Nitride Semicond. Res. **5**, 11 (2000).

112. J. Neugebauer and C. G. Van de Walle, *Gallium vacancies and the yellow luminescence in GaN*, Appl. Phys. Lett. **69**, 503 (1996).

113. K. Saarinen, T. Laine, S. Kuisma, J. Nissila, P. Hautojarvi, L. Dobrzynski, K. Pakula, R. Stepniewski, M. Wojdak, A. Wysmolek, T. Suski, M. Leszczynski, I. Grzegory, and S. Porowski, *Observation of native Ga vacancies in GaN by positron annihilation*, Phys. Rev. Lett. **79**, 3030 (1997).

114. D. Basak, M. Lachab, T. Nakanishi, and S. Sakai, *Effect of reactive ion etching on the yellow luminescence of GaN*, Appl. Phys. Lett. **75**, 3710 (1999).

115. K. Kanaya and S. Okayama, *Penetration and energy-loss theory of electrons in solid targets*, J. Phys. D App. Phys. **5**, 43 (1972).

116. J. I. Goldstein, D. Newbury, D. Joy, C. Lyman, P. Echlin, E. Lifshin, L. Sawyer, and J. Michael, *Scanning electron microscopy and x-ray microanalysis*, (Springer, 3rd edition, New York, 2003) p.72.

117. K. Fu, H. Fu, X. Huang, H. Chen, T.-H. Yang, J. Montes, C. Yang, J. Zhou, and Y. Zhao, *Demonstration of 1.27 kV etch-then-regrow GaN p-n junctions with low leakage for GaN power electronics*, IEEE Electron Device Lett. **40**, 1728 (2019).

118. D. Ji and S. Chowdhury, *Design of 1.2 kV power switches with low R_{ON} using GaN-Based vertical JFET*, IEEE Trans Electron Devices **62**, 8 (2015).

119. K. Hiramatsu, K. Nishiyama, M. Onishi, H. Mizutani, M. Narukawa, A. Motogaito, H. Miyake, Y. Iyechika, and T. Maeda, *Fabrication and characterization of low defect density GaN using facet-controlled epitaxial lateral overgrowth (FACELO)*, J. Cryst. Growth, **221**, 316 (2000).

120. B. Beaumont, M. Vaille, G. Nataf, A. Bouillé, J.-C. Guillaume, P. Vénnègues, S. Haffouz, and P. Gibart, *Mg-enhanced lateral overgrowth of GaN on patterned GaN/sapphire substrate by selective metal organic vapor phase epitaxy*, MRS Int. J. Nitride Semicond. Res. **3**, 20 (1998).

121. L. Zhang, H. F. Tang, and T. F. Kuech, *Effect of Sb as a surfactant during the lateral epitaxial overgrowth of GaN by metalorganic vapor phase epitaxy*, Appl. Phys. Lett. **79**, 3059 (2001).

122. L. Zhang, H. F. Tang, J. Schieke, M. Mavrikakis, and T. F. Kuech, *The addition of Sb as a surfactant to GaN growth by metal organic vapor phase epitaxy*, J. Appl. Phys. **92**, 2304 (2002).

123. S. R. Alugubelli, H. Fu, K. Fu, H. Liu, Y. Zhao, and F. A. Ponce, *Dopant profiling in p-i-n GaN structures using secondary electrons*, J. Appl. Phys. **126**, 015704 (2019).

124. P.-Y. Su, H. Liu, S. Wang, Z. Wu, R. Liu, and F. A. Ponce, *The effect of low-angle off-axis GaN substrate orientation on the surface morphology of Mg-doped GaN epilayers*, submitted to J. Appl. Phys.

125. H. Amano, M. Kitoh, K. Hiramatsu, and I. Akasaki, *Growth and Luminescence Properties of GaN:Mg Prepared by MOVPE*, J. Electrochem. Soc. **137**, 1639 (1990).

126. H. Obloh, K.H. Bachem, U. Kaufmann, M. Kunzer, M. Maier, A. Ramakrishnan, and P. Schlotter, *Self-compensation in Mg doped p-type GaN grown by MOCVD*, J. Cryst. Growth **195**, 270 (1998).

127. H. Liu, H. Fu, K. Fu, S. R. Alugubelli, P.-Y, Su, Y. Zhao, and F. A. Ponce, *Non-uniform Mg distribution in GaN epilayers grown on mesa structures for applications in GaN power electronics*, Appl. Phys. Lett. **114**, 082102 (2019).

128. P.-Y. Su, H. Liu, R. M. S. Kawabata, E. C. Weiner, R. Jakomin, M. P. Pires, R. R. King, P. L. Souza, and F. A. Ponce, *Effect of InAs quantum dots capped with GaAs on atomic-scale ordering in $Ga_{0.5}In_{0.5}P$*, J. Appl. Phys. **125**, 053104 (2019).

129. A. Luque, P. G. Linares, A. Mellor, V. Andreev, and A. Marti, *Some advantages of intermediate band solar cells based on type II quantum dots*, Appl. Phys. Lett. **103**, 123901 (2013).

130. A. Luque, A. Marti, and C. Stanley, *Understanding intermediate-band solar cells*, Nat. Photonics **6**, 146 (2012).

131. M. Hayne, R. Provoost, M. K. Zundel, Y. M. Manz, K. Eberl, and V. V. Moshchalkov, *Electron and hole confinement in stacked self-assembled InP quantum dots*, Phys. Rev. B **62**, 10324 (2000).

132. E. Ribeiro, R. L. Maltez, W. Carvalho Jr., D. Ugarte, and G. Medeiros-Ribeiro, *Optical and structural properties of InAsP ternary self-assembled quantum dots embedded in GaAs*, Appl. Phys. Lett. **81**, 2953 (2002).

133. M. Tytus, J. Krasnyj, W. Jacak, A. Chuchmała, W. Donderowicz, and L. Jacak, *Differences between photoluminescence spectra of type-I and type-II quantum dots*, J. Phys.: Conf. Ser. **104**, 012011 (2008).

134. D. Leonard, M. Krishnamurthy, C. M. Reaves, S. P. Denbaars, and P. M. Petroff, *Direct formation of quantum-sized dots from uniform coherent islands of InGaAs on GaAs surfaces*, Appl. Phys. Lett. **63**, 3203 (1993).

135. R. L. Maltez, E. Ribeiro, W. Carvalho, Jr., D. Ugarte, and G. Medeiros-Ribeiro, *Controlling alloy composition of InAsP self-assembled quantum dots embedded in GaAs*, J. Appl. Phys. **94**, 3051 (2003).

136. D. J. Cole-Hamilton and J. O. Williams, *Mechanisms of Reactions of Organometallic Compounds with Surfaces*, Plenum, New York, p.p. 162 (1989).

137. Y. Andre, A. Trassoudaine, J. Tourret, R. Cadoret, E. Gil, D. Castelluci, O. Aoude, and P. Disseix, *Low dislocation density high-quality thick hydride vapour phase epitaxy (HVPE) GaN layers*, J. Cryst. Growth **306**, 86 (2007).

138. M. Bockowski, M. Iwinska, M. Amilusik, M. Fijalkowski, B. Lucznik, and T. Sochacki, *Challenges and future perspectives in HVPE-GaN growth on ammonothermal GaN seeds*, Semicond. Sci. Technol. **31**, 093002 (2016).

139. I. Bryan, Z. Bryan, S. Mita, A. Rice, J. Tweedie, R. Collazo, and Z. Sitar, *Surface kinetics in AlN growth: a universal model for the control of surface morphology in III-nitrides*, J. Cryst. Growth, **438**, 819 (2016).

140. T. Tanikawa, K. Shojiki, T. Aisaka, T. Kimura, S. Kuboya, T. Hanada, R. Katayama, and T. Matsuoka, *Enhancement of surface migration by Mg doping in the metalorganic vapor phase epitaxy of N-polar* $(000\bar{1})$ *GaN/sapphire*, Jpn. J. Appl. Phys. **53**, 05FL05 (2014).

141. R. Dwiliński, R. Doradziński, J. Garczyński, L. P. Sierzputowski, A. Puchalski, Y. Kanbara, K. Yagi, H. Minakuchi, and H. Hayashi, *Excellent crystallinity of truly bulk ammonothermal GaN*, J. Cryst. Growth **310**, 3911 (2008).

142. R. Dwiliński, R. Doradziński, J. Garczyński, L. P. Sierzputowski, A. Puchalski, Y. Kanbara, K. Yagi, H. Minakuchi, and H. Hayashi, *Bulk ammonothermal GaN*, J. Cryst. Growth **311**, 3015 (2009).

APPENDIX A

PUBLICATIONS DURING THE STUDY TOWARDS THE DOCTORAL DEGREE

P.-Y. Su, H. Liu, S. Wang, Z. Wu, R. Liu, and F. A. Ponce, *The effect of low-angle off-axis GaN substrate orientation on the surface morphology of Mg-doped GaN epilayers*, submitted to J. Appl. Phys. on Jun. 1, 2020.

H. Liu, P.-Y. Su, Z. Wu, R. Liu, and F. A. Ponce, *Effects of substrate misorientation angle on the optical properties of Mg-doped GaN*, J. Appl. Phys., 127, 195701 (2020).

P.-Y. Su, H. Liu, R. M. S. Kawabata, E. C. Weiner, R. Jakomin, M. P. Pires, R. R. King, P. L. Souza, and F. A. Ponce, *Effect of InAs quantum dots capped with GaAs on ordering in* $Ga_{0.5}In_{0.5}P$, J. Appl. Phys., 125, 053104 (2019).

H. Liu, H. Fu, K. Fu, S. R. Alugubelli, P.-Y. Su, Y. Zhao, and F. A. Ponce, *Non-uniform Mg distribution in GaN epilayers grown on mesa structures for applications in GaN power electronics*, Appl. Phys. Lett., 114, 082102 (2019).

E. C. Weiner, R. Jakomin, D. N. Micha, H. Xie, P.-Y. Su, L. D. Pinto, M. P. Pires, F. A. Ponce, and P. L. Souza, *Effect of capping procedure on quantum dot morphology: Implications on optical properties and efficiency of InAs/GaAs quantum dot solar cells*, Sol. Energy Mater. Sol. Cells, 178, 240–248 (2018).

X. Huang, D. Li, P.-Y. Su, H. Fu, H. Chen, J. Montes, T.-H. Yang, C. Yang, J. Zhou, X. Qi, X. Deng, K. Fu, S. P. DenBaars, S. Nakamura, F. A. Ponce, C.-Z. Ning, and Y. Zhao, *Carrier dynamics and localization in nonpolar m-plane InGaN/GaN quantum wells at high temperatures*, J. Nano Energy, accepted (2020).

K. Fu, H. Fu, X. Deng, C.-Y. Cheng, P.-Y. Su, H. Liu, K. Hatch, D. Messina, R. V. Meidanshahi, P. Peri, C. Yang, X. Huang, T.-H, Yang, H. Chen, J. Montes, J. Zhou, X. Qi, S. M. Goodnick, F. A. Ponce, D. J. Smith, R. Nemanich, and Y. Zhao, *Exploring the origin of Si contaminations at GaN epitaxial regrowth interfaces and their impacts for vertical GaN power devices*, submitted to J. Adv. Mater. on Jun. 4, 2020.

C. Yang, H. Fu, P.-Y. Su, H. Liu, K. Fu, X. Huang, T.-H, Yang, H. Chen, J. Zhou, X. Deng, J. Montes, X. Qi, F. A. Ponce, and Y. Zhao, *Demonstration of GaN-based metal-insulator-semiconductor junction by hydrogen plasma treatment*, submitted to Appl. Phys. Lett. on Jun. 15, 2020.

P.-Y. Su, H. Liu, C. Yang, K. Fu, H. Fu, Y. Zhao, and F. A. Ponce, *Lateral vs. vertical growth of Mg-doped GaN on trench-patterned GaN films*, submitted to Appl. Phys. Lett. on Jun. 22, 2020.